Combustion Spraying

7

Abbreviations

APS	Atmospheric Plasma Spraying
BC	Bond Coat
CFD	Computational Fluid Dynamic
DC	Direct Current
D-gun	Detonation Gun
EDS	Energy Dispersive Spectroscopy
FS	Flame Spraying
GS-HVOF	Gas Shroud High-Velocity Oxy Fuel
HVAF	High-Velocity Air Fuel
HVOF	High-Velocity Oxy Fuel
HV-SPS	High velocity Suspension Plasma Spraying
LHS	Left-Hand Side
LT-HVOF	Low-Temperature High-Velocity Oxy Fuel
MPD	Maximum Power Density
PDTS	Pulse Detonation Thermal Spray
PFS	Powder Flame Spraying
PTS	Polymer Thermal Spray
RHS	Right-Hand Side
RT	Room Temperature
SBF	Simulated Body Fluid
SEM	Scanning Electron Microscopy
SFS	Solution Flame Spraying
SHS	Self-propagating High Temperature Synthesis
slm	standard liters per minute
SoD	Standoff Distance
WFS	Wire Flame Spraying
WS-HVAF	Warm Spray High-Velocity Air Fuel
XRD	X-ray Diffraction
YSZ	Yttria-stabilized zirconia

7.1 Overview of Combustion-Based Spray Technologies

"Combustion spraying," often referred to as "Flame spraying (FS)," is at the base of the wide field of thermal spray technologies which was developed in the early twentieth century and remains one of the most widely used spray coating processes because of their favorable economics. Its most common application is in the corrosion protection of infrastructure buildings such as bridges and steel structures. Over the years, the growth of combustion processes was driven by both scientific and technical developments and market requirements. The development of High-Velocity Oxy Fuel (HVOF) spraying by Browning in 1983 is a typical example which was pushed forward by the need to produce WC-Co cermet coatings with superior properties as a replacement for the environmentally polluting chrome plating technologies. Table 7.1 lists the milestones in the development of some of the most important combustion-based spray processes.

In this chapter, a review is made of three combustion-based spray technologies covering for each, the basic principal behind the process, their main characteristics, as well as potential applications and limitations. These are:

– ***Flames spraying (FS)*** using mostly oxy-acetylene torches achieving premixed combustion temperatures up to about 3000 K. Sprayed materials are introduced generally axially into the spray gun. Flame velocities below 100 m/s characterize this process. This technique was the first to be developed in 1909 by Maximilian Ulrich Schoop.

M. I. Boulos et al. (ed.), *Thermal Spray Fundamentals*, https://doi.org/10.1007/978-3-030-70672-2_7

Table 7.1 Milestones in the development of key combustion-based spray processes

Year	Process	Energy generation	Inventor(s)	Reference
1909	Flame spraying (FS)	Combustion (diffusive)	Schoop (Switzerland)	Anon. (1913)
1955	Detonation gun spraying (D-gun)	Combustion (detonation)	Gfeller and Baiker[a] (USA)	Smith (1991)
1983	High velocity oxy fuel (HVOF)	Combustion (deflagration)	Browning (USA)	Browning (1983)

[a]Union Carbide, today Praxair Surface Technology (USA)

– ***High-Velocity Oxy Fuel flame (HVOF)*** spraying (or supersonic flame spraying) where the flame (or deflagration) of a gaseous or liquid hydrocarbon molecule (C_xH_y for example) is achieved at an adjustable stoichiometry with an oxidizer, which is either oxygen or air in a chamber at pressures between 0.24 and 0.82 MPa. The chamber is connected to a convergent-divergent (C-D) Laval nozzle achieving very high gas velocities (up to 2200 m/s), which would be in the range of Mach 2 when considering the local pressure and temperature. Recently, new spray guns using kerosene as fuel have been developed with chamber pressures up to 1 MPa. The trend is also to reduce the combustion temperature and increase the velocity of the combustion products by injecting non-combustible gases such as nitrogen in the combustion chamber. *High-velocity air-fuel flame (HVAF)* is a variant of this technology in which oxygen is replaced by air, which reduces the cost of the spraying process without compromising the quality of the coating. The principal difference is in the flame temperature, which is typically 500 to 1000 °C lower for air/fuel compared to oxygen/fuel combustion. For example, propane/air combustion has an adiabatic flame temperature of 1967 °C, while propane/oxygen combustion temperature is 2526 °C. This results in a lower particle temperature for HVAF processes, which can have either positive or negative effects on the properties of the coating depending on the materials being sprayed. Cermet-type coatings and lower-melting-point materials may benefit from less thermal degradation and oxidation with HVAF.
– ***Detonation gun spraying (D-gun)*** generally using acetylene-oxygen or hydrogen-oxygen mixture contained in a tube closed at one of its ends. The shock wave generated by the reaction in the highly compressed explosive medium (about 2 MPa) heats and accelerates the particles to be sprayed, which are projected toward the substrate. Gas velocities above 2000 m/s are commonly achieved in detonation spray guns. Contrary to the two previous processes where combustible gases and powders are continuously fed within the gun, combustible gas and powder are fed in D-guns in cycles repeated at a frequency ranging from 3 to 100 Hz.

In the following, each of these three techniques will be described in detail. References are given for expanded exposure to recent developments and immerging technologies and their applications.

7.2 Flame Spraying

7.2.1 Basic Concepts

Flame spraying requires the melting of the sprayed material, generally metals or alloys. The process relies on the combustion of a gaseous fuel for the generation of a high-temperature flue gas stream which is used to heat and melt, in-flight, the precursor powder and accelerates the formed droplets toward the substrate on which they are deposited forming the coating. Oxy-acetylene torches are most commonly used for flame spraying. The mixture of acetylene (C_2H_2) and oxygen (O_2) at a stoichiometric ratio gives rise to a combustion temperature of 3410 K at atmospheric pressure, which is the highest temperature of all hydrocarbon gaseous fuels (C_nH_m) at this pressure (see Chap. 3, Table 3.1). Stoichiometry corresponds to the full transformation of C into CO_2 and H into H_2O, according to the global reaction:

$$2\,C_2H_2 + 5\,O_2 \rightarrow 4\,CO_2 + 2\,H_2O \qquad (7.1)$$

The parameter *R*', defined as the fuel to oxidant *(F/A)* ratio used, compared to that of their stoichiometric value $(F/A)_{St}$, is a good indicator of the combustion conditions.

$$R' = (F/A)/(F/A)_{St.} \qquad (7.2)$$

where *F* is the volume or mass feed rate of the fuel and *A* the corresponding value for the oxidizer (see Chap. 3 for more details). The mixture is called fuel rich if $R' > 1$ and fuel lean if $R' < 1$. It should be noted that combustion reactions may also be defined by the Stoichiometric factor, S_t, defined as:

$$S_t = Q_{O_2}/\left(Q_{O_2}\right)_{St.} \qquad (7.3)$$

where Q_{O_2} is the oxygen flow rate (slm), and $\left(Q_{O_2}\right)_{St.}$ the stoichiometric value of oxygen flow rate necessary for the

complete combustion of the fuel. Obviously R and S_t are interrelated with $S_t = 1/R'$.

As the flame length is limited and the particle velocity is only a few tens of m/s, the maximum temperatures that the particles can achieve after their flight is about $T_p = 0.7xT_g$ to $0.8xT_g$, with T_g being the gas temperature, that is, $T_p \approx$ 2300 K for a flame temperature of about 3000 K, which is too low to melt most ceramic materials.

Flame spray has also been used with precursors in the form of wires, cords, and rods, which are introduced axially through the rear of the nozzle into the flame burning at the nozzle exit. Cords being formed of a continuous thin metallic foil folded on itself after being filled with the material to be sprayed as fine powder, mostly ceramics. The resultant, powder-packed, continuous tube has a diameter compatible with most spray wires. Rods, on the other hand, are made of a sintered ceramic with a diameter in the range of 3.17 to 6.35 mm, though generally limited in length to less than1.0 m. As the material fed is melted, it is atomized, forming droplets which are accelerated toward the substrate surface by the expanding hot gas flow and air jets. The main difference between the delivery of the feedstock as either powder or wire, cord, or rod is the melting capability. In contrast, powders, the metal wire, cords, or rods can be advanced in the flame in such a way as to allow their tip to be reached high temperatures for melting and atomization. The formed droplets of the molten material can reach in this case temperatures as high as $0.95T_g$ ($T_p \approx 2850\ K$ for a flame temperature of about 3000 K), which would allow even zirconia to be melted [Thermal Spraying (1985)].

Numerous specialized torch designs have been developed for the "Flame Spraying" of different materials, in powder, wires, cords, or rods, for different applications. Examples are given in the following highlighting design features and typical operating conditions and applications.

7.2.2 Powder Flame Spraying

7.2.2.1 Spray Gun Design and Process Characteristics

A schematic of a typical Sulzer-Metco powder flame spraying (PFS) torch is given in Fig. 7.1. The acetylene and oxygen premixed streams are fed to the nozzle extremity through a ring of 16 to 18 orifices each with an i.d. $\leq$ 1 mm to avoid the flashback of the flame (see Chap. 3, section 3.1.4.1). Proper control of the gas feeding velocity v_u compared to the flame velocity, V_f, is critical for flame stability. As shown in Fig. 7.2, if $v_u \gg V_f$, the flame is blown out, while if $v_u \ll V_f$, flash-back occurs, except if the feeding orifice diameters are small enough to quench the flame and destroy all radicals. In this case, the flame extinguishes.

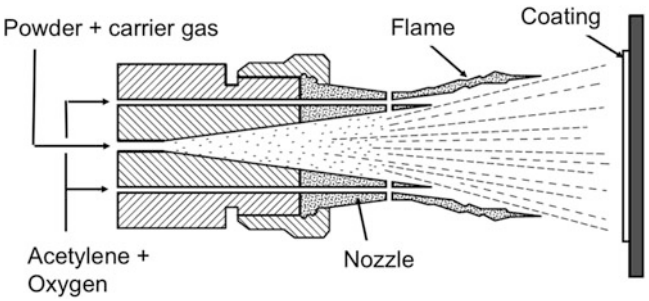

Fig. 7.1 Principal of the Flame Powder Spraying torch. (Courtesy of Sultzer Metco)

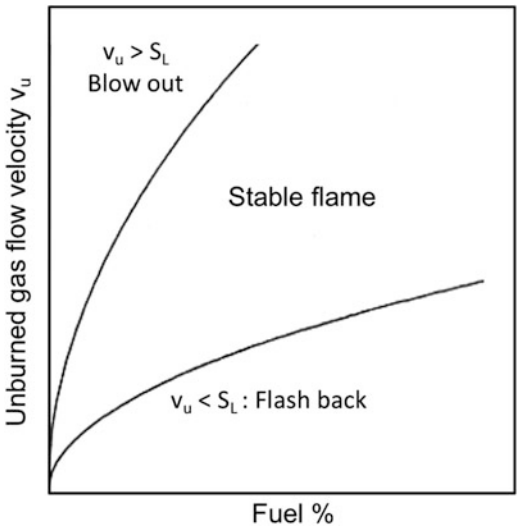

Fig. 7.2 Pre-mixed flame stability diagram [Wigren et al. (1996)]. (Reprinted with kind permission from ASM International)

It is important to emphasize that the power generated in the flame, P_F, depends on the nature of the fuel and oxidizer chosen (highest values being obtained with O_2 and C_2H_2 mixture as shown in Table 3.1 in Chap. 3). P_F depends also on the fuel/oxidizer ratio (about 1/1.6 for the O_2-C_2H_2 mixture) and on the combustible gas flow rate $\dot{m}_u$. Practically, for the oxy-acetylene mixture, P_F is proportional to the oxygen gas flow rate Q_{O_2} (slm), which is the limiting factor.

$$P_F \approx 1.354\ Q_{O_2} \tag{7.4}$$

For $Q_{O_2} = 27\ slm$, $P_F = 36.6\ kW$. It is important to note that in flame spraying, the generated power P_F is typically in the 10 to 50 kW range, which is comparable to that of most plasma spray torches [Wigren et al. (1996)].

In a more recent design of the powder flame spray torch, by Oerlikon-Metco, given in Fig. 7.3, the spray powder is introduced laterally into the central axial channel of the torch, from which it is transported by the gaseous fuel into the

combustion region of the torch. The oxidizer, which is oxygen in this case, is introduced in a similar way as in earlier designs through a series of orifices surrounding the fuel-powder mixture. A photograph of the 5P-II handheld torch is given in Fig. 7.4. According to Oerlikon-Metco, such a torch can operate using either acetylene or hydrogen as fuel with a nominal operating power of 35 kW.

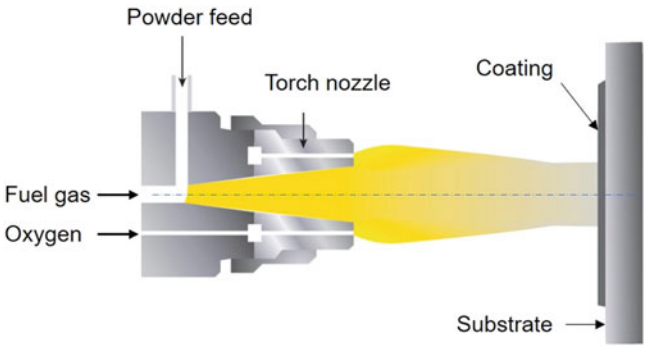

Fig. 7.3 Schematic of the Oerlikon-Metco Flame Powder Spraying torch. (Courtesy of Oerlikon-Metco)

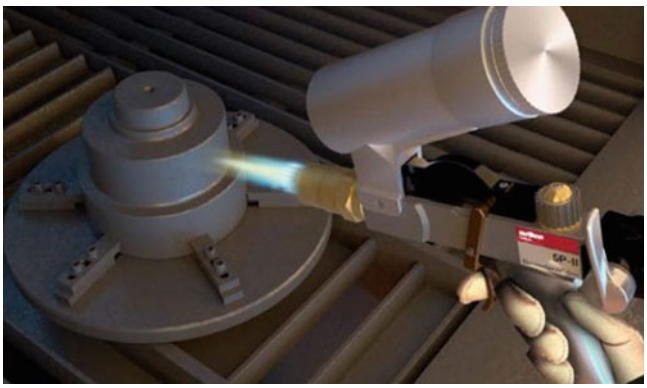

Fig. 7.4 Photograph of the hand-held Oerlikon-Metco Flame Powder Spraying torch. (Photograph Courtesy of Oerlikon-Metco)

Fundamental studies of the flow and temperature fields in low-velocity powder flame spraying (FPS) systems were reported by Nylén and Bandyopadhyay (2000), Bandyopadhyay and Nylén (2003)]. A simplified, and not to scale, schematic representation of the torch configuration used in their study is shown in Fig. 7.5.

The cooling air is injected through an outer ring of orifices. The pre-mixed acetylene-oxygen mixture (22 slm C_2H_2 + 34 slm O_2) was fed through a ring of 16 orifices (0.8 mm in internal diameter) around the nozzle rim, yielding a symmetric flame geometry, while the powder is transported by argon through a central axial channel. The diffusion combustion of the fuel extends in a free jet projecting the particles on the substrate located at 20 cm from the nozzle exit.

The mixture of the reacting gas flow was modeled using the standard k-ε turbulence gas model. In the derivation of this model, it is assumed that the flow is fully turbulent, and the effects of molecular viscosity are negligible. To accurately model the combustion process with reasonable computational effort, single- or multi-step reduced-reaction chemistry models could be used. The choice of this turbulence model also enables the use of the eddy-dissipation model as a competing mechanism for species creation/destruction, together with the Arrhenius finite-rate mechanism. As the process involves chemical reactions, and fast-moving and turbulent gas flow, a generalized finite rate formulation was applied. This approach is based on the solution of the species transport equations for reactants and product concentrations, based on the general chemical reaction given in Eq. 7.1. The gas temperature and velocity fields obtained by this relatively simple, single general chemical reaction simulation are closely comparable with those predicted by significantly more complex multireaction models [Nylén and Bandyopadhyay (2000)]. The convergence time for the simulations without the reversible reactions was significantly shorter, taking only a number of hours instead of a number of days.

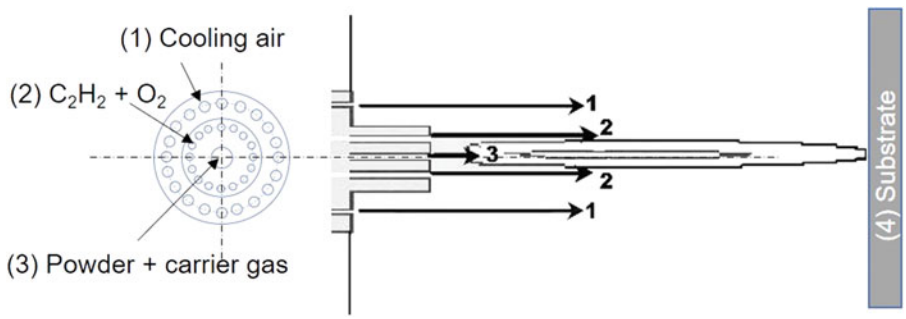

Fig. 7.5 Schematic of the Flame Powder Spraying torch (1) cooling air injected through outer ring of nine orifices at 200 m/s, (2) Fuel-oxygen mix, C2H2/O2 injected through inner ring of 16 orifices at 117 m/s, (3) argon as powder carrier gas at 12 m/s, (4) Substrate [Bandyopadhyay and Nylén (2003)]

Typical results in terms of the gas temperatures and flow fields in the flame are given in Fig. 7.6a and b, respectively. These show an average flame temperature above 2600 °C, while gas velocities are typically below 100 m/s. Bandyopadhyay and Nylén (2003) also calculated and measured the velocities and temperatures of nickel-covered bentonite particles (5–120 μm) *(Metco 312 NS)* injected axially into the flame. The results given in Fig. 7.7a show the probability distributions of particle velocities in the flame prior to their impact on the substrate. The dark bar chart provides data measured using a DPV-2000 system [Bandyopadhyay and Nylén (2003)], while the dotted lines refer to the results of the simulation study. The two sets of results are in reasonable agreement with the experimental distribution, showing a pronounced peak at a particle velocity of 22 m/s. The simulated distribution has a somewhat less pronounced peak, but this also occurs around 22 m/s. The measured distribution has a wider range than the results of the simulation with a small number of particles having velocities exceeding 30 m/s. The corresponding particle temperature distributions are given in Fig. 7.7b. Both measurement results and simulations are also in reasonable agreement with the distribution obtained by the modeling work showing a particle temperature in the range of 1000 to 2600 K, with a peak at 2300 K. The measured data show a broader particle temperature distribution in the range of 1000 to 3500 K, with a peak value around 2400 K.

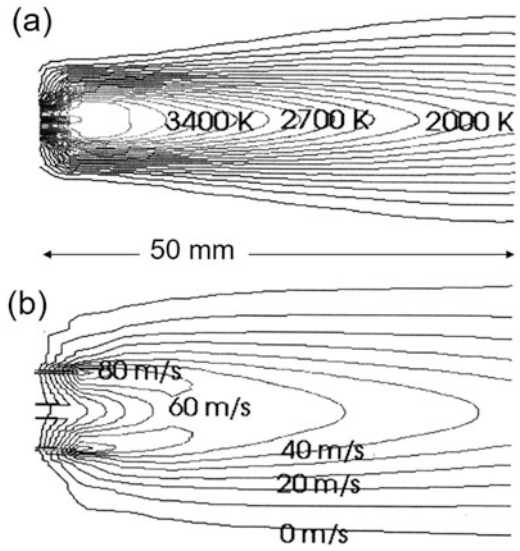

Fig. 7.6 (**a**) Gas temperature and (**b**) flow fields, for an oxy-acetylene flame [Nylén and Bandyopadhyay (2000)]. (Reprinted with kind permission from Springer Science Business Media, copyright © ASM International)

By varying the flow rates of acetylene and oxygen, the flame can be made either oxidizing (fuel lean) or reducing (fuel rich). A reducing-flame limits metal oxidation. The powder is fed either by gravity or preferably with a powder feeder. The carrier gas flow rates, generally argon or nitrogen, have limited influence (a few m/s) on particle velocities, but they increase the spray spot diameter. Reducing the fuel (C_2H_2) and oxygen (O_2) flow rates from 22/34 slm to 18/24 slm results in a reduction of the power dissipated by 21% and the gas velocity by 22%. The corresponding drop of the particle mean velocity is only 13% and that of the mean temperature is 4% [Wigren et al. (1996)]. The highest temperature of NiCrAl/bentonite particles is obtained with a ratio of O_2/C_2H_2 lower than 1.4 (1.6 at stoichiometry) [Wigren et al. (1996)]. As in all spray processes, increasing the powder feed rate has a significant local cooling effect, reducing the flame velocity and temperature (loading effect). The

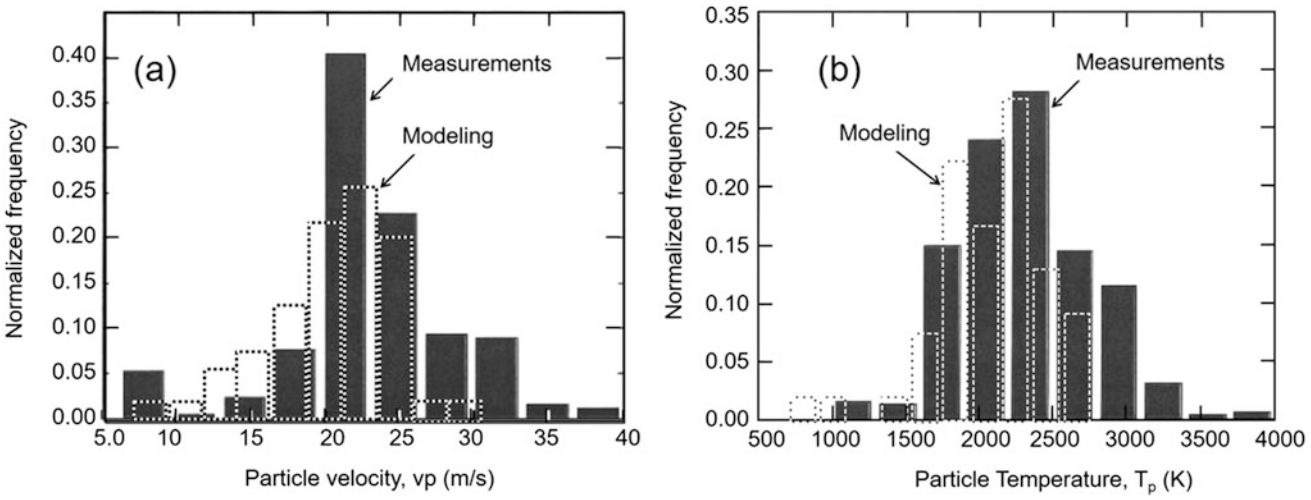

Fig. 7.7 (**a**) Particle velocity and (**b**) particle temperature distributions for Nickel covered bentonite particles (5-120 μm) injected axially into the Oxy-acetylene combustion flame. Dark bar-chart correspond to measurements, while the dotted lines correspond to the results of the modeling work [Bandyopadhyay and Nylén (2003)]. (Reprinted with kind permission from ASM International)

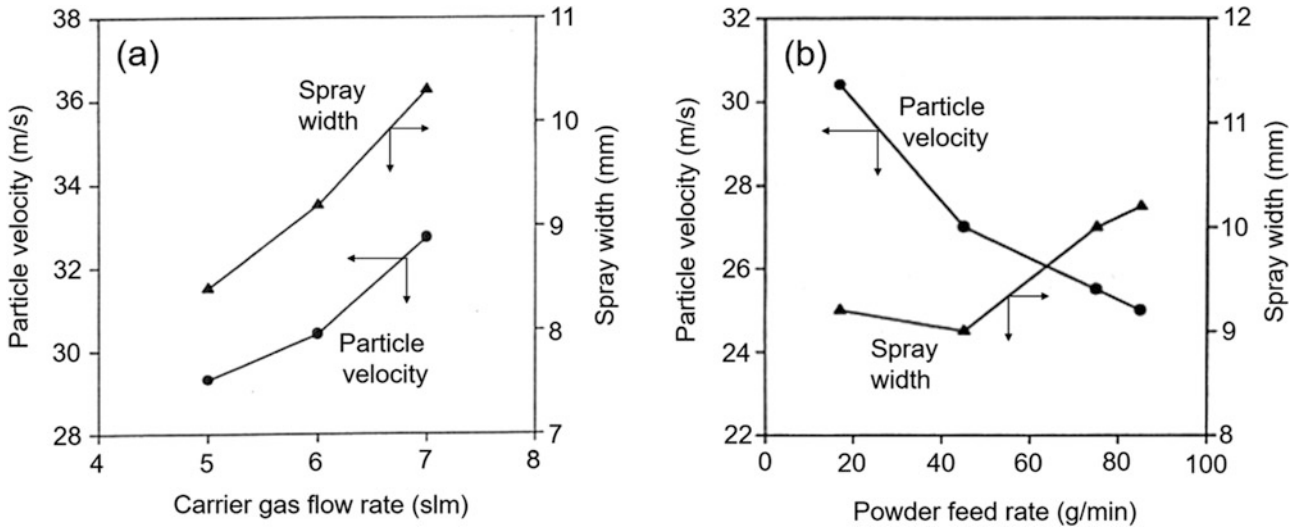

Fig. 7.8 (**a**) Effect of carrier gas flow rate (N2), on particle velocities and spray width, powder feed rate 17 g/min and (**b**) Particle velocities and spray width as function of the powder feed rate. Metco 6PII with 7C-M nozzle (18 slm C2H2 + 28 slm O2) [Wigren et al. (1996)]. (Reprinted with kind permission from ASM International)

results given in Fig. 7.8a [Wigren et al. (1996)] show that increasing the powder carrier gas flow rate gives rise to a slight increase of the particle velocity and an increase of width of the spray spot. Increasing the powder feed rate, on the other hand, Fig. 7.8b, results in a significant drop of the particle velocities, mostly due to the thermal loading effect, and an increase of the width of the spray spot.

[Hall et al. (2010)] studied the heating and acceleration of particles feed stock with an oxy-fuel flame. As for other spray processes, coating microstructure and properties strongly depend on particle velocities and temperatures at impact. They reviewed the different process factors affecting particle temperature and velocity. They showed that multiple process inputs, especially torch hardware, can significantly affect particle temperature and velocity distributions in the powder flame spray process.

7.2.2.2 Applications

As mentioned earlier, powder flame spraying (PFS) has been widely used for a large number of applications. Examples are given in this section of some of the most important and developing applications. These are presented based on the nature of the sprayed material.

(a) ***Metals:***

Mainly those that are easy to melt (Pb, Ag, Zn, Al, Al-12 wt % Si, Al - 5 wt % Mg, Al-Zn, Cu and Cu alloys: Cu-10 wt % Al, Cu-10 wt % Zn, Cu-40 wt % Zn, Cu-30 wt % Zn, Cu-5 wt % Sn, Ni, Ni-20 wt % Cr, steel (0.1 wt % C or 0.1 wt % Cr, 0.25 wt % C, 0.4 wt % C, 0.8 wt % C) and Mo [Rodriguez et al. (2007), Panossian et al. (2005), Paredes et al. (2006), Vijaya Babu et al. (1996), Brantner et al. (2003), Laribi et al. (2006)].

[Babu et al. (1996)] tested flame-sprayed molybdenum to enhance the performance of engineering components such as pistons, piston rings, and shafts. Microstructural studies were conducted on the sprayed coatings and the changes in the microstructure with different spraying conditions were correlated with the strength variations of the coatings.

[Planche et al. (2005)] sprayed NiCrBSi powder successively with plasma, flame spraying and HVOF process. The coatings were characterized in term of microstructure and composition, hardness, Young's modulus, porosity, and oxide level. The results revealed significant modifications in coating properties depending on the spray process used. Comparing the particle characteristics obtained with the different processes allows to better understand the properties of the formed coatings and to investigate the causes of coating quality changes. Differences were interpreted based on in-flight diagnostic results.

[Sakata et al. (2007)] described microstructure control aimed at improving the wear-resistance properties of Co-based (Co-Cr-W-B-Si) self-fluxing alloy coating by diffusion treatment. The treatment of thermally sprayed Co-based self-fluxing alloy coating on steel substrate was carried out at 1370–1450 K for 10–100 min under an Ar gas atmosphere. This diffusion treatment temperature substantially improved the abrasion resistance of the coating.

[Bergant and Grum (2009)] studied the properties of NiCrBSi coatings, produced by a two-step process of flame deposition followed by a furnace post-treatment. Based on

the evaluation of coating properties, the best overall quality was obtained after remitting at a peak temperature 1080 °C with 5 minutes of holding time, followed by slow air cooling.

[Huang et al. (2014)] studied aluminum-alumina composite coatings obtained by flame spraying for potential marine applications against corrosion and wear. Microstructure examination suggested dense coating structures and the evenly distributed alumina splats formed a hard skeleton connecting individual Al splats. The anti-corrosion and wear performance of the coatings were enhanced significantly by the presence of alumina. Failure analyses of the coatings after accelerated corrosion testing disclosed the intact alumina skeleton, which prevented further advancement of the corrosion.

[Navidpour et al. (2017)] considered the potential photoactivity of zinc ferrite, extensively used as a photocatalytic material. They synthesized zinc ferrite powder using mechanical alloying of hematite and zinc oxide at a molar ratio of 1:1, followed by sintering and crushing the alloy for deposition by flame spraying on 316 stainless-steel plate. They concluded that the zinc ferrite coating deposited by flame spraying possesses high photo-absorption properties as well as sufficient photoactivity under visible-light irradiation.

(b) ***Self-Fluxing Alloys:***

These contained Si and B (e.g., CrBFeSiCNi), which are used as deoxidizers with a reaction of the type:

$$(FeCr)_xO_{x+y} + 2\,B + 2\,Si \rightarrow x\,Fe + x\,Cr + B_2O_x.SiO_y \tag{7.5}$$

$B_2O_x.SiO_y$ is a borosilicate. This process requires a thermal post treatment of the coating involving a "fusing" step carried out over 1040 °C using an oxy-acetylene torch which is well suited to reheat the coating. Other means can be used such as a furnace, induction (if the part diameter is almost constant), and lasers. This "fusing" treatment excludes treating coatings on aluminum alloys! During reheating, oxide diffuses toward the coating surface where it is mechanically removed (turning, milling…). The process results in rather dense and hard coatings [Lin and Han (1998), Navas et al. (2006), Sakata et al. (2007)]. These self-fluxing alloys can be reinforced with hard ceramic particles such as CrC [Harsha et al. (2007)].

[Lin and Han (1998)] investigated the process of boriding of flame-sprayed coatings. The combination of flame-spraying and boriding has been shown to improve the mechanical properties, especially the surface properties, of steels. The flame-spray process offered good workability, whereas boriding enhanced the hardness, wear resistance, and corrosion resistance of the surface, thus optimizing the surface properties. Different boriding media, boriding temperatures, and times were investigated.

(c) ***Composites:***

[*Torres* et al. (2009)] fabricated, using oxyacetylene, thermal spraying aluminum matrix composites reinforced with more than 50 vol.% of SiC particles. The sprayed material consisted of mixtures of aluminum powder with 60–85 vol.% of SiC particles. To favor the processing of the composite, in some cases, the SiC particles were coated with silica following a sol-gel route. This allowed for obtaining as-sprayed samples with thickness above 2 mm and with porosity values below 2%. Post-processing of the samples by hot pressing allowed to reduce further the porosity of the composites and to enhance their microstructural homogeneity.

[Wang et al. (2009)] made a TiC-reinforced Ni-based composite coating by flame spraying a mixture of titanium, nickel, and sucrose (to carbonize the sucrose source of carbon). The carbon obtained by pyrolysis of sucrose was a reactive constituent as well as the binder in the composite powder. The titanium and nickel particles were bound by the carbon to form granules of the composite powder. This powder feedstock was used to prepare in situ TiC-reinforced Ni-based composite coating by oxyacetylene flame spraying. The TiC-Ni composite coating was made of TiC, Ni, and some Ni_3Ti. In the coating, a mass of fine TiC particles was uniformly distributed within the metallic matrix. The microhardness and surface hardness of the coating were, respectively, 1433 $HV_{0.2kg}$ and 62 ± 6 (HR30N). The wear resistance was much better for the TiC-Ni composite coating than for the substrate and Ni60 coating.

[Zhang et al. (2014)] deposited on 1045 carbon steel by a flame spraying and melting processing NiCr alloy coatings with 0.5, 1.0, 1.5 and 2.0 wt.% of La_2O_3. The effect of La_2O_3 addition on the tribological properties of the coatings was investigated under dry sliding wear conditions. The result showed that the microstructure of the NiCr alloy coatings is refined with proper amounts of La_2O_3, and the microhardness and wear resistance of the coatings show best enhancement with 1.0% La_2O_3.

(d) ***Reactive Spraying:***

TiC cermets were obtained using asphalt as a carbonaceous precursor. The powder is made by mixing ferrotitanium powder and asphalt at 300 °C, which is heated for 2 h at 600 °C under argon atmosphere (asphalt being completely carbonized). The resulting porous mass is then crushed to form a flame sprayable powder. In situ reactions form TiC particles, which are fine, spherical, and uniformly

dispersed in the coating [Liu et al. (2002), Liu and Huang (2005)].

TiC-Fe fine-grained multiphase and multilayer coatings, composed of alternate TiC-rich and TiC-poor lamellae with different microhardness, can be obtained by reactive flame spray technology using ferrotitanium and graphite as the starting materials. Liu et al. (2002) found that parameters related to the melting and reaction of the reactive micro-pellets are the factors influencing the hardness of TiC-rich layers. A high hardness can be favored by more titanium reacted with graphite (that is, less Fe content and more C/Ti atomic ratio within the reactive micro-pellets), smaller micro-pellets and properly longer spray distance. Fe content (or the expected TiC content) and spray distance are the main parameters to affect the microstructure of the coatings.

[Hui Yuan Liu and Jihua Huang (2006)] prepared a kind of Ti–Fe–C compound powder for Reactive Flame Spray (RFS), using ferrotitanium and asphalt, which was used as the origin of carbon in the mix. The agglomerated Ti-Fe-C compound spraying powder was prepared by heating a mixture of ferrotitanium and asphalt to pyrolyze the asphalt. The TiC/Fe cermet coating prepared by RFS showed high hardness and wear resistance properties. The surface hardness of the TiC/Fe cermet coating was 65 ± 6 (HR30N). In the same fretting conditions, the wear area of the Ni60 coating is much more than that of the TiC/Fe cermet coating.

[Wang et al. (2009)] made a Ni-Ti-C composite powder for reactive thermal spraying by heating a mixture of titanium, nickel, and sucrose to carbonize the sucrose, which is used as the source of carbon. The carbon obtained by pyrolysis of sucrose was a reactive constituent as well as the binder in the composite powder. The titanium and nickel particles were bound by the carbon to form granules of the composite powder. This powder was used to prepare in situ TiC-reinforced Ni-based composite coating using oxy-acetylene powder flame spraying. The TiC-Ni composite coating is made of TiC, Ni, and some Ni_3Ti. In the coating, a mass of fine TiC particles was uniformly distributed within the metallic matrix. The microhardness and surface hardness of the coating were, respectively, 1433 HV 0.2 kg and 62 ± 6 (HR30N). The wear resistance was much better for the TiC-Ni composite coating than for the substrate and Ni60 coating.

(e) ***Photocatalytic Zinc Ferrite:***

Considering its potential photoactivity, zinc ferrite has been extensively used as a photocatalytic material. Navidpour et al. (2017) presented investigation with zinc ferrite powder synthesized using mechanical alloying of hematite and zinc oxide powder at a molar ratio of 1:1 sintered and crushed for deposition by flame spraying on a 316 stainless-steel plate. Solutions were employed to study the photocatalytic activity of the coating. They concluded that the zinc ferrite coating deposited by flame spraying not only possessed high photo-absorption ability, but also exhibited sufficient photoactivity under visible-light irradiation.

(f) ***Polymers***:

To reduce the risk of overheating or burning of polymer particles, flame spray guns were modified by equipping them with an air or nitrogen distributor that could be used to inject cold air or nitrogen inside the combustion zone (see Fig. 7.9a). The cold gas flow acts as a buffer zone between the flame and the particle protecting them against overheating.

The heating and fusing operation of polymer particles using flame spray guns remains; however, a challenge due to the inherently low thermal conductivity of polymers (< 0.5 W/m.K), resulting in high temperature gradients within coating [Gawne et al. (2001)], and the transient heat flux imparted to the coating surface must be carefully controlled.

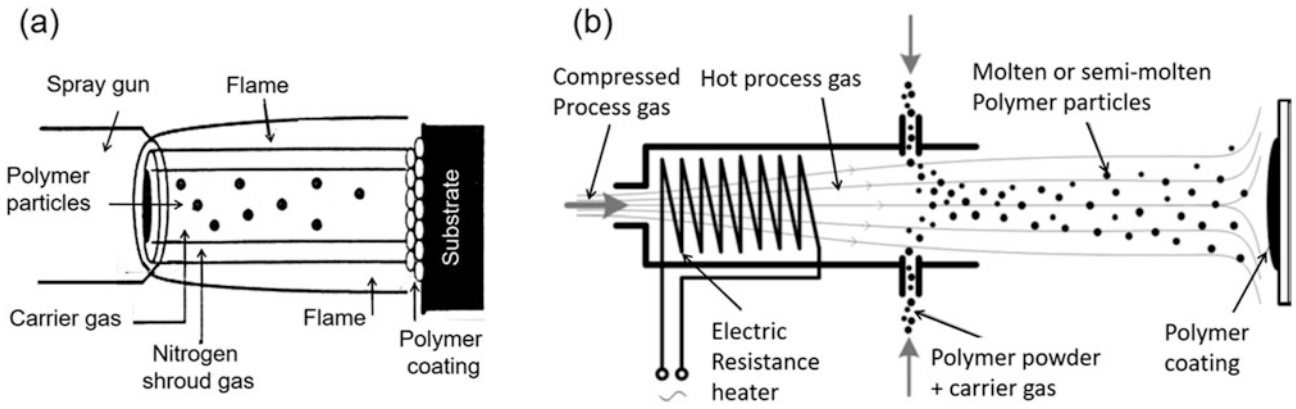

Fig. 7.9 (**a**) Modified flame spray gun for polymer particles spraying [Ivosevic et al. (2009)] (**b**) Resistively heated gas spray gun used for polymer spraying [Ivosevic et al. (2007)]. (Reprinted with kind permission from ASM International)

The limitations of the combustion-based processes for thermal spray of polymers were the motivation of Ivosevic et al. (2009) for the development of a low-temperature spray process called polymer thermal spray (PTS) based on the resistive heating of the process gas in the spray gun. A schematic of such a PTS torch is given in Fig. 7.9.*b*. An electro-resistive heating element is used to heat the main process gas, either pure air, nitrogen, an inert gas, or a mixture. The electric heating element can be set to the required temperature depending on polymer properties. The velocity of the main process gas at the nozzle exit can be adjusted in the range of 20 to 60 m/s. It controls particle in-flight residence time as well as the intensity of forced convection heat over the substrate and/or previously deposited coating layers. Polymer powder is injected downstream of the main process gas heating module using an appropriate carrier gas (see Fig. 7.9.*b*). PTS guns were developed for operation at power levels of 6 kW and 18 kW.

On the other hand, deposition of metallic coatings on elastomeric polymers is a challenging task due to the heat sensitivity and soft nature of these materials and the high temperatures in thermal spraying processes [Ashrafizadeh et al. (2016)]. They employed a flame spraying process to deposit conductive coatings of aluminum-12 silicon on polyurethane elastomers. They found that the coating porosity and electrical resistance decreased by increasing the pressure of the air injected into the flame spray torch during deposition. The latter also allowed the reduction of the stand-off distance of the flame spray torch. They found that the spray process did not significantly change the storage modulus of the polyurethane substrate material.

[Chebbi and Stokes (2012)] studied flame-sprayed biocompatible polymer coatings, made of biodegradable and non-biodegradable polymers as single coatings on titanium and as top coatings on plasma-sprayed hydroxyapatite. Biocompatible polymers can act as drug carriers for localized drug release following implantation. The polymer matrix consisted of a biodegradable polymer, poly-hydroxybutyrate 98%/poly-hydroxy valerate 2% (PHBV), and a non-biodegradable polymer, poly-methyl-methacrylate (PMMA). They studied the effects of spray parameters on coating characteristics (thickness, roughness, adhesion, wettability) and optimized the coating properties accordingly. They showed that optimized flame-sprayed biocompatible polymers underwent little chemical degradation and did not produce acidic by-products in vitro and that cells proliferated well on their surface.

[Gonzalez et al. (2016)] made a review of the deposition of metals onto polymer-based structures to enhance the thermal and electrical properties of the resulting metal-polymer material system. They explored the polymer surface preparation methods and the deposition of metal bond-coats. The objective of their review was devoted to the potential applications of thermal-sprayed metal coatings deposited onto polymer-based substrates. Their review aimed to summarize the state-of-the-art contributions on the thermal spray metallization of polymer-based materials, which has gained recent attention for potential and novel applications.

(d) ***Glass:***

Refractory glass such as (Al_2O_3-Y_2O_3-BiO_2) has been flame sprayed onto stainless steel where it formed hard, uniform and well-adherent coatings [Sainz et al (2008)]. The properties of these coatings were comparable to the bulk properties of glasses of the same composition. Patents, especially in Japan, were also granted for the flame spraying of a wide range of glasses and enamels [Masataka and Kazumi (1989); Koji et al (1990); Hideki et al (1991); Tatsuya et al (1988)]. Bio-glass has been sprayed by Lugsheider et al. (1995), and the spraying of enamels on substrates prone to decompose has been reported by Arcondéguy et al (2007). According to Arcondéguy et al. (2007) and Zhang et al. (2000), the success of these applications requires a close control of the heat flux to the coating/substrate during the spraying operation, and significant reduction of residual stresses in the coating during subsequent cooling down stage.

According to Arcondéguy et al. (2007), mechanisms occurring during glaze-coating manufacturing by flame spraying may differ from those usually encountered when considering more traditional materials such as oxides or even carbides. Indeed, the coating results from the coalescence of molten particles and is manufactured in one pass rather than the stacking of individual lamellae in multiple passes. It is, therefore, important to estimate the thermal flux transmitted from the torch to the substrate, as it has to be high enough to improve the particles' spreading and wettability without leading to thermal decomposition of the substrate nor to the development of unacceptable levels of residual stresses.

7.2.3 Solution Flame Spraying (SFS)

Solution flame spraying (SFS) is a variant of powder flame spraying which has been introduced in the mid-1990s. Its novelty is in the use of a liquid feedstock, whether pure liquid, solution, or suspension, which is atomized and injected in an oxygen-hydrogen or oxy-acetylene flame where the liquid phase is evaporated, and thermo-chemical reactions produce fine or nanometer-sized particles [Tikkanen et al. (1997)]. According to these authors, atomization is optimized with an organic solvent, such as isopropanol, nebulized with hydrogen gas at a high flow rate. Liquid droplets injected into the flame are subjected to a maximum temperature of 2600 °C and are accelerated to

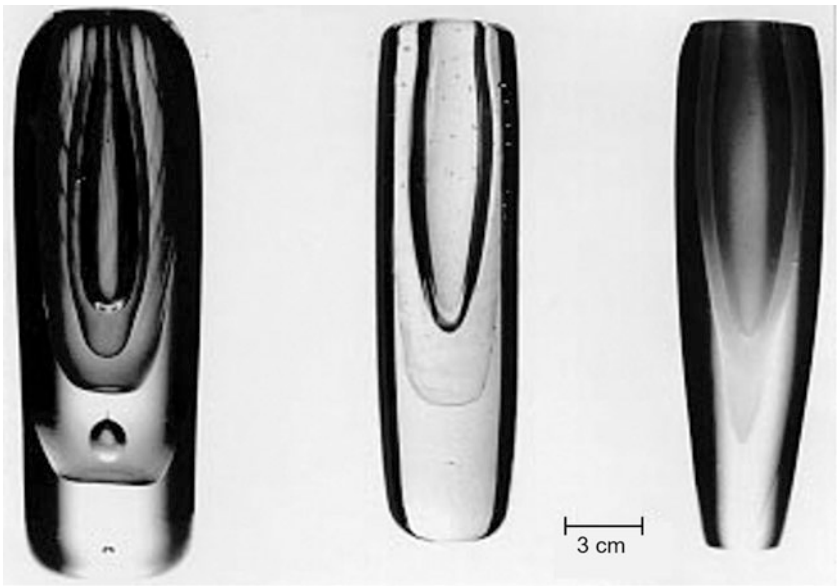

Fig. 7.10 Blue, blue-green, and yellow colored glassware produced by glass blowing. The light blue-green color indicates the weak but eloquent coloring effect of copper ions [Gross et al. (1999)]

about 160 m/s. The flame length can be controlled by flame velocity and the type of solvent. Water produces a shorter flame, whereas isopropanol extends the flame. Injection of the aerosol produces a "pencil-like" region that does not experience turbulence for most of the flame length. Experimentation with manganese nitrate and aluminum iso-propoxide or aluminum nitrate showed conversion to a manganese oxide and alumina, respectively. The process was used for glass coloring by flame spraying Co, Cu, and Ag nitrates dissolved in alcohol or water. After evaporation, precursors are transformed into oxides and sprayed onto soda-lime silica glass at 900 °C to 1000 °C. This process has produced blue, blue-green, and yellow colors [Gross et al. (1999)]. Figure 7.10, unfortunately in black and white, shows colored glass vases produced by glass blowing. The process was also used to deposit finely structured or nanostructured coatings: zirconia, starting from zirconium oxy-acetate precursor gas atomized in the flame [Poirier et al. (2003)] and nanostructured TiO_2 coatings.

[Poirier et al. (2003)] combined the atomization of a colloidal suspension with the lateral injection of the aerosol in a flame, aerosol flame spraying (AFS). The aerosol droplets were partially dried when crossing the flame and then deposited as a coating onto a substrate. Afterward, the coating was consolidated by heat treatment without extensive grain growth. They also modeled the trajectories, acceleration, and vaporization of the droplets to predict the impact conditions of the in-flight dried particles, their size, and water content when they impinge onto the substrate.

The reactive flame-sprayed deposition of photocatalytic nanostructured TiO_2 coatings was reported by Yang et al (2005) using a 30 wt.% solution of butyl titanate in pure ethanol. The formed nanostructured TiO_2 deposit, which was mostly in the anatase phase, could be transformed to rutile by annealing at temperatures above 400–500 °C. The grain size of rutile phase obtained was, however, larger than that of anatase. Moreover, it was noted that while the deposits annealed at temperatures below 450 °C were photocatalytically active, those annealed at 500 °C became photocatalytically inactive in spite of the fact that they contained 95% anatase crystal structure.

7.2.4 Wire, Rod, and Cord Spraying

7.2.4.1 Spray Gun Design and Process Characteristics

Wire, cord, and rod fed devices, as illustrated in Fig. 7.11, use air turbines or electrical motors, built into the torch, that power drive rolls, which pull feedstock from the source and push it through the nozzle at a controlled velocity. If the velocity is too high, the tip of the wire cannot melt because its residence time in the flame is too short. The uniform motion of the wire, adapted to the gas composition, flow rate, and the wire diameter and composition, is the key issue. Typical gas flow rates are as follows: 10 to 30 slm acetylene, 20 to 100 slm oxygen, and up to 17 slm (1 m^3/h) air for atomization of the molten tip.

Typical wire velocities, depending on the wire material, are between 0.6 and 14 m/min. Higher speeds are used to spray lower-melting-point metals such as Babbitt, tin, and zinc. Figure 7.12 shows the details of the nozzle of the gun.

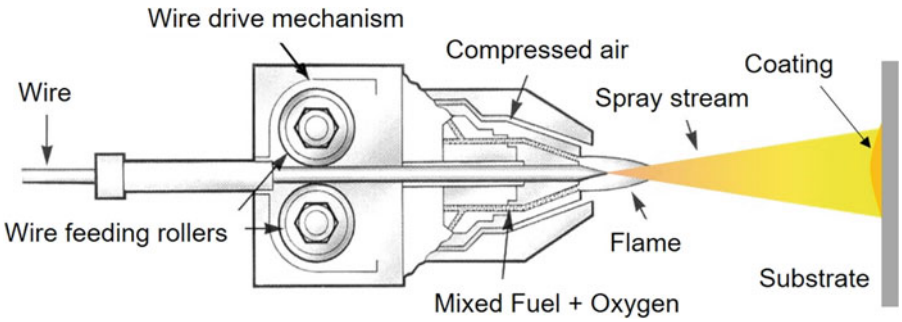

Fig. 7.11 Schematic of a Wire, Rod, or Cord Flame Spray gun [Thermal Spraying (1985)]. (Courtesy of Metallisation Flamespray Dudley, Pear Tree Lane, West Millands, DY2 OXH, England)

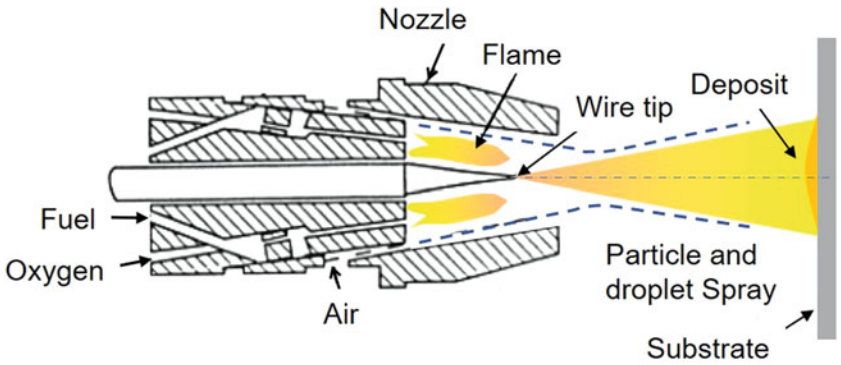

Fig. 7.12 Details of the nozzle design for a Wire, Rod, or Cord Flame Spray gun [Thermal Spraying (1985)]. (Reprinted with kind permission from American Welding Society)

Fig. 7.13 Photograph of the Oerlikon-Metco 16E Wire Flame Spray gun. (Photograph Courtesy of Oerlikon-Metco)

The nozzle produces and shapes the flame and guides the wire along its axis. This nozzle can be changed to adapt to wires of different diameters. In Fig. 7.12, the conical shape of the tip can be observed. Assuming that the liquid metal is withdrawn by the atomization gas as soon as it forms, a constant gas temperature and heat transfer coefficient result in a conical wire tip (cone angle of 25 to 30°), as observed experimentally. A photograph of an Oerlikon-Metco Model 16E Wire Flame Spray gun is shown in Fig. 7.13. Different models of this gun are offered for operation with different types of wires (Hard or soft), standard and high wire speeds, using acetylene, propylene, or propane as gaseous fuel.

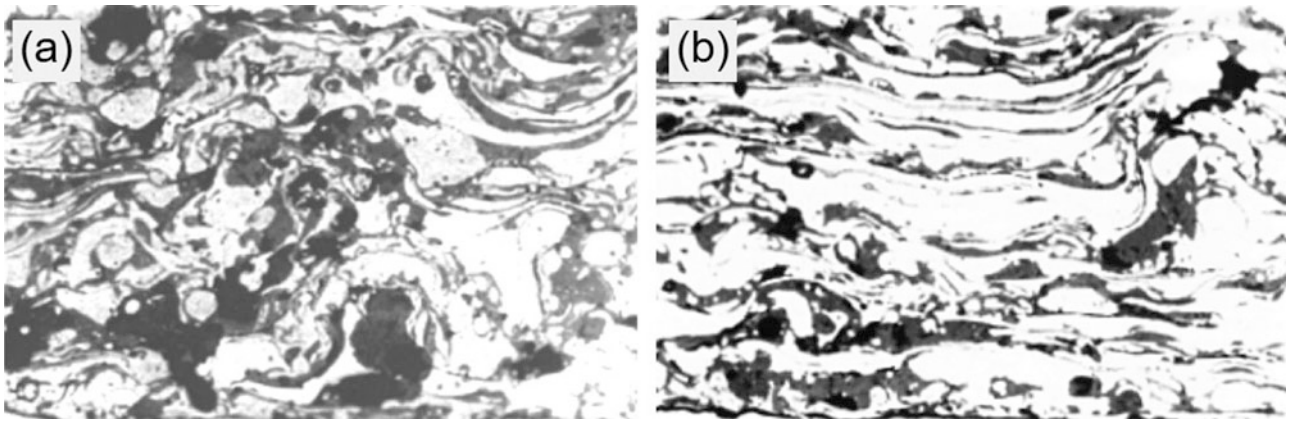

Fig. 7.14 Cross-sections of Wire Flame Sprayed Aluminum Coating (**a**) air atomized (**b**) nitrogen atomized

Typical wire diameters used are between 1.2 and 4.76 mm. They must be clean and smooth with a precise dimensional uniformity (between 0.01 and 0.05 mm). They are stored in coils, spools, or barrels. Wire feed rates depend on sprayed materials and wire diameters, for example: Al: 2–8 kg/h, Zn: 8–30 kg/h, Steel: 2–4.5 kg/h and Mo: 0.7 to 2.5 kg/h.

Particles are produced by the flow of compressed atomizing gas (generally air or nitrogen), which creates liquid metal sheets that become self-aligned in the flow (see *Fig. 11.5* of Chap. 11, pictures obtained for wire arc spraying). Waves are created at the sheet surface due to hydrodynamic instabilities, forming protuberances and inducing sheet disintegration. The flapping motion of the sheets creates showers of drops, which increases the divergence angle. The large eddy structures formed in the flow also modify particle trajectories, as shown by Hussary et al. (2007) for wire arc spraying (Chap. 11).

Coatings obtained by this process generally have high porosity (~ 10%) and can be highly oxidized, for example, to more than 25% for air atomized Al. As can be observed in Fig. 7.14, this oxidation can be reduced by a factor 2 when using nitrogen instead of air. However, considering the flow rates of the atomization gas needed, this solution is rather expensive.

Wire flame sprayed (WFS) coatings are extensively used for corrosion protection, in the automotive industry (Mo on piston rings and for "rain drop erosion" of piston heads), against aqueous corrosion [Ishikawa et al. (1999)] with Al and 80 Ni-20 Cr coatings. However, because of the coating porosity, coatings to be used for corrosion resistance must be sealed using, for example, epoxy or silicone if the service temperature is relatively low (< 200 °C) [Ishikawa et al. (2001)]. Finally, the process is rather economical and simple; it has high deposition rates (10–40 kg/h) and very good thermal efficiency to melt metals (60–70%). Moreover, substrate heating by the flame is limited.

Alternately, WFS can also be used with rods or cords (referred to Rod FS or Cord FS). The process developed by Rokide®, now Saint Gobain®, aimed at the adaptation of the flame spraying technology to the spraying of ceramics. The ceramic particles to be used were sintered to form a rigid rod (diameters between 3.17 and 6.35 mm) and continuously feed into the flame in the same way as the WFS technology, at feed rates between 10 and 20 cm/min (1.5 to 3 mm/s). Unfortunately, due to the limitation of 608 mm, on the length of the rod, the spray cycle is limited to an operation between 3 and 6 min, after which the operation has to be stopped for rod replacement. The problem was partially overcome through the use of cords which are made of ceramic particles agglomerated with either an organic binder (the evaporation or decomposition of which starts at 250 °C and is completed at 400 °C), or a mineral binder [$Al(OH)_3$ that remains up to 1500 °C]. The diameters are the same as those of rods, but the cord length can reach 120 m, which extends the cycle time to 10 to 20 h. The sprayed ceramics are mainly alumina, chromia, titania, zirconia (with calcia, magnesia, yttria as stabilizer) zircon, and alumina-titania. Spray conditions are similar to those of wires.

7.2.4.2 Applications

The materials sprayed are:

- ***Pure metals***: Al 99 wt %, Cu (99.5 and 99 wt %), Mo (99.5, 99 and 98 wt %), Sn, Zn (99.95 wt %).
- ***Alloys***: Cobalt, Copper, Nickel base, MCrAlY (cored wires), NiAl.
- ***Carbide Cermets (cored wires)***: Cr_3C_2 with Fe and FeC, WC/W2C + Fe, WC/TiC + Fe, Cr, Ni *Steels*: low carbon and stainless steel (ductile), Bronze + Al or NiAl.
- High-velocity flame spraying.

7.3 High-Velocity Flame Spraying

High-velocity flame spraying encompasses HVOF, which stands for "High Velocity Oxy-Fuel," in which the spray gun is fed with combustible gas or liquid fuel and oxygen, while HVAF stands for "High Velocity Air-Fuel," where oxygen is replaced by air, resulting in lower temperatures and higher gas velocities.

7.3.1 Basic Concepts

7.3.1.1 Spray Gun Design and Process Characteristics

Union Carbide (now Praxair Surface Technology) introduced the HVOF process in 1958 though it was not really commercialized until the early 1980s, when the Jet Kote (Deloro Stellite) system was introduced by Browning J.A. (1983). The principle of the Jet Kote system, shown schematically in Fig. 7.15a, consists in feeding a high volume of combustible gases into a water-cooled pressurized combustion chamber. The exit of this chamber is at right angle to the exit nozzle. The powder is introduced through a water-cooled central injector on the axis of the gas stream in the throat region [Thorpe and Richter (1992)]. The design of the axial flow HVOF torch shown in Fig. 7.15b was developed further through the introduction of water cooling, which improved the robustness of the torch and its thermal efficiency while maintaining axial powder injection [Ishikawa et al. (2001)]. As with the Jet Kote type gun, axial injection of the powder implies using a pressurized powder feeder. In the torch design presented in Fig. 7.15c, the combustion chamber is still co-axial with the nozzle, but the powder is injected radially beyond the throat at the beginning of the barrel or in the divergent part of the nozzle. Downstream of the throat, the pressure is much lower than in the combustion chamber upstream of the nozzle throat. Injecting powders at this point simplifies the process allowing, if necessary, multiple powder injection ports for a more uniform loading of the exit stream and efficient use of the available energy. Generally, operating data show that at least twice the spray rate per unit of energy can be achieved with radial injection versus axial injection. Moreover, this design has allowed increasing the combustion gas pressure (up to 0.8–0.9 MPa).

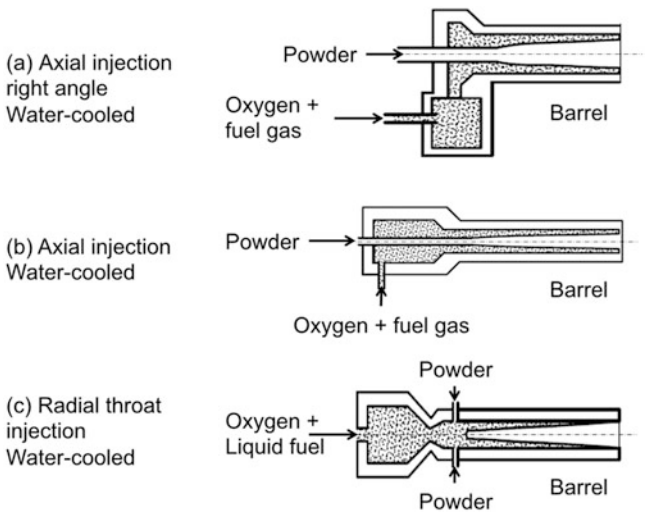

Fig. 7.15 Typical design evolution of HVOF guns (**a**) Principle of the Jet Kote, (**b**) Axial injection in the combustion chamber, (**c**) Axial chamber with radial powder injection [Thorpe and Richter (1992)]. (Reprinted with kind permission from Springer Science Business Media, copyright © ASM International)

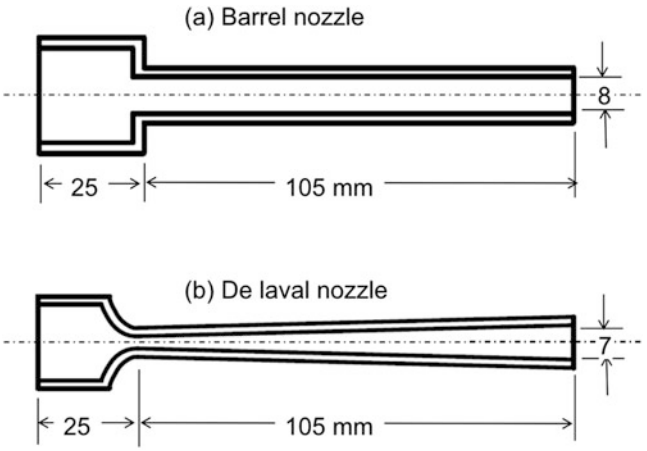

Fig. 7.16 (**a**) Barrel and (**b**) de Laval nozzles. Dimensions given in millimeters [Korpiola et al. (1997]. (Reprinted with kind permission from Springer Science Business Media], copyright © ASM International)

As in all spray processes, when a hot gas exits in the ambient air, the hot jet cools down rather fast due to its expansion and the entrainment of the surrounding air. To impede this phenomenon, it has been proposed to extend the nozzle by a water-cooled barrel (up to 30 cm long), where some energy of the jet is lost to the walls of the barrel but much less than through mixing with the ambient air. Of course, this also requires that particles are not over-heated, or remain below the melting temperature, to avoid deposition on the barrel wall. Korpiola et al. (1997) have shown, based on the 1-D compressible flow model, that with the replacement of a simple straight barrel by a de Laval nozzle, with a divergent section of the same length as the barrel, Fig. 7.16, the gas velocities increased by about 300 m/s, Fig. 7.17. They have also shown that the gas velocity at the exit plane depends on the fuel/oxygen ratio, while the combustion velocity is almost independent of the total gas flow at a constant fuel/oxygen ratio. Typical working pressures are in the range of 0.3–0.6 MPa.

7.3.1.2 High-Power HVOF

Almost simultaneously, guns with the general designs of Fig. 7.15b and b were developed using a liquid fuel such as kerosene instead of combustible gas and oxygen, allowing very high dissipated powers (almost 300 kW). With these guns, powders can also be injected radially downstream of the torch throat. Such high-power guns result in large thermal stresses and oxidation of gun components, particularly the combustion chamber and nozzle, for which the water-cooling must be carefully designed. However, the use of a liquid fuel allowed for a significant increase of the torch power, simplifies the spraying process, improves operational safety, and decreases costs without degrading operational parameters. Examples of commercially available gaseous and liquid-fueled HVOF torches are given in Fig. 7.18, provided courtesy of Oerlikon Metco. Both torches are water-cooled, with axial powder injection in the case of the torch for gaseous fuel, Fig. 7.18a, and radial injection of the powder in the case of the liquid-fueled torch given in Fig. 7.18b. A photograph of the Woka-star 610 liquid-fueled torch is given in Fig. 7.19. According to Oerlikon-Metco, this type of torch is rated for operation at power levels of 293 kW.

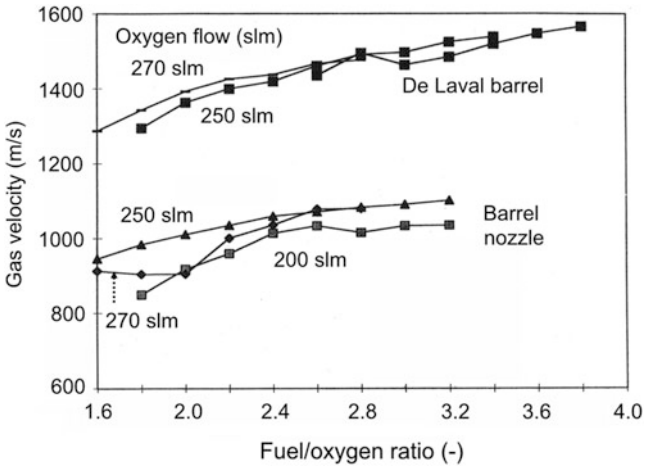

Fig. 7.17 Gas velocity at the exit plane of the HVOF spray gun (H2/02), for different fuel/oxygen ratios) for the two types of gun design: combustion chamber followed by (a.) barrel, (b.) convergent-divergent (de Laval) nozzle (see Fig. 7.16) [Korpiola et al. (1997]. (Reprinted with kind permission from Springer Science Business Media, copyright © ASM International)

7.3.1.3 Evolution of the HVOF Gun Design

The spraying of many metallic or cermet materials (mostly with carbides) using HVOF is sensitive to particle oxidation and partial decarburization, which must be eliminated or at least significantly reduced in order to avoid compromising the quality of the coating. Dedicated efforts deployed over the past two decades toward this objective have led to the development of numerous innovative solutions and design modifications of the standard HVOF gun. In the following, a brief review is given highlighting some of these design proposals that have been widely accepted and used for a wide range of applications. These mostly aim at reducing the gas temperature, increasing its velocity, and protecting the particles as much as possible from exposure to the oxidizing atmosphere.

(a) ***High-Velocity Air Fuel (HVAF) gun.***

The HVOF design given in Fig. 7.15c has allowed J. W. Browning [Browning (1992)] to develop the high-velocity air

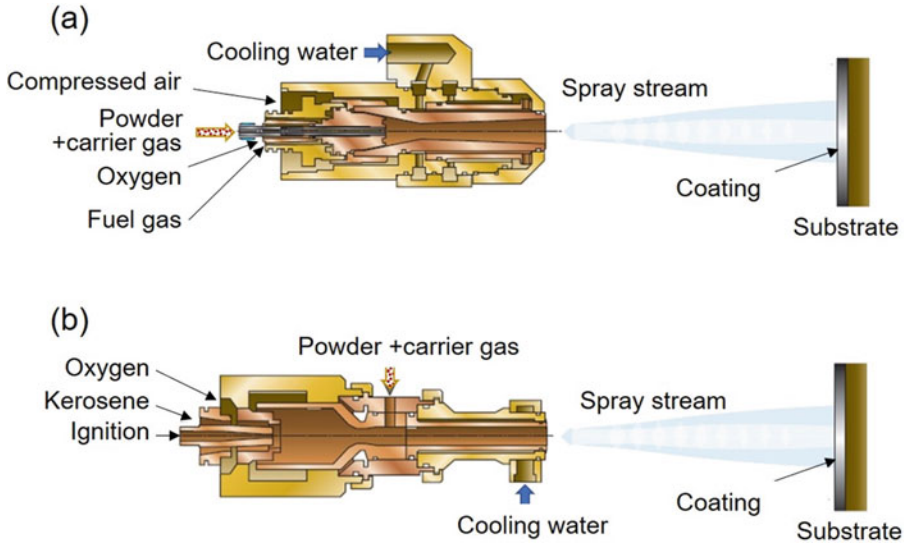

Fig. 7.18 Typical design of the Oerlikon-Metco, HVOF spray guns (**a**) water-cooled, gaseous fuel gun, (**b**) water-cooled, liquid-fueled gun (Schematics Courtesy of Oerlikon-Metco)

Fig. 7.19 Photograph of the Oerlikon-Metco Woka-star 610 Liquid Fuel HVOF gun, Power rating 293 kW (Schematics Courtesy of Oerlikon-Metco

fuel (HVAF) process in which he replaced the oxygen by air as oxidant. This required an increase of the oxidant gas flow rate by a factor of five for the same fuel/oxygen ratio. Nitrogen in the air, which does not participate in the combustion, must be heated, resulting in lower flame temperatures and higher gas velocities. The pressure in the combustion chamber in this case is over 0.8 MPa with airflows in the 8–10 m^3/min range (for an HVOF gun of the first generation, gas flow rates are below 1 m^3/min), giving rise to very high gas velocities (up to 2000 m/s) [Browning (1999)]. Lower temperatures and higher velocities are beneficial to limit particle oxidation. Moreover, the gun can be cooled by the airflow, and its efficiency can reach 90%. Flame ignition is generally made with pure oxygen. For example, [Evdokimenko et al. (2001)] calculated the temperature in the chamber of an HVAF gun working at 1 MPa with three different gases at stoichiometric composition: with hydrogen T = 2383 K, with methane T = 2267 K and finally with kerosene T = 2321 K.

According to Matikainen et al. (2018), particle heating and acceleration in the HVAF spray process can be efficiently controlled by changing the nozzle geometry. They sprayed fine WC-10Co-4Cr and Cr_3C_2–25NiCr powders with three different nozzle geometries (cylindrical exit diameter d = 19 mm, convergent-divergent with d = 22.5 mm, convergent-divergent with d = 26 mm) to investigate their effect on the particle temperature, velocity, and coating microstructure. Their results showed that:

- Changing the HVAF nozzle geometry from cylindrical to convergent–divergent increased the particle velocities while maintaining the particle temperature.
- Heating, melting degree, and the resulting carbide dissolution and de-carburization were effectively controlled by different nozzle geometries.
- Higher particle velocity increased the HVAF-sprayed coating hardness and cavitation erosion resistance with WC-10Co_4Cr feedstock.
- HVAF-sprayed WC-10Co_4Cr and Cr_3C_2–25NiCr coatings demonstrated significantly improved cavitation erosion resistance compared to other HVOF spray processes and bulk materials.

(b) ***Gas Shrouded (GS-HVOF) and Warm Spray (WS-HVOF) guns.***

Gas shrouding is an efficient solution for the protection of the sprayed powder from contact with oxygen in the ambient air, which is engulfed into the HVOF high-velocity jet at the exit of the spray gun. It does not protect, however, the particles from oxidation by any excess oxygen in the fuel-oxygen mixture, or from partial decarburization due to excessive heating. Dilution of the combustion products by an inert gas allows, on the other hand, for the independent control of the temperature and velocity of the spray jet. An interesting review of HVOF process development is this area was reported by Kuroda et al. (2011), in which they identified shrouding and inert gas injection, proposed by Ishikawa et al. (2005), and Kawakita et al. (2006), as a viable option for the reduction of the contact of the sprayed particle with oxygen, reduction of the flame temperate, and increase of the flame velocity.

A schematic of the three HVOF torch designs considered are given in Fig. 7.20. These include, in Fig. 7.20a, a standard high-pressure HVOF (JP5000) gun design as a basis for comparison. An example of a gas-shroud attachment developed by Ishikawa et al. (2005) is given in Fig. 7.20b, which is identified as GS-HVOF. The attachment consists of a cylindrical tube added at the exit nozzle of the spray gun, which offers provision for the injection of the shroud gas through a

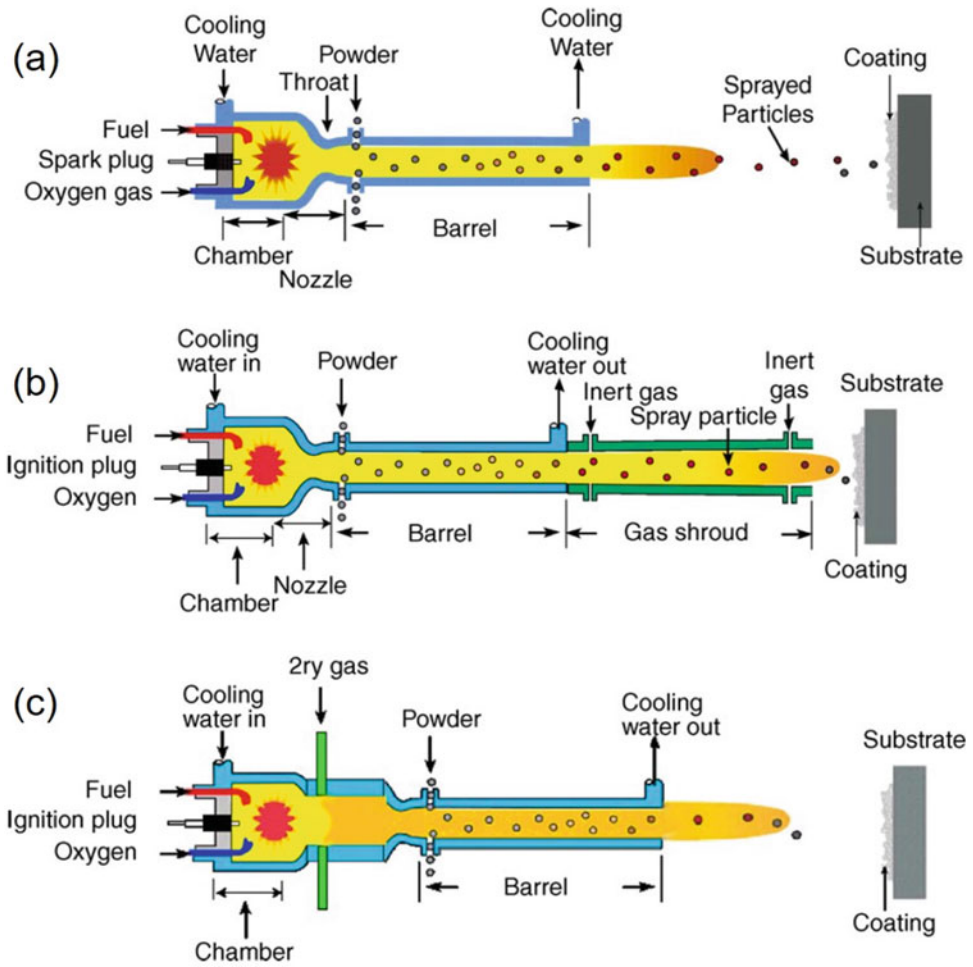

Fig. 7.20 Schematic of (**a**) commercially available high-pressure HVOF (JP-5000) gun, (**b**) gas shrouded (GS-HVOF) gun, (**c**) two-stage HVOF gun with inert gas injection identified as warm spray (WS-HVOF) gun. Guns [Kuroda et al. (2011))]. (Reprinted with kind permission from Springer Science Business Media, copyright © ASM International)

set of annular holes in its wall. The gas shroud set-up has two important effects on (WC-Co) particles injected into the flow; mean particle velocities are increased (with a reducing flame at a pressure of 0.72 MPa) from 760 m/s to 850 m/s with the shroud, while their mean temperatures drop from 1950 °C to 1830 °C. Accordingly, the density of the sprayed WC-Co coating was improved, the degree of decomposition of WC dropped from 6% to 2.5%, and coatings showed superior corrosion and wear resistance properties compared to those obtained in the absence of a shroud.

An alternative to shrouding proposed by Kawakita et al. (2006) referred to as warm spray (WS-HVOF) is based on the addition of a mixing chamber between the combustion chamber and the nozzle, as shown in Fig. 7.20c. The combustion gas generated is mixed with an inert gas such as nitrogen to lower its temperature. The objective is to limit the gas temperature between 1000 and 2300 K. Compared to the HVAF process, dilution of the combustion gases with nitrogen gives more flexibility to tailor temperatures and velocities by adjusting the nitrogen flow rate. Typical working conditions for a modified JP-5000 gun are the following: kerosene from 0.29 to 0.35 L/min (17.4–21 L/h), oxygen between 0.55 and 0.73 m^3/min, nitrogen from 0.5 to 2 m^3/min. When spraying titanium on a steel substrate using the modified torch design, dense coatings were obtained, which provide excellent corrosion protection in seawater in a laboratory test for over one month [Kawakita et al. (2006)]. The results clearly reveal the effectiveness of controlling the temperature and the composition of the gas environment where the titanium or titanium-alloy powder is being sprayed. Cooling of the jet flame prior to injection of the powder allowed a reduction of the oxygen content of the resulting coating to the level of the titanium feedstock, suggesting this process might compete with cold spraying [Kuroda et al. (2011)].

Figure 7.21 shows the variation in the oxygen content in the titanium coating and coating porosity with the nitrogen flow rate [Wu et al. (2006)]. The gas cooling and the resulting lower particle temperatures led to a decrease of the oxidation

level from 5.4 wt.% at 500 slm N_2 to 0.22 at 2000 slm (spray distance 280 mm). Over 1000 slm (N_2), the porosity of the coating increases with large average pore sizes because particle temperatures become too low, and particles lose their plasticity and deformability at impact. Thus, as usual, a compromise must be found.

(c) ***Low-Temperature (LT-HVOF) gun.***

The low-temperature (LT-HVOF) gun proposed by *Lin* et al. *(2014)* was developed from the conventional kerosene-fueled HVOF spraying system GTV-K2 by reducing the critical diameter of the nozzle at the exit of the combustion chamber in order to increase the pressure of the combustion chamber and consequently the velocity of the gases at the exit of the spray gun. A schematic of the LT-HVOF gun is given in Fig. 7.22. In this process, the flow rate of the hot gas in the combustion chamber was controlled to be relatively low through the restriction of the exit nozzle diameter. The plume of the modified process has a higher velocity compared to the conventional HVOF spray process. With the increase of the plume velocity, the heating time of particles decreased, resulting in a decrease of the heat transferred to the spray powder. The kerosene feed rate was reduced from 0.43 L/min (26 L/h) for a conventional HVOF gun to 0.18 L/min (11 L/h) for the LT-HVOF gun. The corresponding oxygen feed rate to the LT-HVOF gun was 88 m^3/h, compared to 90 m^3/h for a conventional HVOF gun. The combustion chamber pressure increased from 0.85 MPa for conventional HVOF to 1.55 MPa for the LT-HVOF. Results from this study *[Lin* et al. *(2014)]* demonstrate that the deposition mechanisms of the LT-HVOF process are closely related to the particle size of the feedstock materials and that the LT-HVOF process is a feasible way to spray dense TiNi composite coatings, on stainless steel 316 L substrate, with low oxygen content combined with the utilization of large-sized Ni-clad Ti powders.

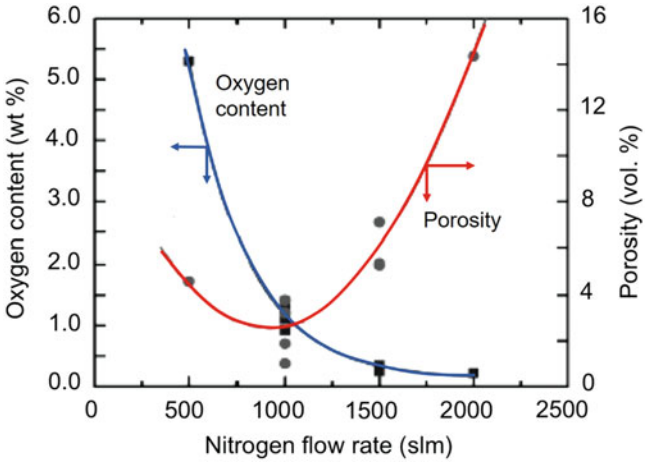

Fig. 7.21 Dependence of titanium (average particles size 28 μm) coating oxygen content and porosity on nitrogen flow rate, sprayed with the gun depicted in Fig. 7.20c [Wu et al. (2006)]. (Reprinted with kind permission from ASM International)

(d) ***Liquid Injection (LT-HVAF) gun.***

To reduce the HVAF process temperature and particle oxidation further, the injection of a liquid such as water, downstream of the nozzle, but upstream of the powder injection port, as shown in Fig. 7.23, was proposed [Yuan et al. (2006)]. The evolution of the gas temperature and velocity in such a process, referred to as LT-HVAF, as a function of the water injection rate, is given in Fig. 7.24. The results are based on computer modeling for operating using 5.47 kg/h (6.8 L/h) kerosene and water injection rate varying between 20 and 30 kg/h (20−30 L/h). Considering the high latent heat of evaporation of water, it is not surprising under these conditions to observe the rapid decrease of the gas temperature and velocity to the 600–700 K and 700–800 m/s range, respectively. It is to be noted that as the gas temperature and velocity continues to drop, the ability to use such flame for the spraying of metals and ceramics diminishes. With a water injection flow rate of 20 kg/h, the characteristics of the flame approaches essentially those of the cold spray process.

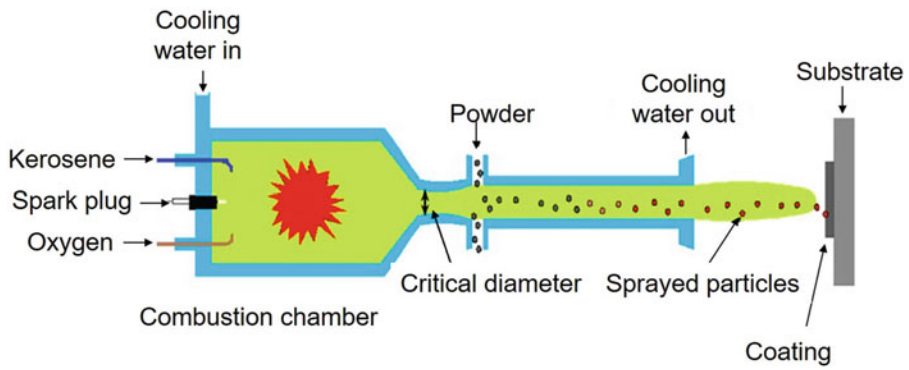

Fig. 7.22 Schematic of LT-HVOF gun by reducing the critical diameter of the combustion chamber [Lin et al. (2014)

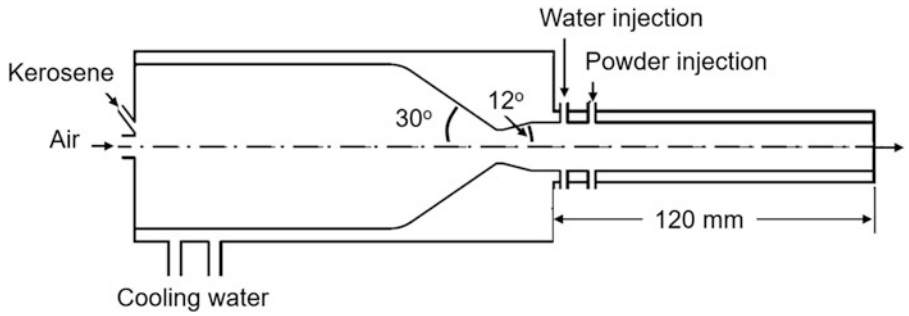

Fig. 7.23 Schematic diagram of low-temperature (LT-HVAF) spraying gun and nozzle with water injection downstream of the nozzle throat [Yuan et al. (2006)]. (Reprinted with kind permission from Springer Science Business Media, copyright © ASM International)

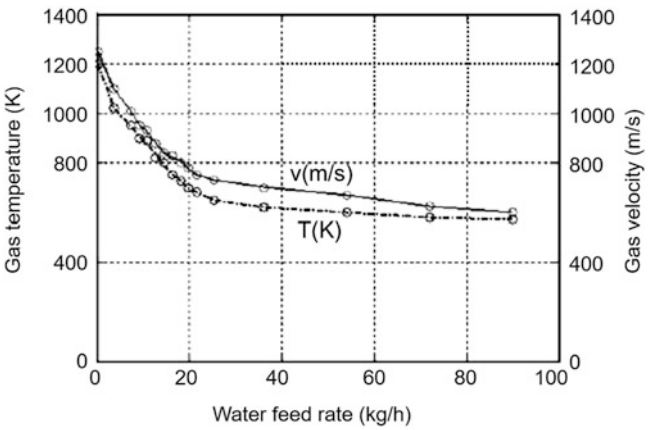

Fig. 7.24 Variation, on a logarithmic scale, of gas the velocity and temperature with water injection rate into the LT-HVAF-gun illustrated in Fig. 7.20 [Yuan et al. (2006)]. (Reprinted with kind permission from Springer Science Business Media, copyright © ASM International)

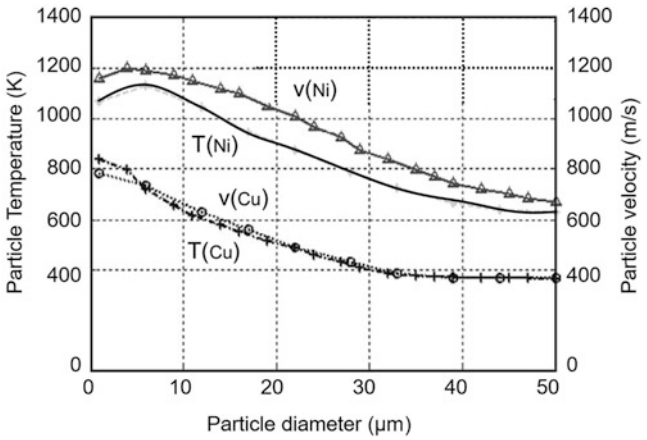

Fig. 7.25 Copper and nickel particle behavior at LT-HVAF gun exit with water injection [Yuan et al. (2006)]. (Reprinted with kind permission from Springer Science Business Media, copyright © ASM International)

In their study, Yuan et al. (2006) also computed individual particle trajectories and temperature history for copper and nickel particulate with diameter in the range of 2 to 50 μm for the same operating conditions in the presence 20 kg/h of water atomized into the flow. The particle velocities and temperatures at the gun exit are given in Fig. 7.25 as a function of the particle diameter. These show maximum copper particle temperatures of 1200 K for particles less than 10 μm in diameter, dropping down to 650 K for 50 μm particles. The corresponding velocities for copper particles are 800 m/s for less than 10 μm particles down to 400 m/s for 50 μm particles. Slightly lower particle temperatures are observed for nickel with essentially the same velocities as for that of copper particles. It is to be noted, however, that in none of these two cases, the particle temperatures remain below the corresponding melting temperature of the particles, T_m for copper being 1357 K and that for Nickel 1728 K.

7.3.1.4 Gas and Particle Dynamics in HVOF Systems

As discussed earlier, HVOF/HVAF systems can be operated using either gaseous or liquid fuels. The typical gaseous fuels used include Hydrogen, acetylene, methane, propane, and propylene. Liquid fuels include kerosene and possibly liquid propane. As an oxidizer, oxygen or air is commonly used. The typical velocities at the exit of the nozzle can be as high as 1900 m/s. Such flows generate oblique shock waves and shock diamonds, as seen in Fig. 7.19 and Fig. 7.26. The diamonds are brighter because of higher local pressure and the temperature in those regions.

Much effort has been devoted to the study and modeling of the flow and temperature fields in HVOF/HVAF jets. These varied from simple isentropic 1-D models [Thorpe and Richter (1992)] and [Korpiola et al. (1997] to 3-D supersonic compressible flow models [Tawfik and Zimmerman (1997)]. The chemical reaction involved,

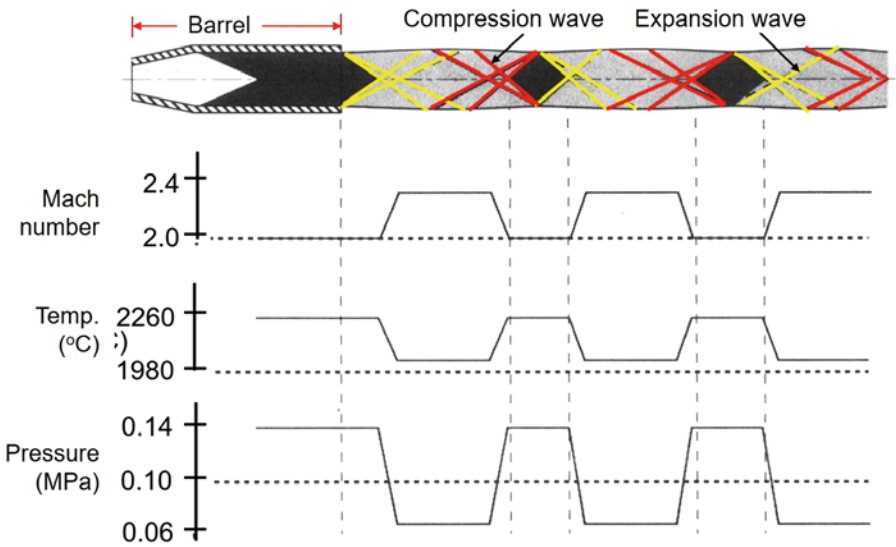

Fig. 7.26 Schematic of oblique shock waves at the barrel exit of an HVOF gun together with axial velocity (Mach number), temperature, and pressure distributions [Thorpe and Richter (1992)]. (Reprinted with kind permission from Springer Science Business Media, copyright © ASM International)

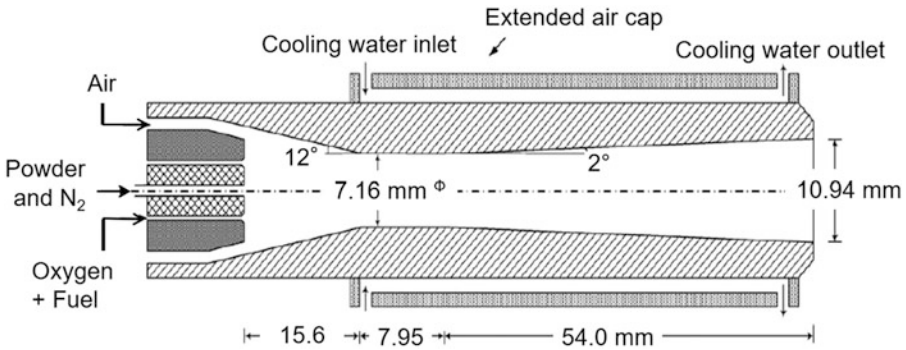

Fig. 7.27 Schematic diagram of the diamond jet hybrid thermal spray gun [Li M. and P. D. Christofide (2006)]. (Reprinted with kind permission from Elsevier)

which is a rather complex problem, is generally treated by an approximate, single-step, general formulation as follows [Oberkampf and Talpallikar (1996a)], [Oberkampf and Talpallikar (1996b)]:

$$C_xH_y + z\,O_2 \rightarrow y_1\,CO_2 + y_2\,CO + y_3\,H + y_4\,H_2 + y_5\,H_2O + y_6\,O + y_7\,OH \tag{7.6}$$

where x, y, z, and y_i are stoichiometric coefficients, which depend on the chemical composition of the hydrocarbon fuel (C_xH_y) used. Oberkampf and Talpallikar (1996a), Oberkampf and Talpallikar (1996b) were the firsts who suggested this approach. In general, modeling results match rather well with experimental results, as for example the pressure variation along the centerline of the nozzle. It should be pointed out that in a typical de Laval nozzle configuration, with convergent/divergent expansion sections, the flow is ideally expanded if the pressure at the nozzle exit, p_e, is equal to the ambient pressure in the surrounding atmosphere, p_a (i.e., $p_e = p_a$). It is, however, known to be underexpanded if $p_e > p_a$, and overexpanded if $p_e < p_a$.

Typical results from [Li and Christofides (2005)] are presented to illustrate possibilities of 2-D models developed for the diamond jet hybrid gun. A schematic diagram of the torch is given Fig. 7.27, which is of the type shown in Fig. 7.15b.

The propylene fuel gas used in this case is mixed with oxygen through a siphon system, and fed to the air cap, where they react to produce high-temperature combustion gases. The exhaust gases, together with the air injected from the annular inlet orifice, expand through the nozzle to reach supersonic velocity. The air cap is cooled by both water and air ("hybrid") to prevent it from melting. It is assumed that the walls of the torch are maintained at a constant temperature of 400 K. The powder particles are injected at the axial powder feed channel in the inlet nozzle using nitrogen as the carrier gas. The different gas flow rates are the following: propylene 83 slm, oxygen 273 slm, air 404 slm, nitrogen carrier gas 13.45 slm; the total mass flow rate of the gaseous feed is 18.10 g/s. The flame richness ratio, R', see Eq. 7.2 [$R' = (\text{fuel/oxygen})/(\text{fuel/oxygen})_{St}$, is 1.045, reflecting a slight excess of propylene.

First, a 1-D simplified model formulation was used by the authors [Li and Christofides (2005)] to calculate the chamber pressure. A chemical equilibrium code developed by Gordon and McBride (1994) was next used to define the reaction formula (see Eq. 5.5) for the given partial pressures of oxygen and propylene. Subsequently, the CFD 2-D simulation was run and the final pressure compared with the one used for deriving the reaction. The trial and error approach shows that the chamber pressure is about 0.6 MPa and the partial pressures of oxygen and propylene are about 0.34 MPa. The results obtained are presented in Fig. 7.28 in terms of the isocontours and profiles, along the centerline of the torch, for the static pressure, axial velocity, Mach number, and temperature in the internal and external fields, which are given in Li and Christofides (2005). The reaction of the pre-mixed oxygen and propylene results in an increase of gas temperature above 3000 K, and a pressure of 0.6 MPa is maintained. At the exhaust end of the torch, gases expand through the convergent–divergent nozzle, pressure (Fig. 7.28a) decreases, and the gas velocity (Fig. 7.28b) increases continuously. At the throat of the nozzle, the Mach number is close to 1. The gas is accelerated to supersonic velocity in the divergent section of the nozzle and reaches a Mach number of 2 at the exit of the nozzle (Fig. 7.28c). Simulation shows that the pressure at the exit of the air cap is 0.06 MPa, which implies that the flow is over-expanded. The over-expanded flow condition gives a slightly higher gas velocity, and more kinetic energy can be transferred to the powders. It is important to note that although the gas temperature inside of the torch is very high, its value at the centerline is less than that outside of the torch (Fig. 7.28d). This also implies that the external thermal field plays a very important role in particle heating.

The over-expanded flow pattern involved in the HVOF thermal spray process is illustrated in Fig. 7.29 [Li and Christofides (2005)]. At the exit of the nozzle, the shock front begins obliquely as a conical surface and is cut off by a "Mach shock disc" perpendicular to the axis of the flow.

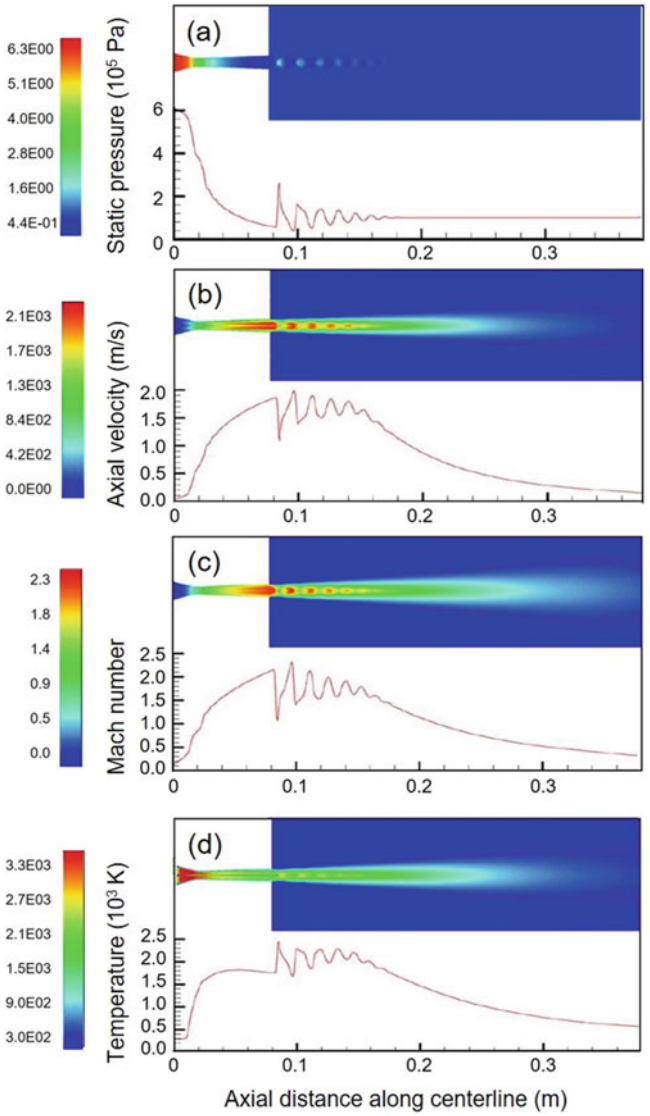

Fig. 7.28 Contours of gas properties (upper plot) and centerline profiles of gas properties (lower plot): (**a**) static pressure, (**b**) axial velocity, (**c**) Mach number and (**d**) static temperature [Li and Christofides (2005)]. (Reprinted with kind permission from Elsevier)

Behind the incident and Mach shock front, a reflected shock front and a jet boundary develop. As the reflected shock front meets the jet boundary, reflected expansion waves develop. These reflected expansion waves converge before reaching the opposite boundaries and give rise to shock fronts, which meet the jet boundary again and the whole process repeats. This periodic jet pattern is eventually blurred and dies out due to the action of viscosity at the jet boundary. It is shown that the gas temperature is relatively low at the exit of the torch (approximately 1800 K). However, passing through the first shock leads to a sharp increase in the gas temperature to around 2500 K. The location of the first shock is 7 mm from the nozzle exit.

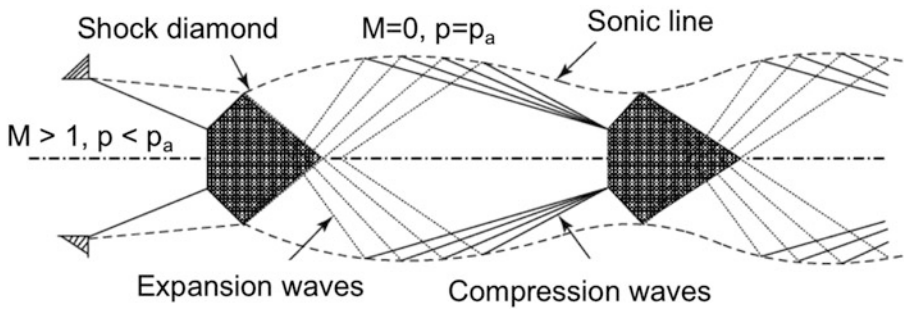

Fig. 7.29 Schematic of wave structure in the over-expanded jet [Li and Christofides (2005)]. (Reprinted with kind permission from Elsevier)

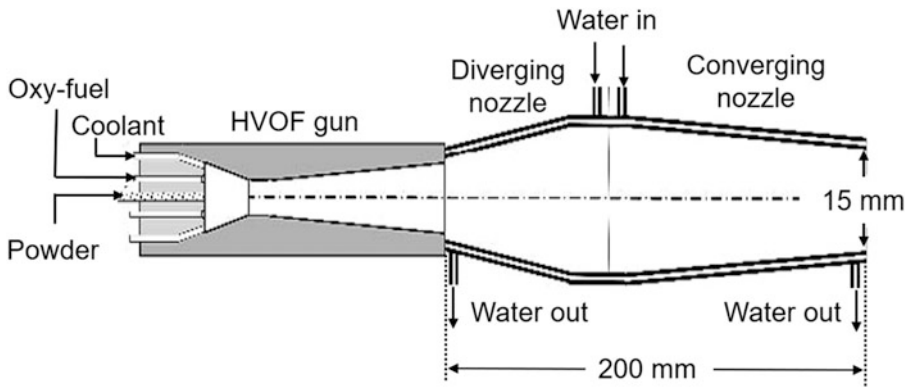

Fig. 7.30 New attachment configurations: Diverging–converging [Dolatabadi et al. (2005)]. (Reprinted with kind permission from Springer Science Business Media, copyright © ASM International)

The main parameters controlling the flow are the nozzle and barrel designs, the choice of gases, the flame richness of the mixture, and the total gas flow rate (often linked to the gas pressure in the combustion chamber).

Extensive modeling studies were dedicated to the nozzle design [Tawfik and Zimmerman (1997), Oberkampf and Talpallikar (1996a, b), Gu et al. (2001), Sakaki and Shimizu (2001), Katanoda et al. (2005), Dolatabadi et al. (2005), Yuan et al. (2006), Li and Christofides (2006)]. Improvements were made in the areas of deposition efficiency, control of in-flight particle oxidation, and flexibility to allow deposition of ceramic coatings. Based on a numerical analysis, a new attachment to a standard HVOF torch, illustrated in Fig. 7.30, was developed, tested, and used to produce thermal spray coatings [Dolatabadi et al. (2005)]. Its performance was evaluated by spraying several coating materials including metal and ceramic powders. Particle characteristics and spatial distribution, as well as gas phase composition, were compared for the new attachment and standard HVOF guns. The attachment provides better particle spatial distribution, combined with higher particle temperature and velocity.

The choice of the fuel/oxygen (F/A) ratio is important for the operation of an HVOF/HVAF system because it controls the gas temperature and the particle oxidation level. For example, calculations by Gu et al. (2001), with a gun, similar to that presented in Fig. 7.15b, working with the mixture C_3H_6-O_2, show that the temperatures that are reached within the combustion chamber vary with the (F/A) ratio. A dependence on the total gas flow rate was also observed with the higher flow rates giving marginally higher combustion temperatures. Compared to the combustion temperature calculated by another author for the same propylene-oxygen mixture at 0.1 MPa, the temperature difference is rather small. Yang et al. (2005) calculated the adiabatic combustion temperature of natural gas (CH_4) as a function of the stoichiometric factor S_t, using different O_2 + air mixtures. The stoichiometric factor S_t, as defined in Eq. 7.3, is the ratio of the oxygen flow rate used to that necessary for the complete combustion of the fuel, that is, its stoichiometric value. The results given in Fig. 7.31 show a maximum adiabatic flame temperature of 3250 K for a (CH_4 + O_2) mixture at Stoichiometric factor $S_t = 0.9$–1.0. With the addition of air (between 50 and 145 slm) to the combustion mixture, with a corresponding decrease of the oxygen flow rate in order to control the S_t values, the maximum flame temperature drops in steps down to 3150 K, while the optimum value of S_t approaches 1.0.

An extensive CFD modeling study of the HVOF process was reported by Cheng et al. (2001) with the objective of providing fundamental understanding of the effect's

controllable experimental parameters on the gas and particle dynamics in the thermal spray process. The study was carried out on the Sulzer-Metco diamond jet gun equipped with a convergent–divergent nozzle, as shown in Fig. 7.27. Since particle loading in the HVOF process is very low, it was assumed that the presence of the particles had a negligible effect on the gas velocity and temperature fields. The model is based on the solution of the corresponding mass, momentum, and energy conservation equations for turbulent flow using the $k - \varepsilon$ formulation, combined with a simplified combustion model as proposed by Oberkampf and Talpallikar (1994, 1996a, b). The study was carried out for a propylene-oxygen mixture with the chemical reaction represented by a simplified single-step equilibrium formulation given by:

$$C_3H_6 + 13.552\ O_2 \rightarrow 1.036\ CO_2 + 1.964\ CO + 0.441\ H + 0.476\ H_2 + 1.937\ H_2O + 0.398\ O + 0.734\ OH \qquad (7.7)$$

The fuel gas (propylene) is premixed with oxygen in the front portion of the gun prior to its injection in the annular gap to the convergent–divergent nozzle where it is ignited. The exhaust gases, along with the compressed air injected from the annular inlet orifice, form a circular flame configuration that surrounds the powder particle input from the central inlet hole. The parameters investigated were essentially the total gas flow rates fed into the HVOF gun and the barrel length. The results are compared to a reference case "REF" corresponding to operation under the recommended manufacturer standard conditions. The composition of the gases used in the four cases studied are given in Table 7.2. These are given in (g/s) for each component with the reference case for a total gas flow rate of 6.94 g/s. The corresponding mass fraction for each component is given as "*REF,* mass fraction." The total gas flow rate for cases *TF1*, *TF2*, and *TF3* varied between 2.28 and 9.21 g/s while keeping the ratio of fuel to oxygen, nitrogen, and air constant, as given in the *REF* case.

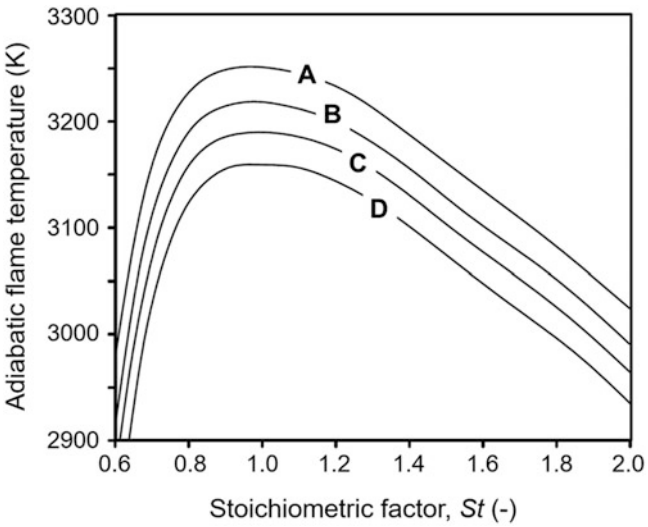

Fig. 7.31 Theoretical adiabatic flame temperatures for different combustion systems at 0.5 MPa (absolute pressure) (**a**) CH4 (200 slm) + O2 (**b**) CH4 (200 slm) + O2 + air (50 slm) (**c**) CH4 (200 slm) + O2 + air (95 slm), (**d**) CH4 (200 slm) + O2 + air (145 slm) [Yang et al. (2002)]. (Reprinted with kind permission from Springer Science Business Media, copyright © ASM)

Results obtained for the reference case (REF) [Cheng et al (2001)], which corresponds to a relatively high total gas flow rate, are given in Fig. 7.32. The exit pressure in this case is higher than the atmospheric pressure and consequently an under-expanded jet is formed. Figure 7.32a shows the Mach number contours over the entire calculation domain. In the convergent portion of the nozzle, the velocity of the gas mixture is low, but is then accelerated to M = 1 at the nozzle throat. In the divergent portion, the gas is further accelerated to a supersonic velocity and reaches M = 2.1 (V = 2032 m/s) at the nozzle exit. It is also noted that as the gases enter the ambient environment, they expand to match the ambient pressure, accelerating to the highest velocity of 2530 m/s. The corresponding gas temperature contours and the flow streamlines are given in Fig. 7.32b and c. These show that the temperature of the gases increases rapidly in the convergent portion of the gun, where the fuel combustion takes

Table 7.2 Relative mass flow rates of inlet gases for different cases compared to those of the standard case after [Cheng et al. (2001)]

Cases	Propylene (g/s)	Oxygen (g/s)	Nitrogen (g/s)	Air (g/s)	Total (g/s)
REF, mass flow rate	1.3	3.05	0.0445	2.55	6.9445
REF, mass fraction	18.72%	43.92%	0.64%	36.72%	100%
TF1	0.43	1.0	0.0101	0.84	2.2801
TF2	0.87	2.04	0.0204	1.71	4.6404
TF4	1.73	4.05	0.0405	3.39	9.2105

Reprinted with kind permission from Springer Science Business Media

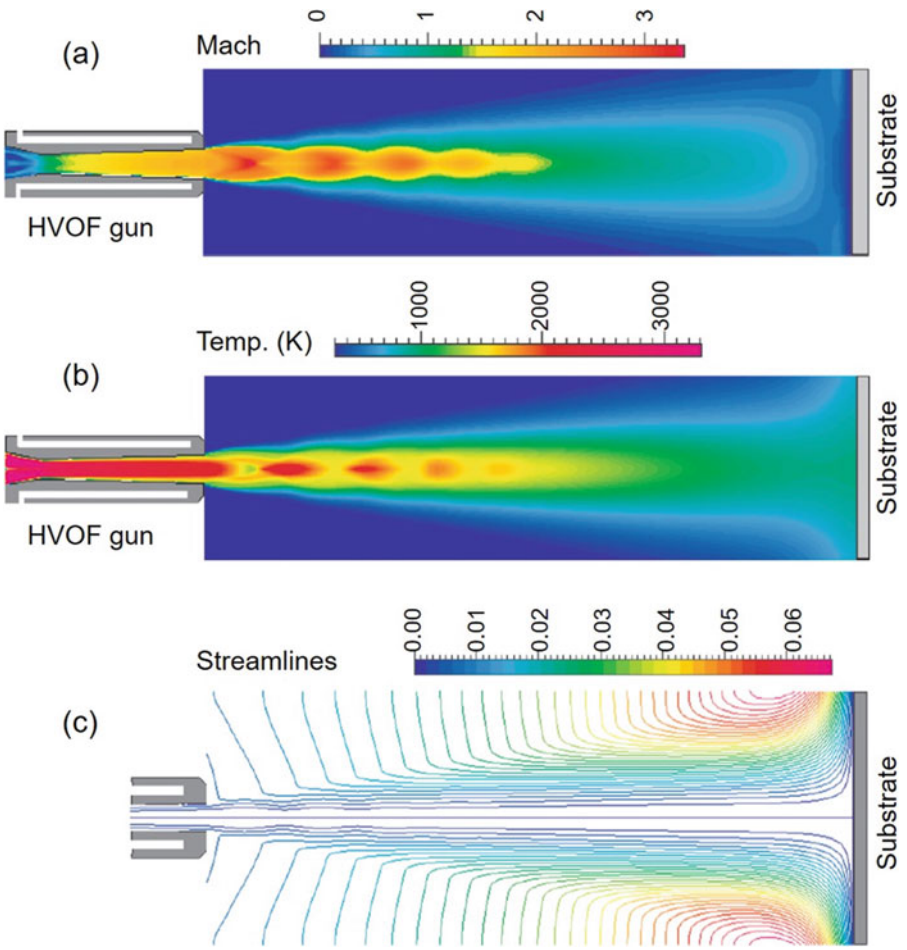

Fig. 7.32 (**a**) Mach number contours, (**b**) temperature and (**c**) streamlines for the HVOF gun with gas flow rates given in Table 7.2, REF case. (propylene-oxygen mixture, Sulzer-Metco Diamond Jet gun) [Cheng et al. (2001)]. (Reprinted with kind permission from Springer Science Business Media)

place, reaching its highest value (about 3200 K) at the throat. As the gases move in the divergent section and exit the torch, their temperature decreases as a result of energy transfer to kinetic energy. Beyond the exit of the torch, the temperature of the gases oscillates as they go through repetitive expansion and compression cycles associated with the creation of shock diamonds. The pattern of expansion and compression waves is repeated until mixing with the entrained ambient atmosphere dissipates the supersonic jet, as shown in Fig. 7.32c, giving the streamlines of the flow.

As reported by Cheng et al. (2001) (Fig. 7.30), increasing the total gas flow rate, cases *TF1*, *TF2,* and *TF3,* has little effect on the gas velocity and temperature inside the nozzle in the range investigated. This implies that the gas flow inside the nozzle is choked. However, the increase in the total gas flow rate leads to a significant increase in the pressure inside the nozzle, as shown in Fig. 7.30a. At the nozzle exit, the pressures on the centerlines reach either positive or negative values with respect to the surroundings. A positive value, obtained for high gas flow rates, indicates that the static pressure is higher than the ambient pressure, as was in the REF case, and that the flow is under-expanded. A negative value indicates, on the other hand, that the static pressure is lower than the ambient pressure and that the flow is over-expanded [Cheng et al. (2001)]. Whatever the flow at the nozzle exit may be, under- or over-expanded, shock diamonds are observed, resulting in velocity and temperature variations along the jet axis, as illustrated, respectively, in Fig. 7.30b and c.

Such temperature and velocity variations can affect the heat and momentum transfers to small particles (below 30–20 μm depending on their specific mass). The shock diamonds and the bow shock created close to the substrate affect mainly the small particles, for example, those below 25 μm for MCrAlY particles [Yang et al. (2002)].

Mathematical modeling has also been a key tool for the study of the gas dynamics in novel HVOF/HVAF devices such as the warm spray (WS-HVAF) gun reported by Kuroda et al. (2011), as described in "*section 7.3.1.3 Evolution of the HVOF gun design*." The study made use of gas dynamic

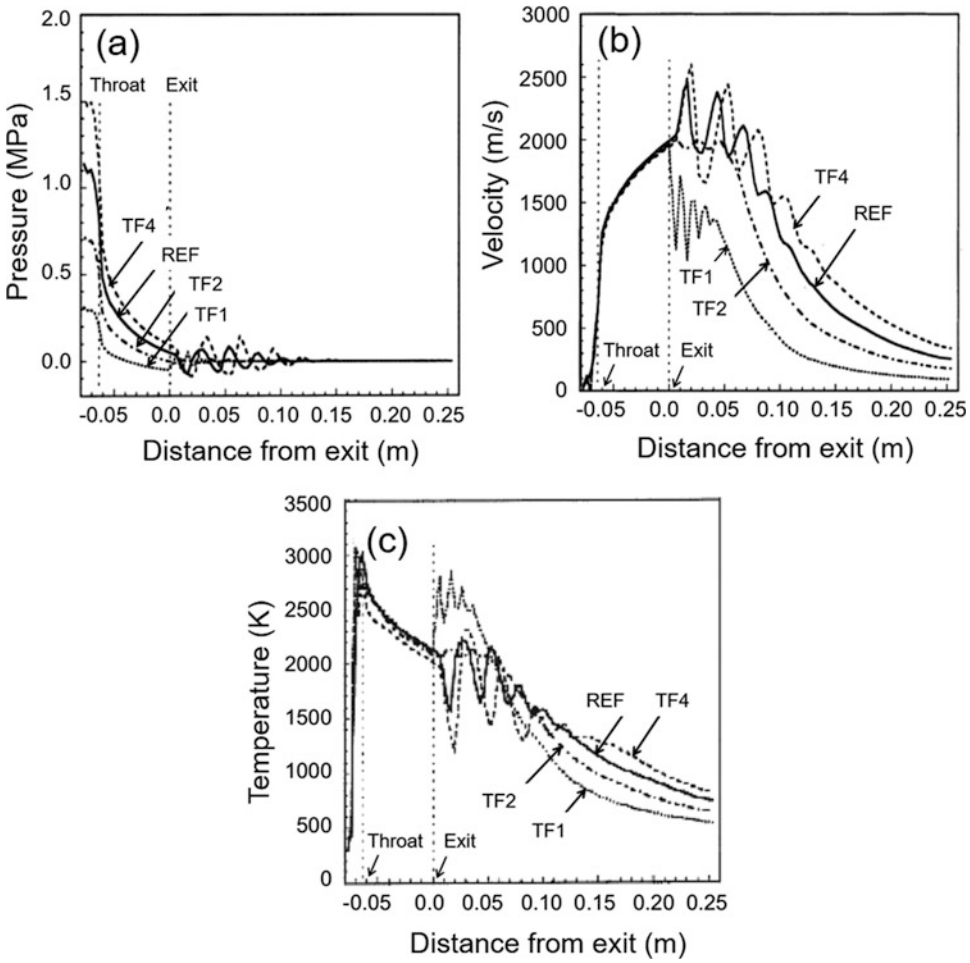

Fig. 7.33 Effect of total gas flow rate on the (**a**), pressure (**b**) velocity and (**c**) temperature, along the centerline (propylene-oxygen mixture, Sulzer-Metco Diamond Jet gun) REF and TF4 are under-expanded jets, while TF1 and TF2 are over-expanded [Cheng et al. (2001)]. (Reprinted with kind permission from Springer Science Business Media)

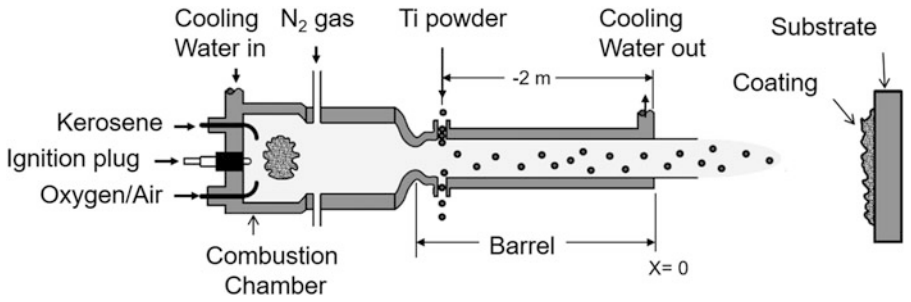

Fig. 7.34 Schematic of the WS-HVAF torch used for the numerical simulation [Kuroda et al. (2011)]

simulation for the calculation of the flow and temperature fields, particle velocity and temperatures in a WS-HVAF gun, and a standard HVAF gun for comparison. A schematic of the WS-HVAF gun used for the numerical simulation is given in Fig. 7.34. Four cases were considered for the operating conditions, given in Fig. 7.35a &b, of the WS-HVAF and the standard HVAF guns, respectively.

In the four cases considered, the fuel (kerosene) feed rate in the WS-HVAF gun varied linearly from 0.35 L/min in case 1 to 0.25 in case 4, with the mixing ratio of kerosene to oxygen set at the stoichiometric value for complete combustion. For the HVAF torch, the fuel feed rate was increased steadily from 0.17 L/min for case 1 to 0.22 L/min for case 4. The feed rate of nitrogen injected into the mixing chamber

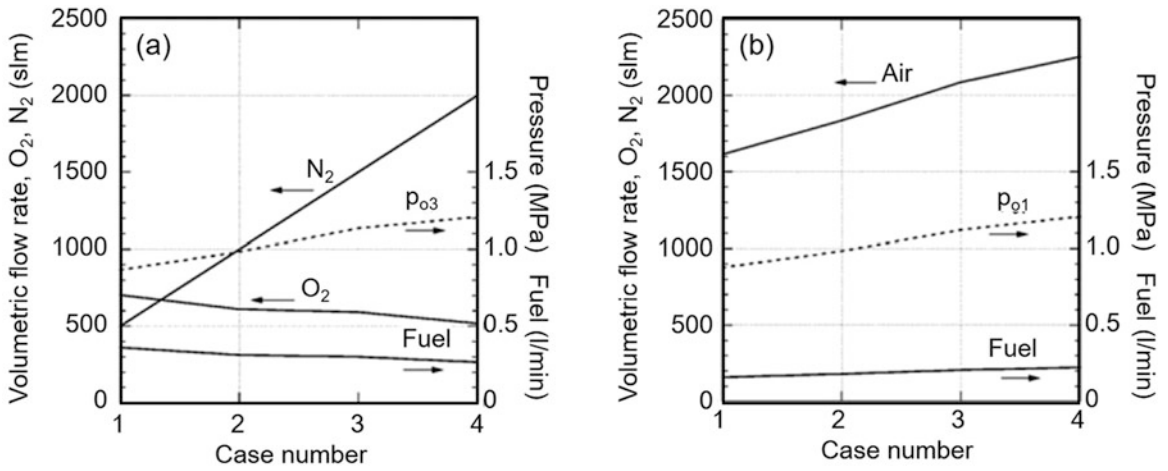

Fig. 7.35 Operating conditions of (**a**) WS-HVAF and (**b**) standard HVAF used for numerical simulation [Kuroda et al. (2011)]

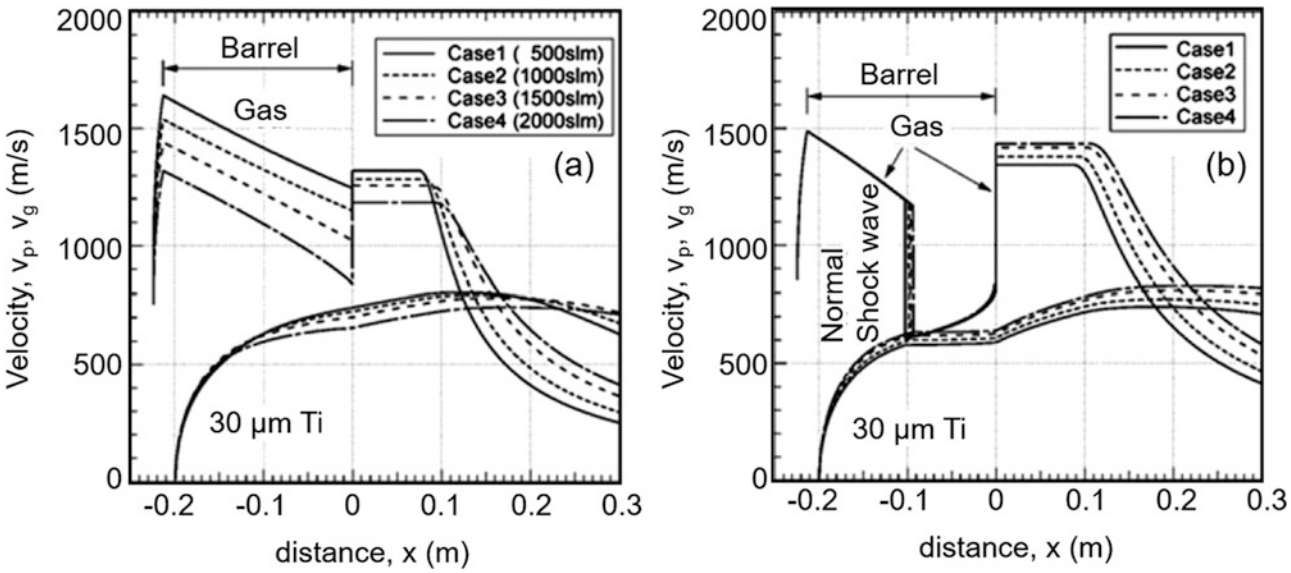

Fig. 7.36 Gas/particle velocities along the centerline (**a**) WS-HVAF gun and (**b**) standard HVAF gun based on numerical simulation [Kuroda et al. (2011)]

of the WS-HVAF torch was increased linearly from 500 slm (N_2) for case 1 up to 2000 slm (N_2) for case 4, with the pressure in the mixing chamber, p_{03}, varying from 0.88 to 1.2 MPa for case 1 and case 4, respectively. For the HVAF gun, the corresponding pressure in the combustion chamber, p_{01}, followed essentially the same curve as a result of the linear increase of the fuel and combustion air feed rate. Under these conditions, the temperature in the mixing chamber of the WS-HVAF gun was evaluated by chemical equilibrium calculations to be 2740 K for case 1 and 1780 K for case 4. The corresponding value for the combustion chamber of the HVAF gun was 2250 K for cases 1–4.

After obtaining the stagnant gas conditions just upstream of the convergent-divergent (C-D) nozzle for both the WS-HVAF and HVAF guns, a quasi 1-D gas dynamics model [Katanoda et al. (2006)] was used for the region inside the spray gun, which starts from the entrance of the C-D nozzle to the exit of the barrel. Outside the barrel, semi-empirical equations [Kleinstein et al. (1964)] were used to calculate the gas velocity and temperature of the gas jet along the centerline. The model calculations were complemented by an experimental determination of the total power generated by the combustion in the WS-HVAF gun to be around 200 kW with heat losses to the guns cooling water varying between 80 and 110 kW. Modeling results reported by Kuroda et al. (2011) are given, respectively, in Fig. 7.36 and Fig. 7.37 for the velocity and temperature of the gas and particles along the centerline of the WS-HVAF and the standard HVAF gun. Distance x = 0 corresponds to the barrel exit of the nozzle. The powder feed ports are situated about

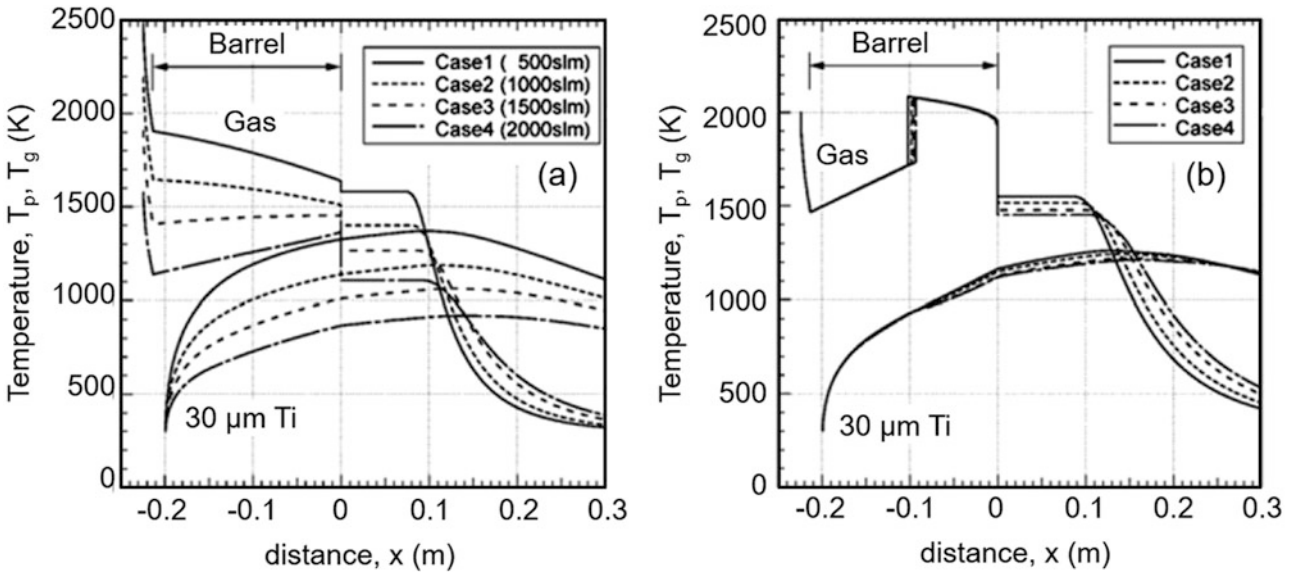

Fig. 7.37 Gas/particle temperatures along the centerline (**a**) WS-HVAF gun and (**b**) standard HVAF gun based on numerical simulation [Kuroda et al. (2011)]

−0.2 m upstream. It may be noted in Fig. 7.36a that as the gas expands through the C-D nozzle, its velocity increases rapidly to about 1300–1600 m/s depending on the nitrogen flow rate, corresponding to a Mach = 2, and then decreases gradually along the barrel length due to friction with the inner wall of the barrel. Outside the barrel, the gas velocity increases stepwise, which represents the under-expansion of the jet flow at the barrel exit, and it remains constant in the potential core of the jet outside the barrel, followed by a gradual decreases of the velocity due to mixing with the ambient air. In the case of the standard HVAF gun, Fig. 7.36b, the gas velocity at the inlet of the barrel is 1500 m/s (Mach = 2.0), which is almost the same as that for Case 2, of the WS gun. However, the gas decreases more rapidly after entering the barrel as compared to the WS gun, due to a larger decelerating effect by the pipe friction against the acceleration effect of cooling. The gas flow cannot maintain a supersonic flow until the end of the barrel, causing a normal shock wave in the barrel at around x = −0.1 m for all the four cases. In the lower part of both Figs. 7.36 *a&b,* the velocity of 30 μm diameter Ti particles is given along the centerline of the WS and standard HVAF gun. These show relatively little dependence on the flow rate of the injected nitrogen gas (cases 1–4) with an exit velocity from the gun barrel of about 600–700 m/s.

Figure 7.37a shows the significant effect of mixing with the cold nitrogen gas on the temperature of the gas and particles. After exiting the barrel, the gas temperature remains constant in the potential core region of the jet, and finally decreases again due to mixing with the ambient air. It is also noted that the injection of nitrogen gas has a significant impact on the in-flight maximum particle temperature in the gun barrel, which drops from 1400 K to less than 1000 K with increase of the gas flow rates from 200 to 2000 slm (N_2). The effect translates in a drop of the particle temperature at the substrate position, x = 0.2 m, for the WS-HVAF process, from 1250 to 900 K while keeping its velocity relatively unchanged. The corresponding temperature profile for the standard HVAF gun given in *Fig. 7 37b* shows relatively higher temperatures of the gases in the barrel region, about 2000 K, with the particle temperatures impacting on the substrate placed at x = 0.2 m, around 1200 K.

7.3.2 Powder Spraying Using HVOF/HVAF

7.3.2.1 Particle Temperatures and Velocities

As has been well recognized, the quality of a coating depends directly, though not exclusively, on the particle velocity and temperature distributions prior to their impact on the substrate. It is, therefore, not surprising that much attention has been given to the calculation and control of the in-flight particle temperature and velocities within such hot flows. This is achieved using the conventional equations considering the drag force exerted on the particle [Tawfik and Zimmerman (1997), Oberkampf and Talpallikar (1996a), Oberkampf and Talpallikar (1996b), Gu et al. (2001), Sakaki and Shimizu (2001), Yuan et al. (2006), Gu et al. (2001), Yang et al. (2002), Srivatsan and Dolatabadi (2006), Cheng et al. (2001)1, Gu et al. (2004), Hanson et al. (2002), He et al. (2001)] (see also for details Chaps. 4 and 5). The drag coefficient is corrected for the particle morphology [Cheng et al. (2001b)] or, what is particularly important, for gas compressibility effects at supersonic velocities [Gu et al.

(2004)]. Such calculations show, as for other spray processes, the strong dependence of the particle temperatures and velocities at impact on their size and trajectories in the flow.

For example, in flow conditions similar to those presented in Figs. 7.32 and 7.33 [Cheng et al. (2001b)], the temperature evolution along the axial trajectory of WC-18Co particles (82 wt.% WC+ 18 wt.% Co) with six different diameters is presented in Fig. 7.38 [Cheng et al. (2001a)].

As can be seen in Fig. 7.38, the 2 and 5 μm particles follow closely the gas temperature. These small particles reach gas temperature before entering the divergent portion inside the gun, and continuously cool down with the decrease in gas temperature. As cold ambient air is entrained, it rapidly cools the gas jet, and the particle temperature drops as well. Beyond a distance of 0.24 m from the nozzle exit, the temperature of 2 μm particles equals the gas temperature. Particles with diameters of 10 and 20 μm reach the gas temperature inside the convergent portion of the nozzle, and after exiting the gun nozzle, their temperatures decrease monotonically. The temperatures for particles larger than 20 μm remain relatively unchanged after exiting the nozzle due to their high thermal inertia. The oblique shocks at the nozzle exit perturb strongly the temperature of particles smaller than 20 μm.

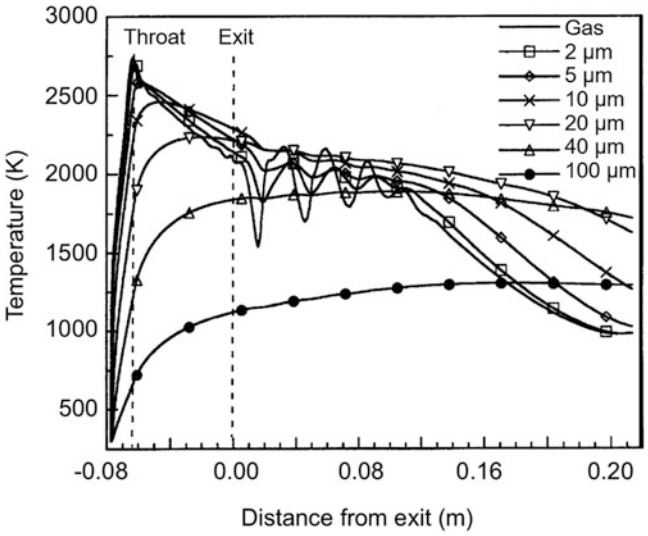

Fig. 7.38 Predicted temperatures of spherical WC-Co (82 wt.% WC) particles with different diameters as a function of distance from the gun exit for axial flow. Gas flow rates: propylene = 6.2×10^{-5} mol/s; oxygen = 20.3×10^{-5} mol/s; nitrogen = 0.99×10^{-5} mol/s, and cooling air = 30×10^{-5} mol/s [Cheng et al. (2001a)]. (Reprinted with kind permission from Springer Science Business Media)

Similar results were obtained by Srivatsan and Dolatabadi (2006), who studied the influence of the oblique shock at the nozzle exit and the bow shock in front of the substrate on MCrAlY particles, 15 and 30 μm in diameter. It was found that 15 μm particles, being very light, are largely affected by the shock diamonds at the nozzle exit and bow shock near the substrate, whereas 30 μm particles are least affected by either shock diamonds or bow shocks. This is due to the larger Stokes numbers associated with 30 μm particles, which is the ratio of particle response time to a time characteristic of the fluid motion. They have also studied the choice of substrate configuration. A convex substrate is better when compared with flat and concave configurations. Although the shape of the concave substrate is favorable for capturing all the particles, the strength of the bow shock formed on a concave surface is very high, which leads to dispersion of most of the lighter particles.

The impact temperatures and velocities of particles thus depend strongly on their sizes, as illustrated in Fig. 7.39a and b from [Cheng et al. (2001a)], and on the distance between

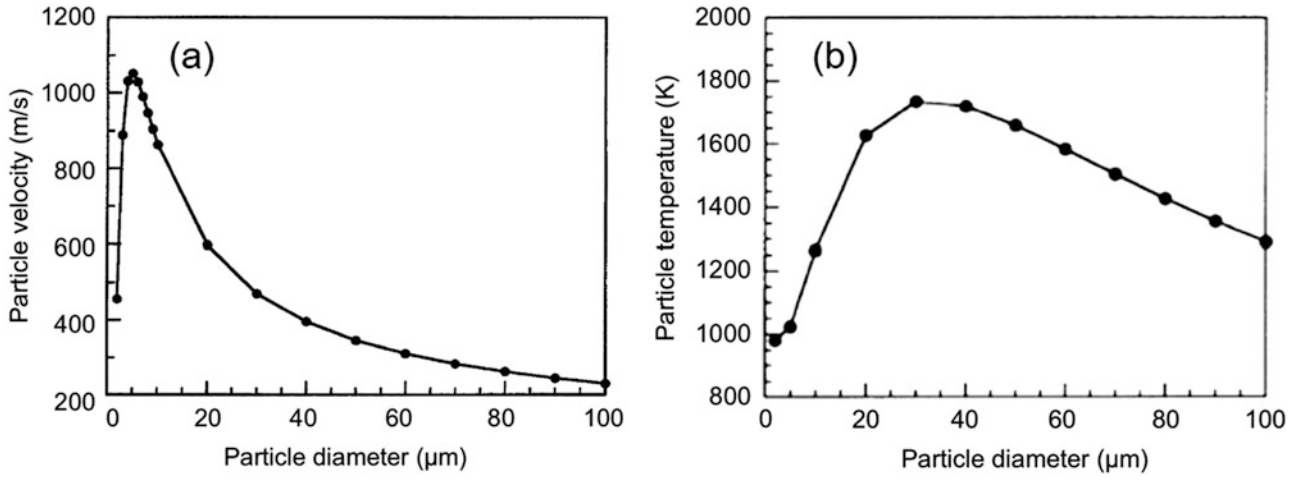

Fig. 7.39 Predicted effect of particle size on its (**a**) velocity and (**b**) temperature, at a spray distance of 0.254 m. Gas flow rates: propylene, 6.2×10^{-5} mol/s; oxygen, 20.3×10^{-5} mol/s; nitrogen, 0.99×10^{-5} mol/s; and cooling air 30×10^{-5} mol/s [Cheng et al. (2001a)]. (Reprinted with kind permission from Springer Science Business Media)

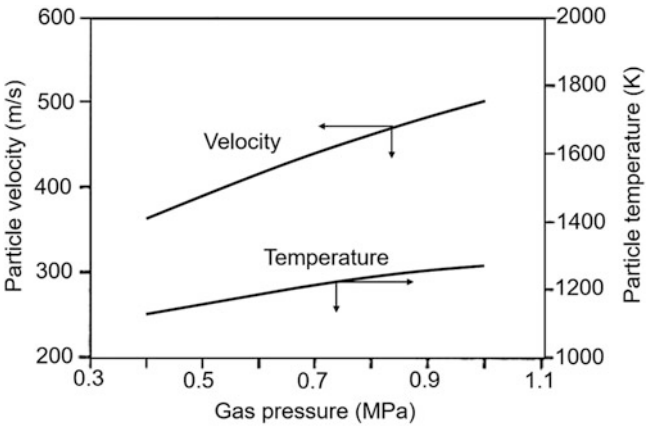

Fig. 7.40 Calculated velocity and temperature of a 38 μm stainless steel particles at the exit of the conical nozzle as function of chamber pressures. Modified TAFA JP-5000 system HVOF gun using kerosene/oxygen [Hanson et al. (2002)]. (Reprinted with kind permission from Springer Science Business Media, copyright © ASM International)

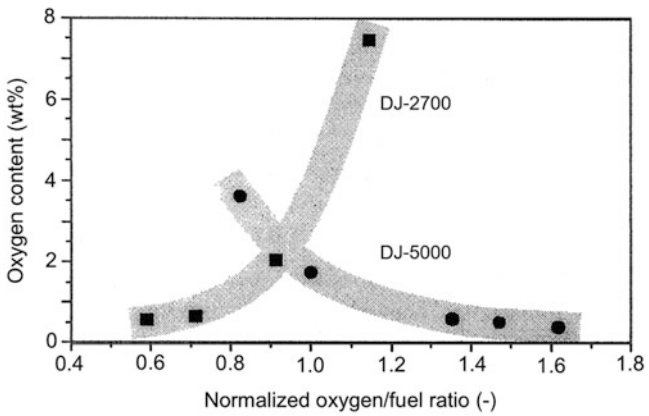

Fig. 7.41 Variation of the oxidation level of stainless steel 316 L particles with the oxygen/fuel ratio of combustible gases for the DJ-2700 and DJ-5000 HVOF gun [Dobler et al. (2000)]. (Reprinted with kind permission from Springer Science Business Media, copyright © ASM International)

nozzle exit and the substrate. These show that the most critical parameter to be concerned about for HVOF spraying is the particle velocity. As seen in Fig. 7.39a, for particles with a diameter between 10 and 60 μm, typically used in thermal spraying applications, particle velocities are in the range between 310 and 860 m/s at a spray distance of 0.254 m. This difference in velocities is equivalent to an order of magnitude difference in the kinetic energy per unit mass of the impinging particle. This will lead to different deformation conditions as splats are being formed, and the higher the velocity, the better is the coating quality. As shown in Fig. 7.39b, the effect of size distribution is less important on particle temperatures.

Calculations by Li et al. (2004b) have also shown that for a given spray gun (type of Fig. 7.15c) and a combustible gas mixture, the velocity of stainless-steel particles (28 μm in mean diameter) is almost independent of the position of the axial injector and varies almost linearly with the chamber pressure, as shown in Fig. 7.40. The observed temperature variations are significantly less than velocity. However, it was reported that particle temperature is very sensitive to the radial injector position, which has been varied from upstream of the nozzle throat to different positions downstream of it. The particle injection location was found to determine the residence time of particles within the nozzle, thus providing a means to control particle temperature. On the other hand, the injection location had a negligible effect on particle velocity according to the numerical model predictions. Experiments revealed that for 38 μm stainless steel particles, their impact velocity and temperature could be controlled within the ranges 340 to 660 m/s and 1630 and 2160 K, respectively.

7.3.2.2 Particle Oxidation

Oxidation is a key parameter for a process that is mainly devoted to the spraying of metals and metal-matrix composites. Moreover, composite particles often contain fine carbide particles, which are very sensitive to oxidation. Carbides also tend to dissolve into the metal matrix if the particle temperature is too high.

Oxidation is present inside the gun and in the flame core due to the excess oxygen (lean flame). However, the particle temperature plays a key role in the oxidation process, especially if it is above the melting temperature: the oxygen content within a steel coating varies from 0.25 wt. % for particle temperatures below 1700 K to 0.8 wt.% for particles at 1800 K! Particle oxidation does not vary in a systematic fashion with the oxygen/fuel ratio of the combustible gases [Dobler et al. (2000)] (Fig. 7.41). With the DJ-2700 gun with axial injection of particles (particle temperatures higher than when injected radially into a JP-5000 gun), the excess of oxygen increases the oxygen content of the coating (316 L). In contrast, with the JP-5000, where the particle temperature is almost 800 K lower, the excess of oxygen cools the particles, and the effect is reverse, that is, the more the oxygen in the flame, the less the oxide in the coating.

Oxidation, as shown by Dobler et al. (2000), occurs only slightly in the jet core but more in the mixing region with the surrounding air (see Fig. 7.42 [Hackett et al. (1995)]) and within the coating during its formation. To reduce oxidation, a shroud gas can be used [Hackett et al. (1995)]. However, shroud gas flow rates (nitrogen) must be very high. For an O_2 flow rate of 727 slm and kerosene flow rate of 0.42 L/min (gun type of Fig. 7.15c), the nitrogen flow rate reaches 0.45 kg/s (about 21.6 m^3/s!) to reduce the oxygen content of pure iron from 3 wt. % to 1 wt.%, as shown in Fig. 7.43 [Hackett et al. (1995)].

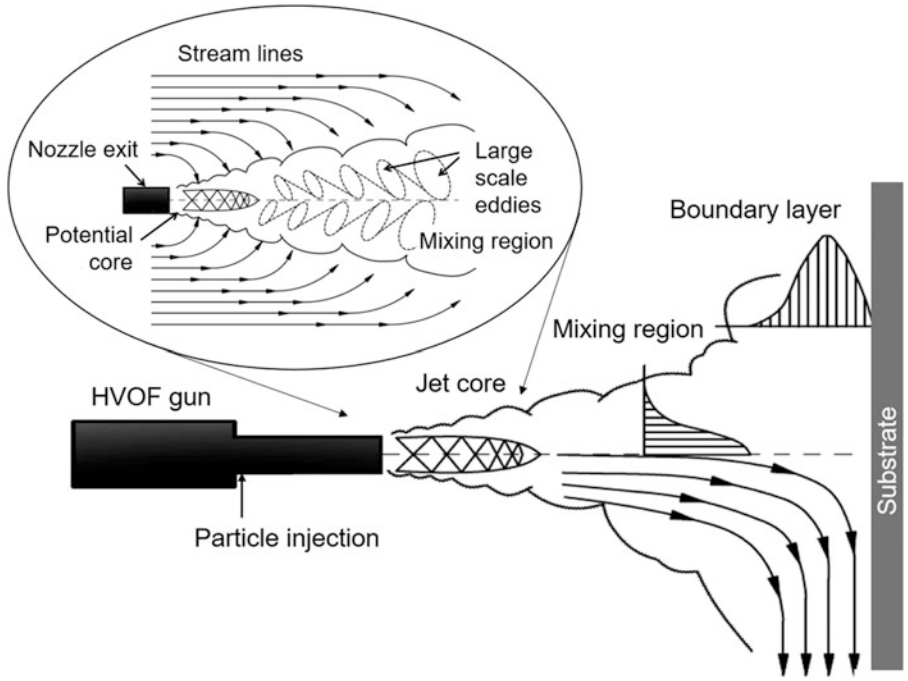

Fig. 7.42 Schematic drawing of HVOF jet mixing with the surrounding gas (**a**) details of the flow (**b**) different regions of the spray process [Hackett et al. (1995)]. (Reprinted with kind permission from ASM International)

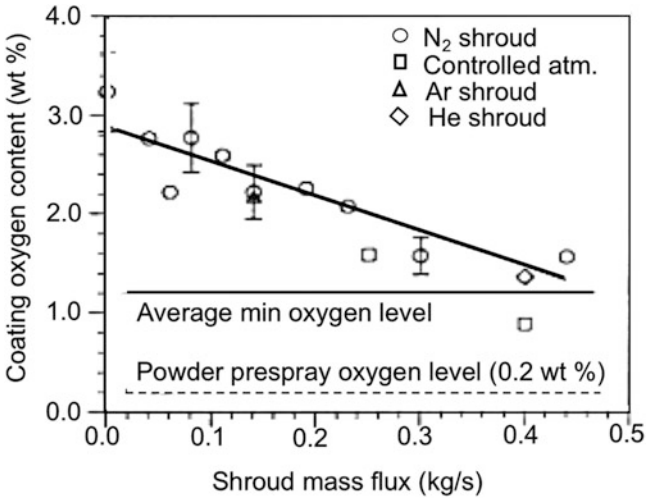

Fig. 7.43 Evolution of the coating oxygen content with the mass flow rate of shroud gas for different shroud gases [Hackett et al. (1995)]. (Reprinted with kind permission from ASM International)

The gas shroud set-up has two important effects: mean particle (WC-Co) velocities increase (with a reducing flame at a pressure of 0.72 MPa) from 760 m/s to 850 m/s with the shroud, while their mean temperatures drop from 1950 °C to 1830 °C. Accordingly, the density of the sprayed coating was improved, the degree of decomposition of WC dropped from 6% to 2.5%, and coatings were superior both in corrosion and wear resistance compared to those obtained with no shroud.

As discussed earlier in sect. 7.3.1.3, a number of HVOF/HVAF gun design modifications were made, leading to the development of the so-called gas shroud (GS-HVOF), the warm spray (WS-HVAF), and the low-temperature (LT-HVAF) guns, which offer distinct advantages in terms of reduction of in-flight particle temperature, without compromising, or at times with an increase of the corresponding particle velocity, which plays a key role in reducing particle oxidation and ceramic degradation in the spray coating process.

7.3.2.3 Coating Formation

[Trompetter et al. (2006)] made an interesting study of splat formation. They used an HVAF gun with a gas temperature of about 1300 °C, below the melting point of NiCr powder (T_m = 1400 °C). The particle velocity was about 670 m/s. When sprayed on soft substrates (compared to the NiCr hardness), predominantly solid splats with deep penetration were observed, while on hard substrates that resisted to particle penetration, a higher percentage of molten splats were observed. They attributed this behavior to increased conversion of particle kinetic energy into heat with increased particle plastic deformation with harder substrates.

The second effect of the high-velocity impacts is a peening action that results in compressive residual stresses in coatings. The first work on this topic was that of Kuroda et al. (2001). They found that the intensity of the peening action and the resultant compressive stress by HVOF-sprayed particles increase with the kinetic energy of the sprayed particles.

Measurements revealed that the residual stress at the surface of the HVOF coatings is low, often in tension, but the stress inside the coatings is at a high compression level. This low value at the surface reflects the lack of peening effect of the last deposited layer. Normally, the quenching stress due to fast cooling of the splat is always tensile, and only the peening effect can transform this tensile stress into a compressive one.

The link between the compressive peening stresses induced in the deposited coating layers and the impact velocity of the sprayed particles have also been confirmed by other researchers [Totemeier et al. (2002); Totemeier et al. (2004); Lima et al. (2006); Yilbas and Arif (2007)]. Residual stresses of +531 MPa were reported by Yilbas and Arif (2007) for the spraying of diamalloy alloy (Inconel 625) onTi-6Al-4V. Comparable values were reported by Lima et al. (2006) for the spraying of superalloy bond coats such as Amdry 9951, Sulzer Metco or Amdry 997, Sulzer Metco on UNS G41350 steel. Such values, strongly linked to the impact velocity, vary from about 100 MPa at 500 m/s to 400 MPa at 650 m/s for 316 L coatings [Totemeier et al. (2004)]. Of course, the substrate is also affected by this peening effect, which, for example for a stainless-steel substrate, affects a region of approximately 100 μm deep, producing an increased subsurface hardening. When these coatings are submitted to high temperature conditions, a recrystallization process takes place and the hardness decreases, as well as the residual compressive stress.

Diamond-Cu composites have been considered to be the next generation of electronic packing materials. One of the key stumbles for such an application is the joining problem between diamond-Cu composites and other materials due to the poor wettability of the diamond particles in the composites. In order to overcome this hurdle, [Liu et al. (2016)] thermally sprayed pure Cu powder onto diamond-Cu substrate by low-temperature high-velocity oxygen fuel spraying process. The spraying was conducted by the LT-HVOF process. As the critical diameter of the combustion chamber was reduced from 7.8 to 5.0 mm, the pressure of the combustion chamber was increased obviously from 0.85 to 1.55 MPa. The flame of the modified process was faster and more intensive than the conventional HVOF spraying process. As a result, the heating time of particles was shortened correspondingly. In order to obtain coatings with low oxygen content and porosity, the spraying parameters such as the flow rate of oxygen and kerosene, the powder feeding rate, and the critical diameter of combustion chamber were optimized. The microstructure and some fundamental properties of the coating obtained were systematically investigated, and morphologies of the single splat deposited on the diamond-Cu substrate were also observed. The splats obtained had good adhesion with the substrate as fine particles flattened sufficiently, while the coarse particles were significantly deformed. The coating was quite dense, with porosity lower than 1%, oxygen content under 0.5%, and thermal conductivity about 266 W/m.K, and still remained on the diamond-Cu substrate after 50 thermal shock cycles between 300 °C and water bath at room temperature. Meanwhile, the solderability of the coating was significantly improved. Therefore, the Cu coating deposited on the diamond-Cu substrate by the low-temperature high-velocity oxygen fuel spraying process can be beneficial in the electronic industry, assisting with soldering and improving the wettability for joining of other materials.

Finally, the HVOF process provides high-density coatings (less than 3% porosity) due to the high impact energy of particles (between 400 and 650 m/s) [Sidhu et al. (2005)]. The short residence times of particles with rather low temperatures (by increasing the gas flow rate) allow for the deposition of particles slightly below the melting temperature, thus reducing the oxidation and decomposition of materials such as WC. The particles have better bonding due to the high impact velocity and low degradation of the sprayed materials. Thus, such coatings have better wear resistance and higher hardness than those sprayed by flames or plasmas, and now, with the "*third generation*" of spray guns, sufficiently low porosity is obtained that these coatings can be used for corrosion protection. Coatings have mostly compressive residual stress, while those sprayed by flames or plasma are often tensile.

Figure 7.44 shows the evolution of the HVOF/HVAF gun designs over the last few years tending toward a reduction of particle temperature in favor of an increase of particle velocity. HVOF spray systems of the "*third generation*" (DJ-2700, DJ-2800, JP-5000) using chamber pressures of up to 1 MPa accelerate spray particles to velocities of about 650 m/s. For HVAF guns, pressures can reach 2 MPa. Coating microstructures demonstrate that only small particles or fractions of larger ones are molten before the impact onto the substrate. A further reduction in particle temperatures below the melting temperatures of metals requires a substantial increase in velocity, which can only be realized by optimizing the expansion ratio in the diverging nozzle section and by using higher chamber pressures through the injection of non-combustible gases. The last developments correspond to power levels up to 300 kW (kerosene 31 L/h, O_2 965 slm, air 500 slm), with the flame being ignited in the combustion chamber with a hydrogen pilot flame (88 slm).

To check the influence of the gun design on coating quality, a series of experiments [Schwetzke and H. Kreye (1999)] were performed with the same powder, an agglomerated and sintered WC-Co 83–17 with a particle size range of −45 + 10 μm. The powder was sprayed with the HVOF systems Jet Kote (Stellite Coatings, Goshen, IN), Top Gun (UTP Schweißmaterial, Bad Krozingen, Germany), Diamond Jet (DJ) Standard, DJ -600, DJ-2700 (Sulzer Metco, Westbury, NY), JP-5000 (Tafa, Concord, NH), and Top Gun-K (GTV, Luckenbach, Germany). The degree of phase transformations depends on the heat

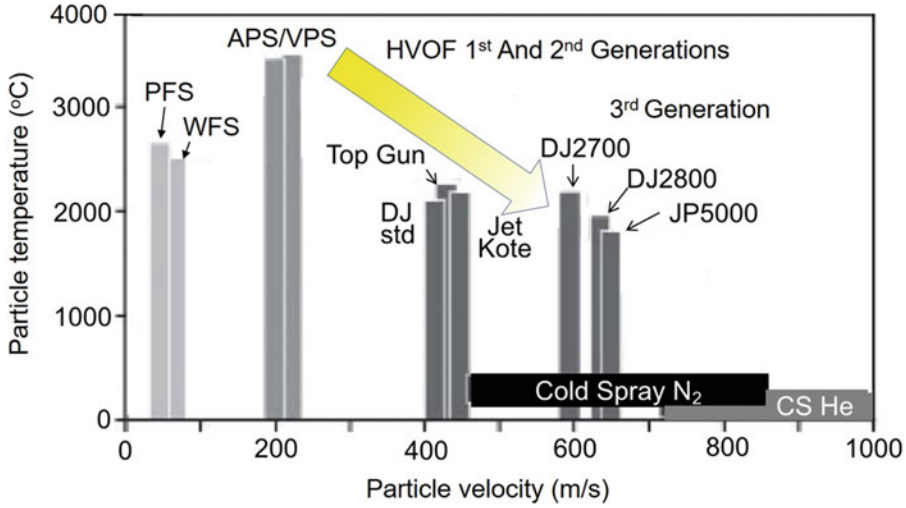

Fig. 7.44 Particle temperatures and velocities obtained in different thermal spray processes, as measured for high-density materials. (PFS) Powder Flame Spraying, (WFS) Wire Flame Spraying, (APS) Air Plasma Spraying, (VPS): Vacuum Plasma Spraying, (CS) Cold Spray) [Gärtner et al. (2006)]. (Reprinted with kind permission from Springer Science Business Media], copyright © ASM Int.)

transferred to the particles, which depends in turn on the spray system and fuel used, the flame temperature, and the type of spray powder [Schwetzke and H. Kreye (1999)]. Phase transformations increase when the injection of the powder occurs in a region where the flame temperature is highest, such as in the top gun system, where the powder is injected directly into the combustion chamber. Fewer phase transformations occur when the powder is injected behind the combustion chamber in a region where the flame temperature is low, as in the JP-5000 and Top Gun-K system, or when the flame temperature is lowered by cooling air, as in the DJ-2600 and-2700 systems [Hackett et al. (1995)]. The use of dense spray powders, which are heated up less in the spray process, or powders that already contain some amounts of h-phase, reduces phase transformations. Decarburization of an agglomerated and sintered WC-Co (83-17 wt %) powder ranges from 25 to 70% for the various spray systems and fuels. However, the properties of the coatings such as hardness and wear resistance are not influenced when the carbon loss remains below 60%. Hardness and bond strength of the coatings are mainly determined by the impact velocity of the particles, which are highest when systems with a converging-diverging Laval nozzle are used, due to the superior particle velocities.

Wielage et al. (2006) point out that new HVOF spraying guns operating at increased combustion chamber pressures have shown high potential for spraying of coatings consisting of metals that do not feature the outstanding ductility of pure copper or aluminum. High deposition efficiency, that is, up to 85%, at a considerable powder feed rate of 4.5 kg/h is already possible for spraying corrosion-protective iron or nickel-based coatings like AISI 446, AISI 316 L, or MCrAlYs. Also spraying of highly reactive materials like titanium under atmospheric conditions becomes feasible. Both dense coatings for corrosion-protection purposes and porous coatings for biomedical applications can be produced. [Wielage et al. (2006)].

According to Tillmann et al. (2018), current developments in different industrial sectors also showed an increasing demand of thermally sprayed internal diameter (ID) coatings. The most recent research and development was mainly focused on commercial applications such as arc spraying (AS), atmospheric plasma spraying (APS), and plasma transferred wire arc spraying, especially for cylinder liner surfaces. However, efficient HVOF torches are meanwhile available for ID applications as well, but in this field, there is still a lack of scientific research. Especially, the compact design of HVOF-ID and APS-ID spray guns, the need for finer powders, and the internal spray situation led to new process effects and challenges, which had to be understood in order to achieve high-quality coating properties comparable to outer diameter coatings. Thus, in the present work, the focus was on the ID spraying of bond coats (BC) and thermal barrier coatings (TBC) for high-temperature applications. An HVOF-ID gun with a N_2 injection was used to spray dense bond-coat (MCrAlY) coatings. The TBCs (YSZ) were sprayed by utilizing an APS-ID torch. Initially, flat steel samples were used as substrates. The morphology and properties of the sprayed ID coating systems were investigated with respect to the combination of different HVOF and APS spray parameter sets. The results of the conducted experiments show that the HVOF-ID spray process with N_2 injection allowed to adjust the particle temperatures and speeds within a wide range. CoNiCrAlY bond coats with porosity from 3.09 to 3.92% were produced. The spray distance was set to 53 mm, which led to the smallest coat-able ID of 133 mm, see *Fig. 5.44*. The porosity of the TBC ranged from 7.2 to 7.3%. The spray distance for the APS-ID process was set to 70 mm, which leads to the smallest coat-able ID of 118 mm.

7.3.3 Wire Spraying Using HVOF /HVAF

One of the drawbacks of wire flame spraying is the relatively low velocity of particles at impact, resulting in very porous coatings (over 10%), which are only tolerated because of the high deposition rates of the process (up to 10 kg/h), a key factor in process economics. HVOF wire spraying has been intensively studied for the automotive industry. A schematic of a typical wire HVOF torch (Metco DJRW Diamond Jet gun) is given in Fig. 7.45.

The nozzle exit diameter is 8.7 mm and a typical wire diameter is 3.2 mm. The gas flow rates are 47 slm propylene, 212 slm oxygen, and 519 slm atomizing air. With a steel wire, these conditions resulted in a droplet size distribution between 10 and 80 μm with velocities around 250 m/s. According to Neiser et al. (1995), Lopez et al. (1998), Neiser et al. (1998), stainless steel droplet velocities were measured to be 540 m/s for 10 μm and 395 m/s for 20 μm, while their temperature was close to 2200 K.

[Neiser et al. (1995), Neiser et al. (1998), Lopez et al. (1998)] have shown that the high gas velocity induces a convection phenomenon within liquid droplets removing continuously fresh metal at their surface and moving the oxygen or the oxides formed at the droplet surfaces to the inside. The formation of such as internal circulation pattern inside the droplets gives rise to coatings where FeO is detected in the resulting splats. The phenomenon is limited to the region in the close vicinity of the exit nozzle of the torch. Further downstream in the jet particle/droplet oxidation is limited to its surface. To spray steel inside aluminum-silicon cylinder bores for the automotive industry, a curved air cap has been adapted to the Metco rotating torch (DJRW Diamond jet) (Fig. 7.46). Calculations and measurements reported by Hassan et al. (1998) and Lopez et al. (1998) with the axial position of the wire give particle velocities at impact between 200 and 250 m/s.

Molybdenum has also been sprayed by wire flame and D.C. plasma jets [Modi and Calla (2001)]. Coatings obtained with Mo + 25 wt % NiCrBSi were compared to those sprayed by HVOF. The latter had a lower friction resistance than the plasma-sprayed coatings. They were also harder and more wear resistant than wire flame-sprayed coatings. Corrosion protection coatings of Ni-Cr wires [Sidhu et al. (2006)1] and NiCrBSi, Cr_3C_2-NiCr and Stellite-6 [Sidhu et al. (2006)2] sprayed with HVOF wire fuel-oxygen gun had porosities of less than 1%, and a good resistance to hot corrosion, especially the Ni-20Cr coatings.

It is interesting to note that the "*hybrid spray process*" has been developed by Stanisic et al. (2006) through a combination of arc spraying with HVOF/plasma jet gun. In this system, schematically illustrated in Fig. 7.47, the material to be sprayed is introduced either via arcing of wires only or a full-hybrid mode with both arcing of wires and a powder or wire through the HVOF gun. It was also possible to operate in a pure HVOF mode with either wire or powder fed to the HVOF gun. According to the authors, this system provides very dense coatings compared to arc-sprayed ones [Stanisic et al. (2006)].

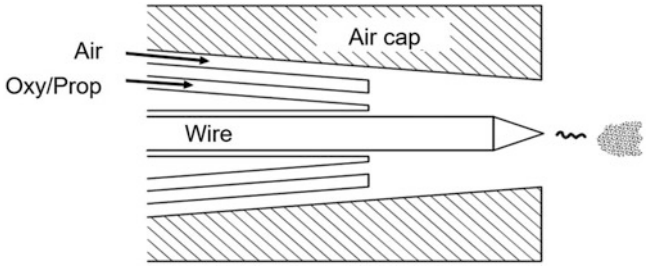

Fig. 7.45 Schematic diagram of the HVOF torch and the wire melting and atomization process [Neiser et al. (1995)]. (Reprinted with kind permission from ASM International)

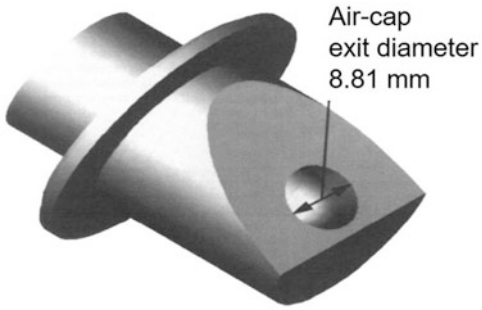

Fig. 7.46 Curved air cap adapted to the HVOF wire gun schemed in Fig. 5.37 [Hassan et al. (1998)]. (Reprinted with kind permission from Springer Science Business Media, copyright © ASM International)

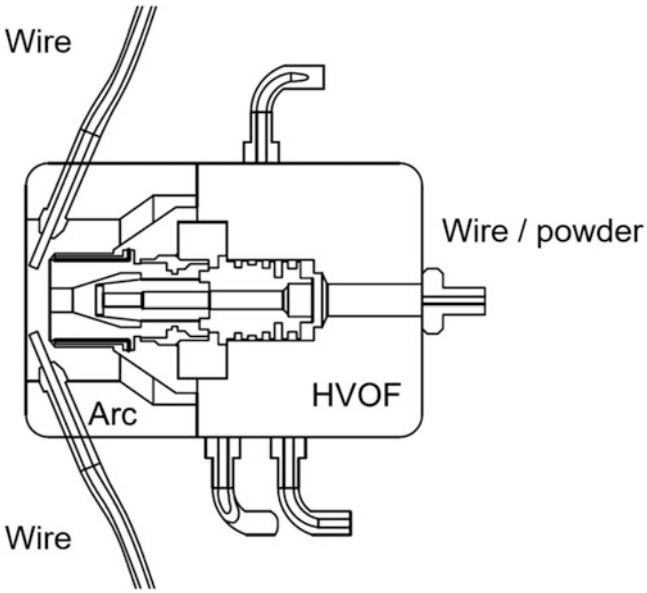

Fig. 7.47 Hybrid spray torch comprising wire arc and HVOF gun. [Stanisic et al. (2006)]. (Reprinted with kind permission from Springer Science Business Media, copyright © ASM International)

7.3.4 High-Velocity Suspension Flame Spraying (HV-SFS)

According to Killinger et al. (2006), the use of thermal spray technologies for the deposition of nanostructured coatings is a challenging approach with new promising applications. It requires the processing of very fine-grained powders with grain size in the nanoscale. As nano- and sub-micrometer powders cannot be handled using mechanical powder feeders, new concepts have to be developed. Among these, suspension spraying is one of the most promising. Standard HVOF techniques are not easily adapted to the injection either of nanoparticles in a liquid carrier (suspension) or in a solution that upon heating transforms in solid particles that can be very small. High-velocity suspension flame spraying (HV-SPS) is a new approach to spray micron, submicron, or nanoparticles with hypersonic speed to form thin and dense coatings. The process is based on the dispersion of the powder in an aqueous or organic solvent which is fed axially into the combustion chamber of a modified high-velocity oxyfuel (HVOF) spray torch. Several suspension feeder concepts were tested to ensure a constant flow of the suspension and, thus, a stable spray process. The study was carried out using a suspension containing sub-micrometer or nano-sized powders of alumina, titania, and yttrium-stabilized zirconia (YSZ).

[Dongmo et al. (2009a)] and [Dongmo et al. (2009b)] point out that the HV-SPS system is characterized by a two-step combustion process. The premixed combustion of propane and oxygen is run with an excess of oxygen (lean-burn combustion), leading to excess oxygen after propane combustion. Using ethanol as dispersant for the nanostructured feed powder, the ethanol vapors liberated as the suspension droplets evaporate are burned in a diffusion flame reaction using the excess oxygen in the system. Experimental studies show a jet stream, or open jet formation, of the suspension (in this case, ethanol solution containing nanoparticles [Dongmo et al. (2009b)]) for injection in a TopGun-G® combustion chamber at high pressure (0.3–0.4 MPa) with an injection nozzle with an internal diameter < 1 mm . The mechanism of droplet formation in the form of a dense cloud of droplets containing nanoparticles with uniform diameter at the nozzle outlet followed by droplet breakup is illustrated in Fig. 7.48. Open jet formation means that the fluid is injected as a coherent stream into the surrounding medium (combustion chamber with high pressure), while, for example, for automotive injection systems, a spray injection is applied with a diverging jet of atomized fluid. In case of the HV-SPS injection, the suspension jet breaks up only downstream under the influence of fluid dynamic forces. By calculating the suspension jet's Weber number, it can be evaluated if breakup takes place under the injection conditions and which breakup model is appropriate for the modeling of breakup and droplet.

Bolelli et al. (2009) manufactured Al_2O_3 coatings using the high-velocity suspension flame spraying (HV-SPS) technique with a nanopowder suspension. Their structural and microstructural characteristics, micromechanical behavior, and tribological properties were studied and compared to conventional atmospheric plasma-sprayed and high-velocity oxygen-fuel-sprayed Al_2O_3 coatings manufactured using commercially available feedstock. The HV-SPS process enabled near-full melting of the nanopowder particles, resulting in very small and well-flattened lamellae (thickness range 100 nm to 1 μm), almost free of transverse microcracking, with very few unmelted inclusions. Thus, porosity was much lower, and pores were smaller than in conventional coatings. Moreover, few interlamellar or interlamellar cracks existed, resulting in reduced pore interconnectivity (evaluated by electrochemical impedance spectroscopy). Such strong interlamellar cohesion favored dry sliding wear resistance at room temperature and at 400 °C.

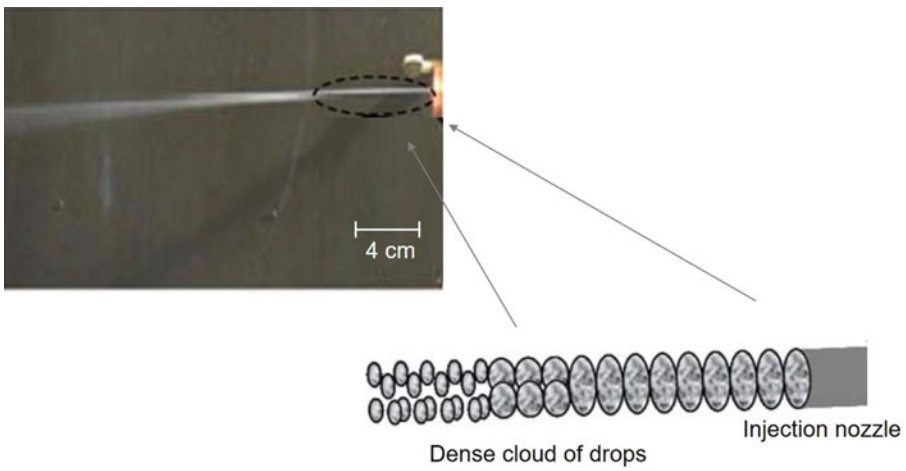

Fig. 7.48 Suspension droplets emerging from the injection nozzle and their subsequent breakup in the HVSFS jet stream [Dongmo et al. (2009b)]

[Altomare et al. (2011)] used the high-velocity suspension flame spraying technique (HV-SPS) to deposit 45S5 bioactive glass coatings onto titanium substrates, using a suspension of micron-sized glass powders dispersed in a water + iso-propanol mixture as feedstock. By modifying the process parameters, five coatings with different thicknesses and porosities were obtained. The coatings were entirely glassy but exhibited a through-thickness micro-structural gradient, as the deposition mechanisms of the glass droplets changed at every torch cycle because of the increase in the system temperature during spraying. After soaking in simulated body fluid, all of the coatings were soon covered by a layer of hydroxyapatite; furthermore, the coatings exhibited no cytotoxicity, and human osteosar-coma cells could adhere and proliferate well onto their surfaces. HV-SPS-deposited 45S5 bioglass coatings are therefore highly bioactive and have potentials as replacement of conventional hydroxyapatite in order to favor osseointegration of dental and prosthetic implants.

[Killinger et al. (2015)] point out that suspension spraying has evolved during the past decades and now is at the threshold of commercial utilization. Compared to standard powder spray methods, mainly DC plasma spraying and (high velocity) flame spraying, it is quite clear that suspension spraying will not replace these well-established technologies but can extend them by adding new coating properties. Still there remain many issues to be resolved. Suspension interaction with the hot gas stream is much more complex than in ordinary powder spray processes. In case of HVOF, when axial injection into the combustion chamber is used, a direct observation of the liquid flame interaction is not possible. This paper discusses the present status of suspension HVOF spraying (high-velocity suspension flame spraying) including torch concepts, torch configuration in case of a top gun system as well as different injector concepts and their influence on suspension atomization. The role of suspensions is discussed regarding their rheological and thermo-dynamical properties, mainly given by the solvent type and the solid content. An overview of different available diagnostic methods and systems, and the respective applicability is given. Coating properties are shown and discussed for several oxide ceramics with respect to their possible applications.

Müller et al. (2012) compared two different spray processes: suspension plasma spraying (SPS) and high-velocity suspension flame spraying (HV-SPS), which are under focus in the field of suspension spraying. Both techniques are suitable for manufacturing finely structured coatings. The differences in particle velocity and temperature of these two processes cause varying coating characteristics. The high particle velocity of the HV-SPS process leads to more dense coatings with low porosity values. Coatings with higher and also homogeneous porosity, which can be generated by SPS, also have high potential, for example, for thermal barrier coatings. In this study, both the processes, SPS and HV-SPS, were compared using alumina as feedstock material mixed with different solvents. Besides the characterization of the microstructure and phase composition of the applied coatings, the focus of this study was the investigation of the melting behavior of the particles in-flight and of single-splat characteristics.

Using the SPS process, high porosities up to 40% were achieved, with the applied solvent strongly influencing the melting behavior. Much better melting can be achieved by means of organic solvents of the additional energy that is delivered during their combustion. Further improvements concerning suspension injection will lead to better melting of the particles. Comparison of HV-SPS and SPS coatings revealed differences in phase composition. In SPS coatings, a high amount of alpha alumina was detected, whereas in HV-SPS coatings, the gamma phase was dominant.

The use of suspension plasma spraying (SPS) was also used by Oberste Berghaus et al (2008) for the manufacturing of thin and low-porosity electrolytes in an effort to develop a cost-effective and scalable fabrication technique for high-performance, metal-supported SOFCs. Three substrates metal-supported solid oxide fuel cells (SOFCs) were thermally sprayed on Hastelloy. These were composed of a samarium-doped ceria (SDC) ($Ce_{0.8}Sm_{0.2}O_{2-\delta}$) electrolyte layer and Ni-$Ce_{0.8}Sm_{0.2}O_{2-\delta}$ (Ni-SDC) cermet anode. The cathode, a $Sm_{0.5}Sr_{0.5}CoO_3$ (SSCo)-SDC composite, was screen-printed and fired in situ. The anode was produced by suspension plasma spraying (SPS) using an axial injection plasma torch. The SDC electrolyte was produced by high-velocity oxy-fuel (HVOF) spraying of liquid suspension feedstock, using propylene fuel (DJ-2700).

Saeidi et al. (2011) sprayed using a Praxair (CO-210-24) high-velocity oxy-fuel (HVOF) and vacuum plasma spraying (VPS), coatings made of CoNiCrAlY powder. Free-standing coatings underwent vacuum annealing at different temperatures for times of up to 840 h. Feedstock powder, and as-sprayed and annealed coatings, were characterized by scanning electron microscopy (SEM), energy dispersive spectroscopy (EDS), and X-ray diffraction (XRD). The hardness and Young's modulus of the as-sprayed and the annealed HVOF and VPS coatings were measured, including the determination of Young's moduli of the individual phases via nanoindentation and measurements of Young's moduli of coatings at temperatures up to 500 °C. The Eshelby inclusion model was employed to investigate the effect of microstructures on the coatings' mechanical properties. The sensitivity of the mechanical properties to microstructural details was confirmed. Young's modulus was constant up to ~200 °C, and then decreased with increase in measurement temperature. The annealing process increased Young's modulus because of a combination of decreased porosity and β volume fraction. Oxide stringers in the HVOF coating

maintained its higher hardness than the VPS coating, even after annealing.

Stiegler et al. (2012) deposited hydroxyapatite (HA) coatings on Ti plates by the high-velocity suspension flame spraying (HV-SPS) technique. The process characteristic, the microstructure, and phase composition of the coatings were significantly influenced by the solvent and by the design of the combustion chamber of the HV-SPS torch. Water-based suspensions always led to fairly low surface temperatures (350 °C) and deposition efficiencies <40% and produced coatings with low amount of crystalline, which tends to dissolve very rapidly in simulated body fluid (SBF) solutions. DEG-based suspensions, when sprayed with a properly designed combustion chamber, produce deposition efficiencies of 45–55% and high surface temperatures (550–600 °C). In these coatings, the degree of crystallinity increased from the bottom layer to the top layer, probably because the increasingly large surface temperature can eventually favor re-crystallization of individual lamellae during cooling. These coatings were much more stable in simulated body fluid solutions.

7.3.5 Industrial Applications

HVOF/HVAF and associated technologies have been widely used for the spraying of metals, cermets, and a few ceramic protective coatings, which are typically 100–300 μm thick, onto surfaces of engineering components to allow for their use under demanding conditions. Initially, the focus was on wear-resistant coatings, but now the coatings are extensively studied for their corrosion and oxidation resistance, which can be better than those produced by other thermal spraying technologies. These coatings have found wide applications in marine, aircraft, automotive, and other industries. They are also used for reclaiming a wide range of petrochemical process components.

7.3.5.1 Metals

Pure aluminum coatings with low porosity were obtained with the lowest oxygen/fuel ratio with HVOF [Evdokimenko et al. (2001)], and porosity values down to 1% were obtained with HVAF [Evdokimenko et al. (2001)]. Iron-aluminide was sprayed with HVOF with 7 to 15 wt.% oxide inclusion [Totemeier et al. (2003)]. Among the alloys, the most popular is Ni-Cr, for which adherence is very high on stainless steel substrates (more than 100 MPa) and is not affected by thermal fatigue [Higuera et al. (2002)]. When HVAF sprayed onto aluminum substrates, NiCr particles exhibit a strong bond with the substrate with an important penetration into it but with no evidence of chemical bonding [Trompetter et al. (2005)]. NiCr or NiCrSiB coatings are used against the severe corrosive environment in waste-to-energy boilers [Li and Wang (2002) and Kawahara (2007)]. NiCrMoNb is also used against corrosion [Yilbas et al. (2003)].

In thermal barrier coatings, upon exposure to high-temperature gases, a thin oxide scale, the thermally grown oxide (TGO), forms at the bond-coat/topcoat interface and continues to grow in thickness during thermal cycling. The TGO's uneven and rapid growth results in localized stress concentrations where cracks can nucleate and initiate the failure dynamics. To achieve a dense and uniform α-Al_2O_3 TGO scale with a slow growth rate, HVOF coatings of superalloys have been used [Yang et al. (2002), Rajasekaran et al. (2011), Lima et al. (2007), Yang et al. (2002), Lima et al. (2007), Ni et al. (2011), Chen et al. (2008), Brandl et al. (1997), Scrivani et al. (2003), Rajasekaran et al. (2011), Ni et al. (2011), Lima and Guilemany (1997), Richer et al. (2010), Fossati et al. (2010), Jang et al. (2006), Yuan et al. (2008)]. Coatings have been studied for the influence of various parameters such as bond-coat thickness and roughness, composition, mechanical properties evolution through the topcoat, bond coat and substrate, spray process. HVOF-sprayed bond-coat coatings have been compared to those obtained by plasma spraying (APS and VPS), cold spraying, and D-gun. They have higher aluminum content, and the thermally grown oxide (TGO) developed during cyclic oxidation contains fewer mixed oxide clusters and a stable Al_2O_3 layer. Thus, the TGO has a low growth rate and a low tendency for crack propagation, which leads to improved TBC durability. A typical HVOF bond coat of NiCrAlY (Cr: 24–26, Al: 4–6, Y: 0.4–0.7, Ni: bal.) with a narrow size distribution (47–57 μm) sprayed with JP-5000 HP/HVOF (kerosene-oxygen) is presented in Fig. 7.49a, representing substrate, bond coat, and topcoat, the bond coat microstructure being presented in Fig. 7.49b. It has a lamellar structure containing dispersed inclusions of aluminum oxide, as well as pores of varying sizes for a total porosity of 3.2%. Its average roughness Ra is 5.38 μm. The bond coat presents broader and lower diffraction peaks of the γ-Ni_3Al phase than the starting NiCrAlY powder.

HVOF metal coatings (Stellite®6) have excellent resistance to cavitation erosion [Kumar et al. (2005)]. Bulk amorphous coatings (NiTiZrSiSn) have also been successfully sprayed when reducing in-flight oxidation by reducing the oxygen to fuel gas ratio [Yuan et al. (2008)].

[Sidhu et al. (2006)] analyzed and compared the mechanical properties and microstructure details at the interface of HVOF-sprayed NiCr-coated boiler tube steels, namely ASTM- SA-210 grade A1, ASTM-SA213-T-11, and ASTM-SA213-T-22. Coatings were developed by two different techniques, and in these techniques, liquefied petroleum gas was used as the fuel gas. First, the coatings were characterized by metallographic, scanning electron microscopy/energy-dispersive X-ray analysis, X-ray diffraction, surface roughness, and microhardness, and then

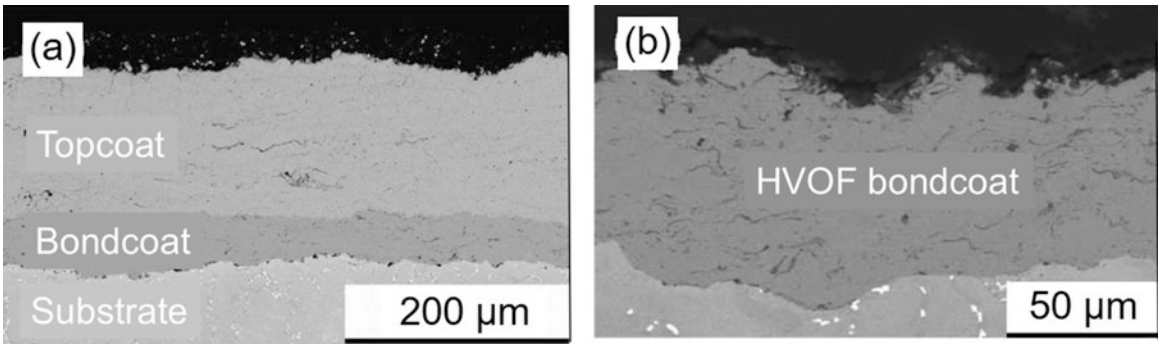

Fig. 7.49 (**a**) Cross-section of detonation-sprayed TBC using hollow sphere YSZ powder D-gun sprayed with the HVOF bond coat, (**b**) Microstructure of the HVOF NiCrAlY coating in the as-sprayed state. (Reprinted with kind permission from Elsevier [Ahmed et al. (2002)])

were subjected to erosion testing. An attempt has been made to describe the transformations taking place during thermal spraying. It was concluded that the HVOF wire-spraying process offered a technically viable and cost-effective alternative to the HVOF powder spraying process for applications in an energy generation power plant with a point view of life enhancement and to minimize the tube failures because it gives a coating having better resistance to erosion.

Trompetter et al. (2010) investigated the effect of substrate surface oxides on splat-substrate bonding by thermally spraying NiCr particles onto aluminum substrates with surface oxide layers grown hydrothermally and electro-chemically. Cross-sections of bonded solid and molten splats revealed substantial deformation of both the substrate and the surface oxide. In spite of the substantial substrate deformation, there was no significant loss of the surface oxide material and there was no observed diffusion of the substrate oxide into the NiCr particle or vice versa. For solid splats, the substrate oxide was still present over the entire splat-substrate interface; however, for molten splats, the oxide had been penetrated in several locations, allowing close proximity of the splat metal to the substrate metal. These results strengthen the theory that oxide layers impede bonding and that successful bonding occurs only when the surface oxide is substantially deformed or disrupted to produce mechanically interlocking features at the interface.

Trompetter et al. (2016) studied Ni-Cr alloy particles thermally sprayed onto a variety of substrate materials using the high-velocity air fuel (HVAF) technique. Although the various substrate materials were sprayed using identical powder material and thermal spray conditions, the type and variation of splat morphologies were strongly dependent on the substrate material. Predominantly solid splats were observed penetrating deeply into softer substrates, such as aluminum, whereas molten splats were observed on harder substrates, which resisted particle penetration. The observed correlation between molten splats and substrate hardness could be due a dependency of deposition efficiencies of solid and molten splats on the substrate material. However, it was found that the conversion of particle kinetic energy into plastic deformation and heat, depending on substrate hardness, can make a significant contribution toward explaining the observed behavior.

[Han et al. (2017)] deposited the chemical composition of NiCoCrAlHfYSi with a suitable particle size, using an activated combustion-high velocity air fuel (AC-HVAF) spray. AC-HVAF is a potentially promising process because dense, continuous, and pure alumina can be formed on the surface of the MCrAlY metallic coatings after isothermal oxidation exposure. The NiCoCrAlHfYSi (Amdry386) and NiCo-CrAlTaY (Amdry-997) coatings were produced using AC- HVAF and APS, respectively. Isothermal oxidation was subsequently conducted at 1050 °C in air for 200 h. This paper compared the characteristics of four coated samples, including the surface roughness, elastic modulus, hardness, oxide content, microstructural characteristics, and phase evolution of thermally grown oxides (TGO). The growth of both the TGO and alumina scales in the TGO of the HVAF386 coating was relatively rapid. The θ- to α-alumina phase transformation was strongly determined by the Hf and Si dopants in the HVAF-386 coating. Finally, the extent of grain refinement and deformation storage energy in the HVAF997 coatings were determined to be significantly crucial for the θ- to α-alumina phase transformation.

[Sadeghimeresht et al. (2016)] considered that the selection of the thermal spray process is the most important step toward a proper coating solution for a given application, as important coating characteristics such as adhesion and microstructure are highly dependent on it. In their work, they performed a process-microstructure-properties-performance correlation in order to figure out the main characteristics and corrosion performance of the coatings produced by different thermal spray techniques such as high-velocity air fuel (HVAF), high-velocity oxy fuel (HVOF), and atmospheric

plasma spraying (APS). Previously optimized HVOF and APS process parameters were used to deposit Ni, NiCr, and NiAl coatings and compare with HVAF-sprayed coatings with randomly selected process parameters. As the HVAF process presented the best coating characteristics and corrosion behavior, a few process parameters such as feed rate and standoff distance (SoD) were investigated to systematically optimize the HVAF coatings in terms of low porosity and high corrosion resistance. Ni and NiAl coatings with lower porosity and better corrosion behavior were obtained at an average SoD of 300 mm and feed rate of 150 g/min. The NiCr coating sprayed at a standoff distance of 250 mm and feed rate of 75 g/min showed the highest corrosion resistance among all the investigated samples.

[Milanti et al. (2015)] studied novel Fe-based coatings to evaluate the microstructural details and corrosion properties using two different generations of HVAF spray guns. These two generations of HVAF guns are activated combustion HVAF (AC-HVAF, second generation) M2 gun and supersonic air fuel HVAF (SAF, third generation) M3 gun. Structural details were analyzed using X-ray diffractometry and a field-emission scanning electron microscope. Higher denseness with homogeneous microstructures was achieved for the Fe-based coating deposited by the M3 process. Such coatings exhibited higher particle deformation and lower oxide content compared to coatings manufactured with M2 gun. Corrosion properties were studied by open-cell potential measurements and electrochemical impedance spectroscopy. The lower porosity and higher interlamellar cohesion of the coating manufactured with the M3 gun prevent the electrolyte from penetrating through the coating and arriving to the substrate, enhancing the overall corrosion resistance. This can be explained by the improved microstructures and coating performance.

Gupta et al. (2018) pointed out that the development of thermal barrier coatings (TBCs) manufactured by suspension plasma spraying (SPS) is of high commercial interest as SPS has been shown capable of producing highly porous columnar microstructures similar to the conventionally used electron beam–physical vapor deposition. However, the lifetime of SPS coatings needs to be improved further to be used in commercial applications. The bond-coat microstructure, as well as top-coat–bond-coat interface topography, affects the TBC lifetime significantly. The objective of this work was to investigate the influence of different bond coat deposition processes on SPS top-coats. In this work, a NiCoCrAlY bond coat deposited by high-velocity air fuel (HVAF) was compared to commercial vacuum plasma-sprayed NiCoCrAlY and PtAl diffusion bond coats. All bond-coat variations were prepared with and without grit blasting the bond-coat surface. SPS was used to deposit the top coats on all samples using the same spray parameters.

Warm spraying has been developed, in which powder particles are accelerated and simultaneously heated, and deposited onto a suitable substrate in thermally softened solid state. Accordingly, Kim et al. (2010) sprayed commercially available titanium powder onto a steel substrate by the spraying process. Microstructural developments and deposition behaviors from a deposited single particle to a thick coating layer were observed by high-resolution electron microscopes. A single titanium particle sprayed onto the substrate was severely deformed and grain-refined mainly along the interfacial boundary of the particle/substrate by the impact of the sprayed particle. A successive impact by another particle further deformed the previously deposited particle and induced additional grain refinement of the remaining part. In a thick coating layer, severe deformation and grain refinement were also observed. The results have demonstrated the complex deposition behavior of the sprayed particles in warm spraying using thermally softened metallic powder particles.

When comparing Ni-20 wt % Cr sprayed with gaseous or liquid fuel, the latter results in less oxidation, less porosity, and less evidence of melting. Accordingly, such coatings are able to withstand more than 3000 h exposure to neutral salt spray tests without substrate corrosion, which is two orders of magnitude more than what is obtained with gaseous fuels [Aalamialeagha et al. (2003)]. Materials sprayed are almost the same as those sprayed with gaseous fuel. The main differences are the higher velocities and the lower temperatures.

With copper particles sprayed at 500 m/s, very dense coatings were obtained when the particle temperatures were such that the particles were highly deformable just below the melting temperature [Kawakita et al. (2006)]. The same results were obtained with stainless steel, which, with addition of molybdenum, resulted in good corrosion-resistance coatings [Kawakita et al. (2005)] that were also harder than wrought material [Totemeier et al. (2005)]. Stellite®-6 was also excellent for repairing cavitation damage in turbines and pumps [Kumar et al. (2005)]. Similar results were obtained with Ni-Cr coatings, which had adhesion values of over 70 MPa on 9Cr-1Mo steel, and which presented excellent steam-oxidation resistance [Sundararajan et al. (2004a, b)]. When spraying MCrAlY coatings with such HVOF guns with an inert gas shroud, the coating oxygen levels were almost as low as those obtained in vacuum plasma spraying (VPS) [Pant et al. (2007)]. It was also possible to achieve amorphous phase formation of Zr-based alloy coatings (up to 62%) due to low oxide formation. Of course, if the coating is overheated by spraying it with too low stand-off distance [Kim et al. (2001)], no amorphization is possible. When heat treating Co-Mo-Cr-Si coatings at 600 °C, the hardness increases and the friction between the coating and an alumina pin diminishes [Bolelli and Lusvarghi (2006)].

Liquid-fuel HVOF is also used to spray materials in which solid lubricants are incorporated such as WC-Co and fluorinated ethylene-propylene (FEP) copolymer-based material [Marple and Voyer (2001)] or iron sulfide [Wang (2004)].

As with flame or gaseous-fuel HVOF, SHS (self-propagating high-temperature synthesis) reactions can be produced upon spraying, for example, with SiO_2/Ni/Al-Si-Mg powder, resulting in composite materials of $MgAl_2O_4$, Mg_2Si in an Al-Si matrix [Ozdemir et al. (2005)]. A rapid formation of aluminide ($NiAl_3$) can be produced by an exothermic reaction of plated nickel with Al-Si-Mg core powder [Ozdemir et al. (2005)]. In both cases, reactions start in-flight and finish during splat layering. Such composites are rather hard.

Cetegen and Basu (2009) presented a review of the current state-of-the-art in the modeling of liquid chemical precursor droplets and particles injected into high-temperature jets in the form of DC-arc plasmas and high-velocity oxy-fuel flames to form coatings. Conventional thermal-spray processes have typically utilized powders that are melted and deposited as a coating on hardware surfaces. However, production of coatings utilizing liquid precursors has emerged in the last decade as a viable alternative to powder deposition. Use of liquid precursors has advantages over powder in terms of their relative ease of feeding and tailoring of chemical compositions. In this, the authors reviewed the modeling approaches to injection of liquid precursors and particles into plasmas and high-velocity oxy-fuel flames. Modeling approaches for the high-temperature DC-arc plasma and oxy-fuel flame jets were first reviewed. This was followed by the liquid spray and droplet-level models of the liquid precursors injected into these high-temperature jets. The various knowledge gaps in detailed modeling are identified and possible research directions are suggested in certain areas.

7.3.5.2 Cermets

These coatings have been intensively studied from the beginning, and the success of HVOF or HVAF processes relies on them [Ahmed and Hadfield (2002), Parco et al. (2006), Perry et al. (2002), Deng et al. (2007), Jacobs et al. (1998), Jacobs et al. (1999), Marple and Lima (2005), Moskowitz and Trelewicz (1997), Guilemany et al. (2005), Ji et al. (2007), Matthews et al. (2004), Mizuno and Kitamura (2007)]. The cermets, which are mostly sprayed, are WC-Co and Cr_3C_2-NiCr. One of the key issues for coating quality is to avoid carbide decomposition, or at least reducing it as much as possible. Spraying with fuel-rich mixtures [5.122], and using HVAF preferentially to HVOF [Parco et al. (2006), Jacobs et al. (1999)], allows for reducing drastically or even avoiding carbide decomposition. These coatings are used for their wear resistance (friction and erosion), and corrosion resistance, especially for those containing NiCr. Other composites are also sprayed, such as MoB/CoCr [Mizuno and Kitamura (2007)], against erosion by molten Al-Zn alloys, Ni-Ti-C [Horlock et al. (2005)], which, by SHS reaction, after spraying, contains TiC in a Ni-rich solution together with NiTi, TiO_2, and $NiTiO_3$, and lastly silicon nitride-based coatings [Thiele et al. (2002)] where the silicon nitride is imbedded in a complex oxide binder matrix. Such coatings exhibit satisfactory corrosion and thermal-shock resistance.

With cermets such as WC-Co and Cr_3C_2-NiCr, rather dense coatings are obtained with Cr_3C_2-NiCr coatings being more protective against corrosion than WC-Co ones [de Villiers Lovelock (1998); Otsubo et al. (2000); Sidhu et al. (2007); Bolelli et al. (2006); Ishikawa et al. (2007); Maiti et al. (2007); Sidhu et al. (2006); Sidhu et al. (2007)]. This fact is attributed to the formation of Cr_2O_3, NiO, and $NiCr_2O_4$ [Bolelli et al. (2006)]. WC-20 wt% Cr_3C_2-7 wt% Ni cermet coatings have good resistance to sliding wear [Bolelli et al. (2006)]. Adding WC to the powder [Maiti et al (2007)] improved the hardness of WC-Co-Cr. Cr_3C_2-NiCr coatings on Ni base super alloys provided a good resistance to hot corrosion [Sidhu et al. (2007)]. At last, WC-Co + CoMoCrSi coatings are harder but less tough than electrolytic hard chrome (EHC) coatings, and their two-body sliding resistance definitively overcomes that of EHC coatings, but they experience a comparable or even higher mass loss when subjected to three-body abrasion conditions [Ishikawa et al. (2007)]. WC-NiCrFeSiB coatings on Ni- and Fe-based super alloys show excellent oxidation and hot corrosion resistance at 800°C [Sidhu et al. (2007b)].

Optimized processing windows for spraying high-quality metal carbide-based coatings were developed using particle diagnostic technology by Ang et al. (2016). The cermet coatings were produced via the high-velocity oxygen-fuel (HVOF) spray process and were proposed for service applications such as marine hydraulics. The traditional "trial and error" method for developing coating process parameters is not technically robust, as well as being costly and time consuming. Instead, this contribution investigated the use of real-time monitoring of parameters associated with the HVOF flame jets and particles using in-flight particle diagnostics. Subsequently, coatings can be produced with knowledge concerning the molten particle size, temperature, and velocity profile. The analytical results allowed identification of optimized coating process windows, which translate into coatings of lower porosity and improved mechanical performance.

Bartuli et al. (2005) performed the parametric study of nanocrystalline WC-Co coatings deposited by high-velocity oxyfuel from commercial nanostructured composite powders. Processing parameters were optimized for maximal retention of the nanocrystalline size and for minimal de-carburation of the ceramic reinforcement. Thermochemical and gas-dynamical properties of gas and particle flows

within the combustion flame were identified in various operating conditions by computational fluid-dynamics (CFD) simulation. Significant improvements in the mechanical properties of the coatings were obtained: a decrease of the friction coefficient was measured for the nanostructured coatings, together with an increase of microhardness and fracture toughness.

According to Bobzin et al. (2016), thermally sprayed Fe-based coatings reinforced by TiC particles are a cost-effective alternative to carbide coatings such as WC/CoCr, Cr_3C_2/NiCr, and hard chrome coatings. They feature good wear resistance and—with sufficient number of alloying elements like Cr and Ni—high corrosion resistance. In hydraulic systems, the piston is usually coated with hard chrome coatings for protection against corrosion and wear. New water-based hydraulic fluids require an adaption of the coating system. In order to investigate the wear and corrosion resistance of Fe/TiC, a novel powder consisting of a $FeCr_{27}Ni_{18}Mo_3$ matrix and 34 wt.% TiC was applied by HVOF and compared to reference samples made of WC/CoCr (HVAF) and hard chrome. Besides an in-depth coating characterization (metallographic analyses, electron microprobe analyzer–EMPA), wear resistance was tested under reverse sliding in a water-based hydraulic fluid. The novel Fe/TiC coatings showed good wear protection properties, which are comparable to conventional coatings like WC/CoCr (HVAF) and electroplated hard chrome coatings. Corrosion resistance was determined by polarization in application-oriented electrolytes (hydraulic fluid at 60 °C, artificial sea water at RT). The corrosion resistance of the investigated iron-based coatings at 60 °C was superior to that of the reference coatings for both hydraulic fluids. Select coatings were tested in an application-oriented hydraulic test bench with HFC hydraulic fluid (water polymer solutions), showing comparably good wear and corrosion resistance as the hard chrome-coated reference.

7.3.5.3 Ceramics

Ceramic coatings are not the strongest point of HVOF or HVAF processes because the process is more prone to achieve high velocities than high temperatures. Titania is rather well melted in processes working with propylene [Lima and Marple (2003a) and (2003b)]. High Weibull modulus values are obtained compared to other spray techniques and coatings are very dense and uniform, with rutile being the major phase. Alumina is mostly sprayed with chromia, which allows for stabilizing the α phase [Stahr et al. (2006)]. At last, zirconia stabilized with yttria, with particles below 10 μm, can be sprayed, and it is suggested that sintering can play a role with good adhesive and cohesive coatings [Dobbins et al. (2003)].

7.3.5.4 Polymers

Among the sprayed polymers, Nylon 11 is the one most frequently used, with or without ceramic doping [Petrovicova et al. (2000), Ivosevic et al. (2005), Jackson et al. (2007)]. The residence time in the HVOF is generally short enough (~ 1 ms) to limit its degradation and a change of its color. Such coatings, when used for their dry sliding wear performance, are more wear resistant without doping powders because those additions may lead to abrasive and fatigue wear.

Thermal spray of polymers has had limited investigation due to the narrow processing windows that are inherent to polymer powders, especially their low temperatures of thermal degradation [Withy et al. (2008)]. The polymer polyaryl-ether-ether-ketone (PEEK) has a continuous use temperature of 260 °C, does not suffer significant thermal degradation below 500 °C [Lu et al. (1996)], and has high resistance to alkaline and acidic attack. These properties led [Withy et al. (2008)] to select PEEK for investigation. To minimize thermal degradation of the particles, the high-velocity air-fuel technique was used. To investigate the effect of substrate pretreatment on single-splat properties, single splats were collected on aluminum 5052 substrates with six different pretreatments. The single splats collected were imaged by scanning electron microscopy and image analysis was performed with ImageJ, an open source scientific graphics package. On substrates held at 323 °C, it was found that substrate pretreatment had a significant effect on the circularity and area of single splats, and also on the number of splats deposited on the substrates. Increases in splat circularity, area, and the number of splats deposited on the surface were linked to the decrease in chemisorbed water on the substrate surface and the decrease of surface roughness. This proved that surface chemistry and roughness are crucial to forming single splats with good properties, which will lead to coatings of good properties.

7.4 Pulse Detonation Thermal Spray

The pulse detonation thermal spray (PDTS), commonly known as detonation gun (D-gun), was developed in the 1950s in the USA by Union Carbide Corporation (Now Praxair) in 1955, Poorman et al. (1955), and independently in 1969 at the Institute of Materials Science (Kiev, Ukraine) in the former Soviet Union, Nevgod et al. (1987a, b), and Barisov et al. (1990).The technology is closer to cold spray or HVOF/HVAF than conventional thermal spray coating since it relies heavily on the acceleration of particles to be sprayed to high velocities, projecting them toward the substrate in

essentially a softened solid-state where they deform on impact, forming the coating. In contrast to other combustion processes, where the flame is a subsonic wave sustained by a chemical reaction, detonation wave is a shock wave sustained by the energy of chemical reactions in a compressed explosive gas mixture. The pressure ratio of burned to unburned gases, $p_b / p_u \approx 13–25$ and $\rho_b/\rho_u \approx 1.4–2$, where ρ_b is the specific mass of burned gases and ρ_u that of unburned ones [Glassman (1977)]. These ratios are considerably higher than those of atmospheric pressure flames where the density ratio of the hot gases is typically in the range ($\rho_b/\rho_u \approx 0.06–0.25$), at pressures slightly below atmospheric pressure ($p_b \approx 80$ to 90 kPa). The ideal detonation wave travels in gases at constant speed close to the Chapman–Jouguet velocity (v_{CJ}), which is between 1500 and 3000 m/s, depending on the type and composition of the fuel-oxidizer mixture. The pressure just behind the detonation wave can be as high as 20 ~ 30 times the ambient pressure. In this section, a brief review of the basic concepts behind the technology is presented, followed by typical D-gun spray coating applications.

7.4.1 Basic Concepts

As illustrated in Fig. 7.50, the basic concept behind a detonation gun (D-gun) is to generate a detonation wave in a confined space (Barrel) open at one end, through the combustion of a well-defined mixture of oxygen and an appropriate fuel such as hydrogen, acetylene, or propane. As the fuel/oxygen mixture is ignited, a high-pressure shock wave (detonation wave) is generated which, depending on the composition of the fuel/oxygen mixture, can have a gas temperature as high as 4000 K and a velocity of the shock wave up to 3500 m/s. As the wave propagates toward the open end of the barrel, it entrains, heats, and accelerate a small charge of powder pre-placed in the combustion chamber to a plasticizing stage (skin melting) and relatively high velocities of the order of 1200 m/s. On immerging from the open end of the barrel, the powder is projected towards the substrate (work piece), placed a distance typically between 100 and 200 mm from the end of the barrel, on which the coating is formed on impact through plastic deformation. The process is cyclic, involving the repetitive spraying of the powder in successive “shots” driven by a repetitive explosive combustion at a frequency in the 1–15 Hz range. At the end of each cycle, the chamber is flushed with nitrogen to remove any remaining “hot” powder particles from the chamber as these can otherwise detonate the explosive mixture in an irregular fashion and render the whole process uncontrollable. Recent studies by Endo et al. (2016) reported experiments using a high-frequency pulse detonation combustor (HFPDC) operated in the liquid-purge mode at frequencies up to 150 Hz.

In a typical D-gun, the barrel is made of a heavy wall, water-cooled cylindrical tube closed at one end with an internal dimeter, $d_i = 10$ to 40 mm, and length, L_T, of up to 1 or 1.5 m. As a rule of thumb, $L_T = 40$ to 80 x d_i up to 100 d_i. The geometry of the detonation chamber must allow for steady detonation, which also depends on the mixture composition, temperature, and pressure. The fuel and oxidizer feed are either separately injected into the closed end of the barrel tube or premixed prior to injection. Charge ignition is made using a sparkplug. The detonation wave tends to propagate in all directions, including into the gas supply, creating an explosion hazard. The effect is called "backfiring," which must be considered in the design of the gas detonation equipment. The problem is usually solved through the use of an inert gas, such as nitrogen, in order to separate different portions of the fuel from one another and to prevent propagation of the detonation wave into the gas distributor. Numerous other safety features are introduced in the gun design to avoid faulty ignition of the fuel; these generally involve the periodic purging of the barrel tube with nitrogen at the end of every ignition and the nitrogen purging the fuel and oxidant mechanical or electromagnetic valves. The material to be sprayed is introduced into the gun barrel in the form of small charges, typically of less than 1 g each, of fine powder with a particle size in the range of 10 to 40 μm. The position of the powder feed in the barrel is a critical parameter in the design and operation of the gun. The powder charge is either axially introduced from the closed end of the barrel using a coaxial probe that can deliver the powder to different locations on the barrel axis, as shown in Fig. 7.50a, or laterally (radially) further downstream at any desired locations, as shown in Fig. 7.50b.

According to [Kadyrov E. and V. Kadyrov (1995)], the process consists essentially of the following four principal steps, schematically represented in Fig. 7.51:

(a) Injection of an oxygen and fuel mixture into the combustion chamber
(b) Injection of the powder “charge” followed by a nitrogen purge between the ignition point and the combustion gas mixture to separate the gas supply from the explosive gases and prevent backfiring
(c) Ignition of the combustion gas mixture giving rise to detonation and the creation of a detonation wave, which entrains, heats, and accelerates the powder toward the open end of the barrel and projects it on the substrate, forming the coating
(d) Nitrogen purge of the barrel at the end of the cycle [Kadyrov E. and V. Kadyrov (1995)]

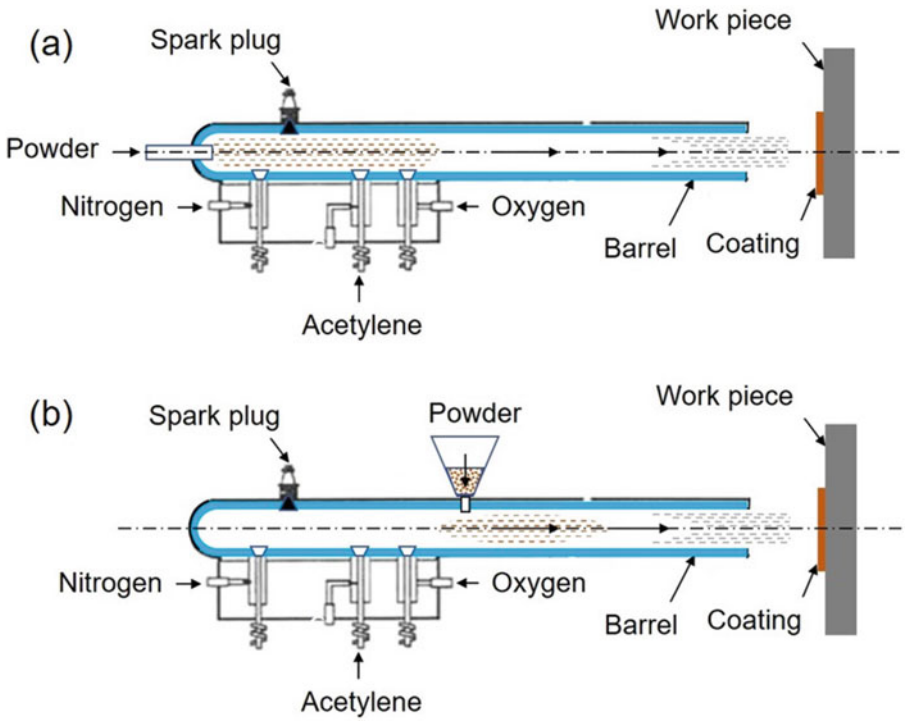

Fig. 7.50 Schematic of detonation gun spray coating process (**a**) axial powder feed (**b**) lateral (radial) powder feed

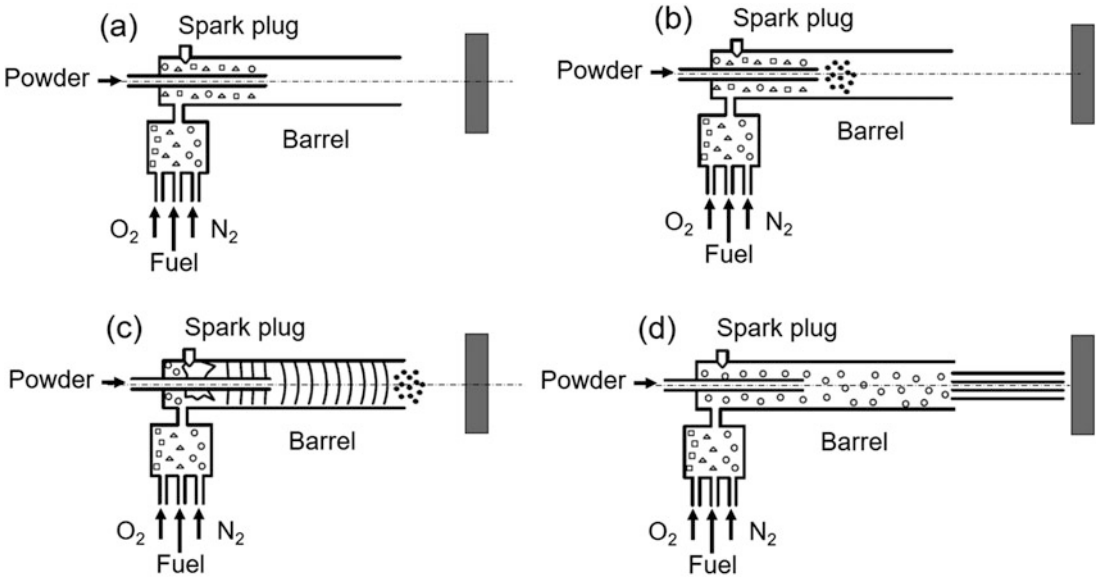

Fig. 7.51 Schematic of the detonation process cycle (**a**) injection of fuel and oxygen into combustion chamber, (**b**) injection of powder charge and nitrogen gas, (**c**) detonation of the combustion mixture, powder acceleration, and projection on the substrate, (**d**) nitrogen purge of the chamber in preparation for the next cycle [Kadyrov and Kadyrov (1995)]. (Reprinted with kind permission from Springer Science Business Media, copyright © ASM International)

Steps (a) and (b) are the preparatory ones, while steps (**c**) and (**d**) are self-governing ones independent of the process control system. The injection of fuel into the D-gun and the mixing of the fuel with the incoming oxidizer or injection of the fuel-oxidizer mixture start the new operation cycle. A mechanical or electromagnetic valve is used in industrial

guns to prevent detonations or shocks into the feeding system and provide sufficient time for the mixing of the fuel with the oxidizer. It is important to note that the detonation coating process is, by definition, an intermittent process that allows the temperature of the substrate to be kept low, generally below 100 °C, avoiding undesirable thermal deformation of the substrate.

The deposition rate of the coating material using the D-gun is directly dependent on the mass of the ***charge*** that is projected at every cycle, the ***frequency of ignition*** cycle, and the ***deposition efficiency***. The latter is the fraction of the projected powder that is deposited on the substrate. The ignition frequency, f, is inversely proportionate to the duration of the cycle, t_c, which is composed of six characteristic time intervals [Kharlamov (2004)]:

$$f = 1/t_c \tag{7.8}$$

with

$$t_c = \Delta t_{gfl} + \Delta t_{pfl} + \Delta t_{pr} + \Delta t_{in} + \Delta t_{tr} + \Delta t_{exp} \tag{7.9}$$

where

Δt_{gfl} barrel filling time by fresh gas mixture
Δt_{pfl} barrel filling time with powder charge
Δt_{pr} time for nitrogen purging
Δt_{in} time for detonation initiation
Δt_{tr} time for detonation traversing the barrel Δt_{exp} exhaust of detonation products and powder particles and nitrogen purge

The dynamic filling, Δt_{gfl}, and exhaust/purging, Δt_{exp}, processes have the longest durations, which can be shortened by operating at higher dynamic pressures, with an upper limit due to filling losses. The length and the volume of the barrel, together with the pre-detonation chamber and the filling velocity, determine the filling time, Δt_{gfl}, since the mass flow into the combustor has to traverse the combustor length [Kharlamov (2004)]. The compressibility effects occurring when injected gas velocity is over Mach 0.5 limit the fill rate. A full cycle of the detonation gun, t_c, can then be calculated by summing all of characteristic times. An optimum exists because of the coupling of the length, dynamic pressure, and operating frequency of a barrel. Practical values are up to 10 Hz for a 1 m long combustor operating at an initial pressure of 0.1 MPa [Kharlamov (2004)]. When using multiple injection locations, this frequency limit could be overcome [Roy et al. (2004)]. While the length of the barrel can reach $100xd_i$ [Kharlamov (2004)], consideration should be given to the fact that half of the gas thermal energy is lost after $40xd_i$.

The minimum barrel diameter depends on heat losses to the tube wall and is typically 15–20 mm for most fuels and particle materials. A barrel 15 mm in diameter is sufficient for spraying cermets of tungsten carbide-metal when using acetylene, and a barrel 40 mm in diameter is necessary when using propane [Nikolaev et al. (2003)]. According to [Kharlamov (2004)], varying the barrel cross-sectional area along its length allows for a more uniform filling of the barrel. It is possible to use a nozzle at the barrel end to improve the performance [Roy et al. (2004)]. Contrary to nozzles of steady-flow devices, D-gun nozzles operate at essentially unsteady conditions and their design and optimization require considering the whole operation process. Attaching a nozzle to the end of the detonation tube makes it possible to gradually expand gases and decrease the rate of pressure drop in the tube. However, the nozzle increases the length of the barrel and thereby decreases the operation frequency.

Turbulence, caused by the roughness of the internal surfaces of the D-gun barrel, while promoting a better mixing of the powder with the combustion products, leads to increased heat losses to the wall. Roughness can be achieved by threaded grooves of various profiles, made along the entire length of the barrel, or in individual sections [Kharlamov (2004)]. When the grooves are located in the barrel inlet section, the pre-detonation distance is shortened, whereas their location at its outlet improves powder mixing and intensifies heat exchange.

Typical supply gas pressures to D-guns are 140–200 kPa (20 to 30 psig). The consumption of gas per unit mass of sprayed matter is four to eight times less than that for HVOF spraying [Kadyrov E. and V. Kadyrov (1995)]. The frequency and noise levels (about 145 dBA) require the detonation to be confined in acoustical enclosures. According to Kadyrov E. and V. Kadyrov (1995), one can image propagation of the detonation wave as a stationary distribution of density, temperature, pressure, and velocity moving with some speed distribution. Figure 7.52 gives a qualitative image of the detonation parameters [Kadyrov E. and V. Kadyrov (1995)]. It is assumed that the thickness of the reaction zone is very thin and that the zone of the reaction products is separated from the initial gas mixture by the detonation wave front. At the leading edge of the detonation wave, the temperature increases rapidly, and then behind the front rises gradually in the reaction zone before decreasing gradually with increasing distance from the wave front (Fig. 7.52b). There are also step-like increases in pressure and specific mass density at the detonation wave front followed by a gradual decrease behind (Fig. 7.52a and c).

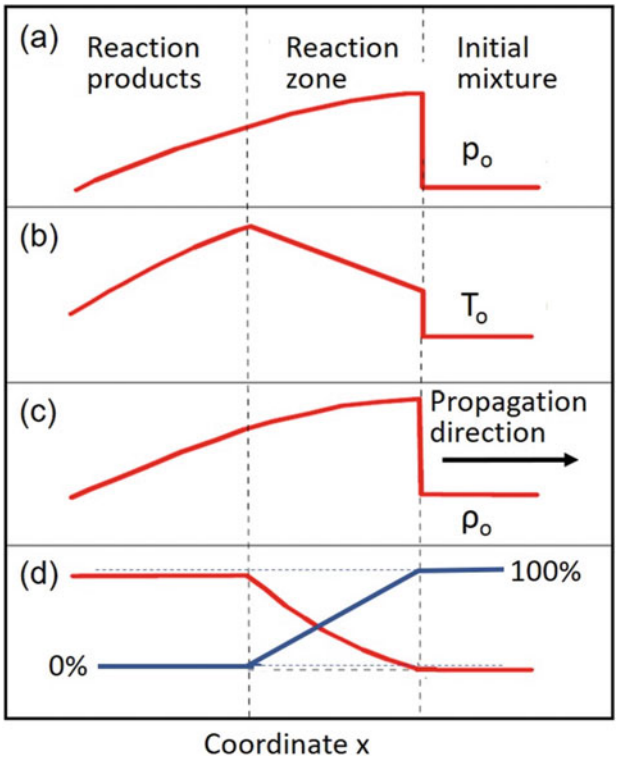

Fig. 7.52 Qualitative picture of detonation parameter variations in the gas (**a**) pressure, (**b**) temperature, (**c**) specific mass, (**d**) distribution of the detonation velocity, v_D, and un-burned gases [Kadyrov and Kadyrov (1995)]. (Reprinted with kind permission from Springer Science Business Media, copyright © ASM International)

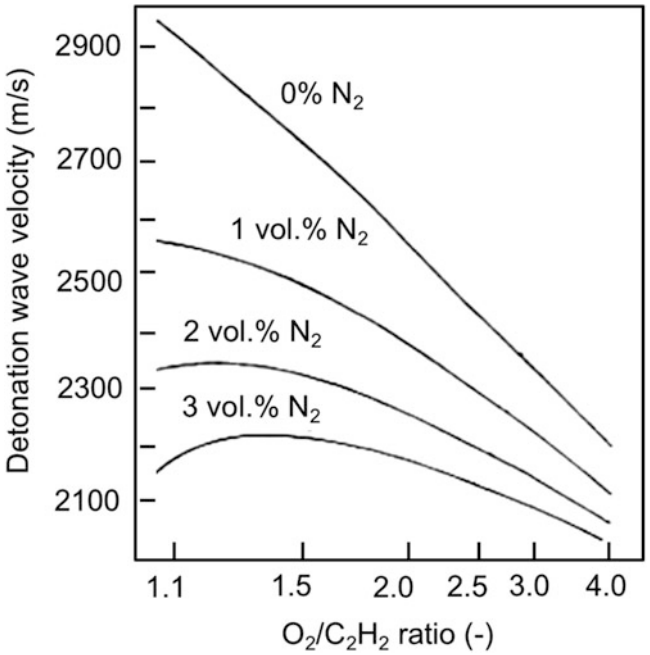

Fig. 7.53 Effect of nitrogen gas on the detonation velocity for different O_2/C_2H_2 mixtures in the presence of different vol. % of nitrogen addition [Kadyrov et al. (1995)]. (Reprinted with kind permission from Springer Science Business Media, copyright © ASM International)

7.4.2 Gas and Particle Dynamics

Numerous studies have been devoted to the understanding of the gas and particle dynamics under pulse detonation thermal spray (PDTS) conditions due to their critical impact on the spraying process and the quality of the coating obtained. The work of [Kadyrov et al. (1995) and Kadyrov (1996)] is pioneering in this area by studying gas dynamic parameters of the detonation powder spray coating process and the mechanism of particle acceleration by the shock wave inside the coating apparatus. Velocities of gas detonation in different gas mixtures are analyzed by applying conventional fluid dynamic theory of detonation for oxygen/hydrogen and oxygen/acetylene mixtures. Their results show that the velocity of the detonation wave varies between 1000 and 3000 m/s depending on the composition of the gas mixture. It is independent of the barrel diameter, provided it exceeds a critical diameter. Once the detonation occurs, its theoretical velocity v_D (m/s) can be calculated by:

$$v_D = \sqrt{2(\gamma^2 - 1)\, Q_o} \tag{7.10}$$

$$T_1 = \frac{2\gamma\, Q_o}{(\gamma + 1)\, c_v} \tag{7.11}$$

$$p_1 = 2(\gamma - 1)\rho_o Q_o \tag{7.12}$$

Where;

γ specific heats ratio of the burned gases ($\gamma = c_p/c_v$)
c_p specific heat at constant pressure
c_v specific heat at constant volume
Q_o specific energy of chemical reaction during detonation,
T_1 temperature of detonation products
p_1 pressure of detonation products

They also point out that detonation parameters are sensitive to the composition of the combustible mixture. The addition of light gases (He, H_2) increases the detonation velocity, while the addition of heavier gases (such as Ar, N_2) decreases the velocity. This is illustrated in Fig. 7.53, representing the velocity of the detonation wave calculated using Eq. (7.10) for different O_2/C_2H_2 mixtures in the presence of nitrogen at different concentrations. The detonation velocity decreases with the increase of the oxygen/acetylene ratio. The introduction of a small percentage of

nitrogen decreases rapidly the velocity of the detonation wave especially for sub-stoichiometric combustion mixtures ($O_2/C_2H_2 < 2.5$). For example, 3 vol.% of nitrogen reduces the detonation velocity by 600 to 800 m/s, with a corresponding drop in particle velocity, leading to a degradation of the quality of the coating. The results of similar calculations using Eqs. (7.10 to 7.12) for different hydrogen/oxygen fuel mixtures in the presence of different additives such as Ar and N_2 are summarized in Table 7.3.

Heat and momentum transfer to particles entrained by the detonation wave are calculated using the conventional equations of motion and heat transfer with or without corrections for supersonic velocities [Kadyrov et al. (1995)], see also Chaps. 4 and 5. Computations were carried out for 20 μm alumina particles injected at three different axial locations in the gun's barrel, $x_i = 0.2$, 0.6 and 1.5 meters, with x_i being the "loading distance" from the point of initiation of the detonation ($x = 0$) to the point of powder injection into the gun. The result given in Fig. 7.54a shows the position of the particle in a 2 m barrel as a function of time for oxygen/acetylene and oxygen/hydrogen stoichiometric mixtures, with initial particle injection at $x_i = 0.2$ m. These show a time-of-flight of the particles until it reaches the exit level of the gun barrel of 2.0 ms, for the oxygen/acetylene mixture, which is shorter than that for the oxygen/hydrogen mixture, 2.7 ms.

The results given in Fig. 7.54b, for the same combustion mixtures and particle system, show that the acceleration and the flight history of the particles in the gun barrel, until they reach its exit level, strongly depend on the injection location of the powder. For example, with a loading distance of 0. 2 m in an O_2/C_2H_2 mixture, the maximum velocity of the particles of 837 m/s is reached against 1152 m/s for a loading distance of 60 cm in the same combustion mixture. Delaying the injection of the powder to the downstream end of the gun barrel, $x_i = 1.5$ m in a 2.0 m gun, gives rise to a very short period of particle entrainment and acceleration by the detonation wave, not allowing the particle to reach its maximum value. These results exhibit several interesting features. The acceleration of the particles from zero to the maximum velocity occurs in a relatively short distance, 0.2 to 0.4 m, in less than 0.6 ms. According to Kadyrov et al. (1995), this is due to the fact that the initial particle

Table 7.3 Parameters of the detonation wave in hydrogen/oxygen mixtures with the addition of different gases [Kadyrov et al. (1995)]

Fuel mixture	p_2/p_1	T_2(K)	v_D(m/s)
$2H_2 + O_2$	18.0	3283	2806
$(2H_2 + O_2) + O_2$	17.4	3390	2302
$(2H_2 + O_2) + 4H_2$	16.0	2976	3627
$(2H_2 + O_2) + N_2$	17.4	3367	2378
$(2H_2 + O_2) + 3\ N_2$	15.6	3003	2033
$(2H_2 + O_2) + 1.5Ar$	17.6	3412	2117

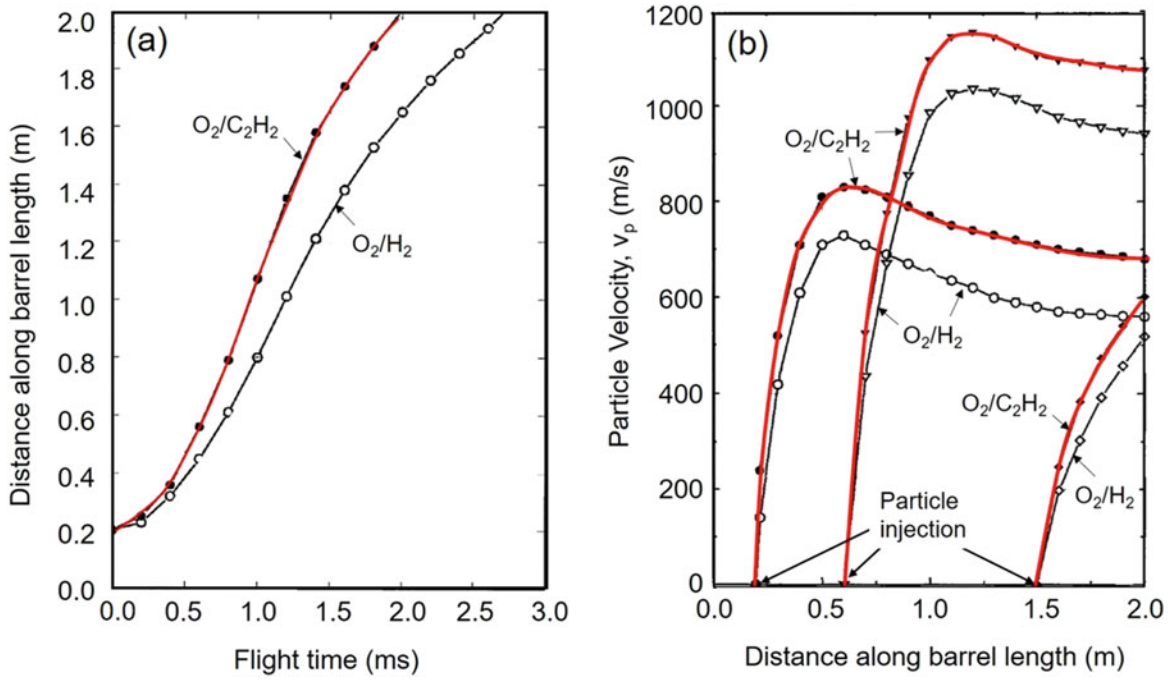

Fig. 7.54 Velocity of 20 μm Al_2O_3 particles versus axial distance for O_2/C_2H_2 (filled symbols) and O_2/H_2 (open symbols) stoichiometric mixtures for different injection locations [Kadyrov E. and V. Kadyrov (1995)]. (Reprinted with kind permission from Springer Science Business Media, copyright © ASM International)

acceleration is provoked by the high-speed gas flow following the detonation wave front. As the detonation wave propagates forward and the particle separates from the wave front, the velocity of the detonation products decreases, and at some point, becomes smaller than that of the particle. With the particle moving faster than the detonation products, the drag force reverses direction and the particle starts to slow down. As can be observed in Fig. 7.54b, the particle exit velocity at the limit of the D-gun barrel, v_{po}, remains strongly dependent on the composition of the detonation mixture and the position of the powder injection in the barrel. For an oxygen/acetylene detonation mix, $v_{po} = 690$, 1080 and 600 m/s for values of $x_i = 0.2$, 0.5 and 1.5 m. The corresponding particle exit velocities for an oxygen/hydrogen mix are 560, 950, and 510 m/s, respectively. As pointed out by Kadyrov et al. (1995), such variations of the particle velocity along its trajectory inside the D-gun are distinctly different from those observed in alternate thermal spray technologies such as HVOF and plasma spraying.

A comprehensive analysis of particle dynamics and heat transfer in pulse detonation thermal spray (PDTS) was reported by Ramadan et al. (20042004). The proposed axisymmetric, 2-D transient compressible gaseous detonation model is based on a three-stage representation of the process, as illustrated in Fig. 7.55. These consist of:

(a) Simultaneous feeding of the reaction mixture (oxygen and acetylene) through a mixing chamber, and of the powder into the tubular D-gun barrel.

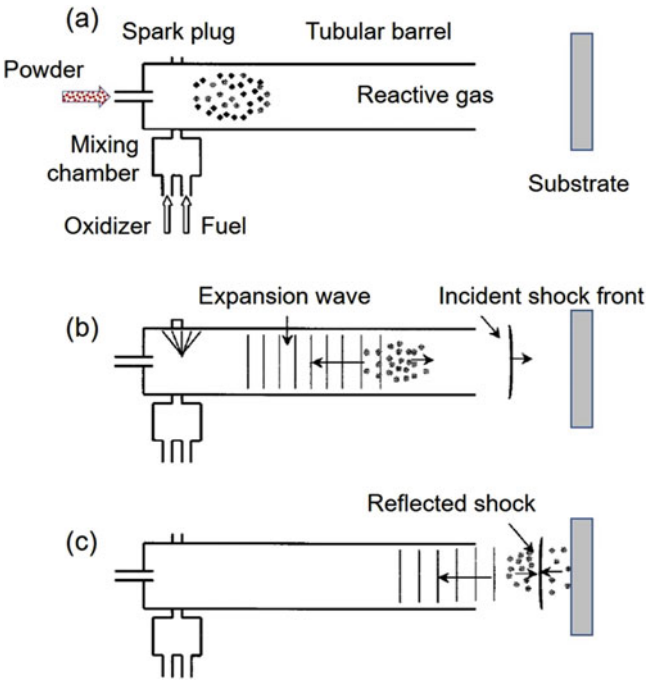

Fig. 7.55 Three-stage representation of the PDTS process [Ramadan et al. (2004)]

(b) Ignition of the combustion mixture using a spark plug near the closed end of the barrel.

(c) Transition from deflagration where the combustion wave propagates at subsonic speed to detonation with the generated high-pressure reactive shock wave (detonation wave) propagates at supersonic speed toward the open end of the barrel entraining and accelerating the supplied powder charge. The collision of the high-velocity, high-temperature powder particles with the substrate forms the coating.

Ramadan et al. (2004) point out that following the detonation front is an expansion wave that propagates rearward toward the breech end of the tube (Fig. 7.55b) and that once the shock front exits the barrel, it starts decaying as the gas expands outside the barrel. Depending on the stand-off distance (SoD), defined as the distance between the barrel exit and the substrate, the shock wave can reach the substrate with a large pressure ratio reflecting back into the path of the incoming particles, as shown in Fig. 7.55c. The interaction between the reflected wave and the particles depends on the particle properties and their size distribution. As the particles impact on the surface of the substrate, they form splats adhering to the substrate depending on their temperature and impact velocity. Following a purge of the barrel to remove any residual powders and combustion products, a new cycle is initiated through the feeding of new fuel-oxidant gas mixture-powder charge into the barrel.

The basic assumptions made in their model can be summarized as follows:

- Axisymmetric 2-D system of coordinates.
- Transient inviscid compressible flow model with the viscous effects confined to the interaction between the gas and the particles.
- Combustion chemical reactions take place in a one-step irreversible process.
- Negligible particle loading effects on the gas flow, that is, one-way coupling between the gas and particulate phases. This is justified by the fact that the mass of powder injected into the barrel is usually smaller than 10–20% of the gas weight.
- Eulerian and Lagrangian representation of the gas and particulate phase governing equations, respectively.

Results were given for a cylindrical detonation gun, 25 mm in internal diameter, with different lengths, L. The reactive gas mixture used was $C_2H_2/O_2/N_2$, with $O/C = 1$, $N_2(\%) = 40$. The resulting detonation wave speed for this mixture was 2464 m/s. The sprayed particles were alumina with three different diameters: 10, 20 and 30 μm. The stand-off distance (SoD) taken is six tube diameters, that is, the substrate was far enough from the barrel exit plane so that the

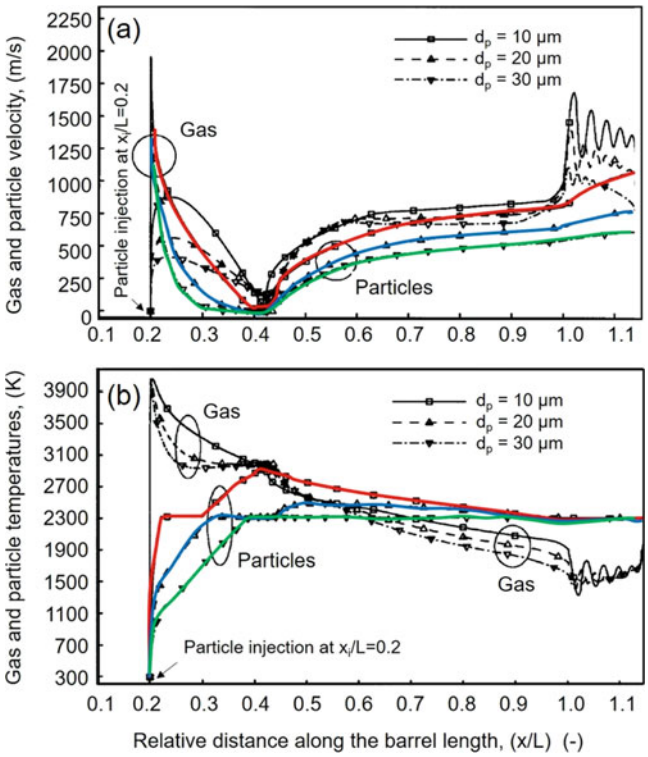

Fig. 7.56 (**a**) Particle velocity and gas velocity in its location, as function of distance along the barrel length, (**b**) Particle temperature and gas temperature at its location as function of distance long the barrel length. Alumina particles in an $O_2/C_2H_2/N_2$ (40 vol.%) axial loading distance $x_i/L = 0.2$ and radial loading distance $y_i/r = 0.05$, L = 1.0 m, d_i = 25 mm and SoD = $6d_i$ [Ramadan et al. (2004)]. (Reprinted with kind permission from Springer Science Business Media, copyright © ASM International)

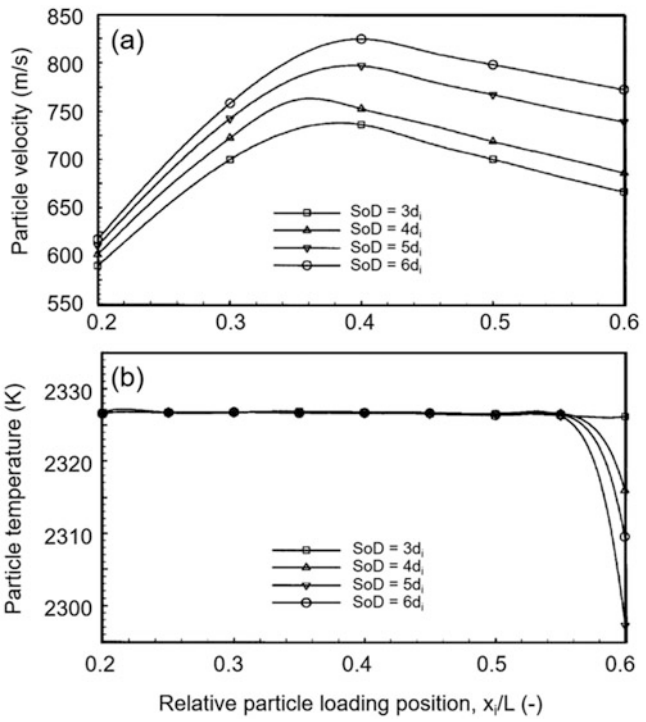

Fig. 7.57 (**a**) Alumina particle velocity and (**b**) temperature prior to their impact on the substrate as function of the relative loading position, for different Stand-off Distance (SoD). d_i = 25 mm, L = 1.0 m [Ramadan et al. (2004)]. (Reprinted with kind permission from Springer Science Business Media, copyright © ASM International)

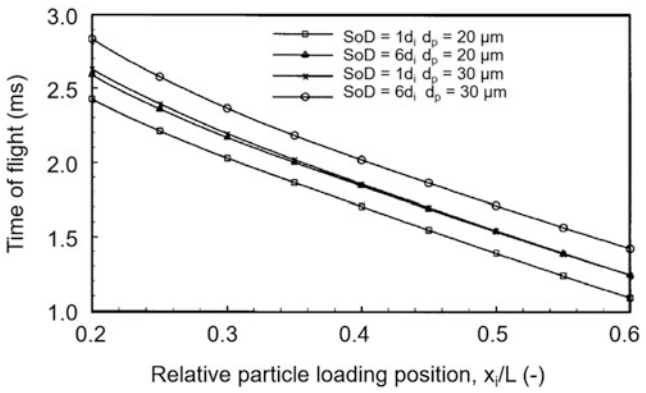

Fig. 7.58 Time of flight for alumina particles as a function of the relative particle loading position, particle diameter, and Stand-off Distance (SoD). d_i = 25 mm, L = 1.0 m [Ramadan et al. (2004)]. (Reprinted with kind permission from Springer Science Business Media, copyright © ASM International)

gas expanded freely with negligible shock reflection effects. Figures 7.56a and b present the dependencies of solid particle velocities and temperatures on their axial location, x, as well as the gas velocities and temperatures at the particle location. In this calculation, the initial loading location is $x_i/L = 0.2$ and L = 1 m (injection position far from optimal). Hot gases also heat particles to high temperatures that can reach the melting point, depending on their sizes (Fig. 7.51b) and injection location (not represented here).

Ramadan et al. (2004) pointed out that the geometrical configuration of the detonation gun, the particle size of the powder feed, the loading locations, and the SoD were important parameters in determining the properties of the end product. In general, increasing the standoff distance resulted in an increase in velocity and a decrease in temperature of the particles at impact on the target surface. Increasing the stand-off distance also resulted in less uniform properties of the coating layer, where the properties of the coating layer were dependent on the particle characteristics upon impact on the target surface. As shown in Fig. 7.57, the particle velocity on impact on the substrate is strongly dependent on the particle axial loading location and the SoD. The effect is less pronounced on the particle temperature prior to its impact on the substrate. The time of flight of the particles from imitation of the detonation to their impact on the substrate is given in Fig. 7.58. As expected, the results are relatively sensitive to the particle diameter and the stand-off distance (SD), and inversely proportional to the relative particle loading position. It is to be noted that these results were obtained

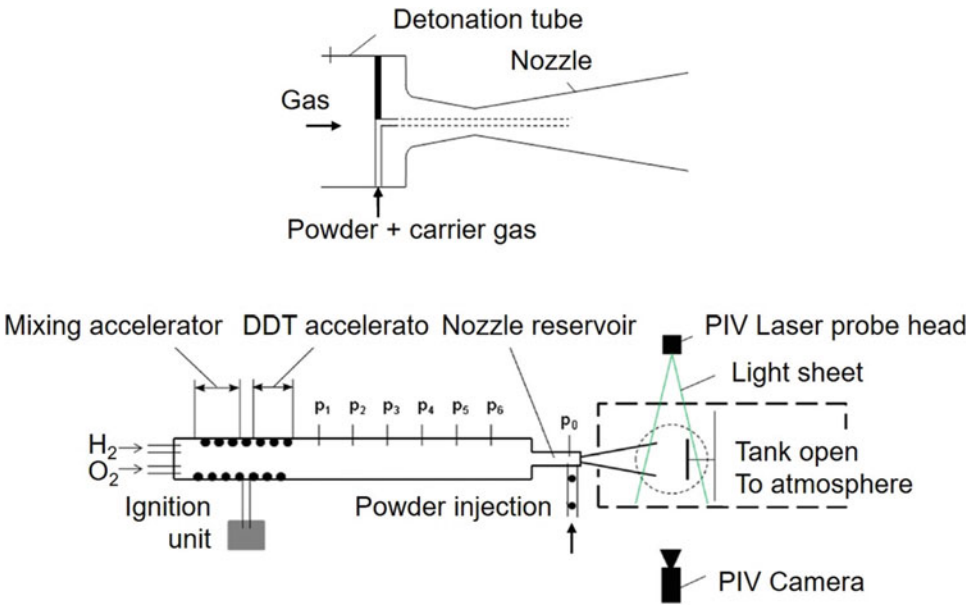

Fig. 7.59 Modified D-Gun test rig with convergent-divergent nozzle extension. [Henkes et al. (2014)]

for a barrel length L = 1 m. Operation with a longer or shorter barrel length has a significant influence on the reported data.

An interesting development reported by Henkes et al. (2014) describes a modified detonation gun through the addition of a convergent-divergent nozzle that allowed for a significant increase of the particle projection velocity over 1200 m/s, leading to improved coating qualities. The device, schematically represented in Fig. 7.59, could be operated either as a conventional D-gun in which the powder is accelerated in a blast wave, or as an intermittent shock tunnel process in which the particles are accelerated in a high-enthalpy nozzle flow with high reservoir conditions. Experimental data and modeling results are presented for the spraying of WC-Co (88/12), NiCr (80/20), Al_2O_3, and Cu using different substrate/powder combinations.

7.4.3 Coating Formation

As mentioned earlier, thermal spray coating using the pulse detonation thermal spray (PDTS) or D-gun technology is based on the cyclic projection of the material to be deposited in the form of small charges of fine powders each of a mass less than 1 g at frequencies up to 10 to 15 Hz. The technology relies heavily on the in-flight heating and acceleration of particles to be sprayed to temperatures near their melting point and velocities of the order of 1000 m/s, projecting them toward the substrate in essentially a softened solid state where they deform on impact forming a high-density well-bonded coating. The rate of coating deposition, $\dot{m}_d$, can be simply calculated as:

$$\dot{m}_d = \eta_d f\, m_c \tag{7.13}$$

where;

η_d deposition efficiency
f detonation frequency
m_c powder charge per detonation cycle

It is to be noted that the mass of powder charge used per shot has to be carefully controlled. In principle, it should be less than 10–20% of the mass of the combustion gas products, which provides the particles with the necessary heat and mechanical energy to raise their temperature and accelerates and projects the individual powder particles onto the substrate. The coating produced by each individual shot should mainly consist of individual particles distributed uniformly over the surface of the substrate. If the powder charge is too high, a continuous film is formed in a single shot, which on cooling will develop cracks in the film, which weakens it and induces a certain level of porosity [Nikolaev et al. (2003)].

With a typical charge of 0.2 g of powder per shot, operating at a frequency of 5 Hz, a deposition rate of around 60 g/min (3.6 kg/h) can be expected depending on the deposition efficiency, η_d. The latter depends, in turn, on the properties of the material deposition, the substrate preparation, and the operating parameters including the stand-off distance (SoD) between the end of the spray gun and the substrate. Normally with D-gun technology, deposition efficiencies close to 100% can be attained with the diameter

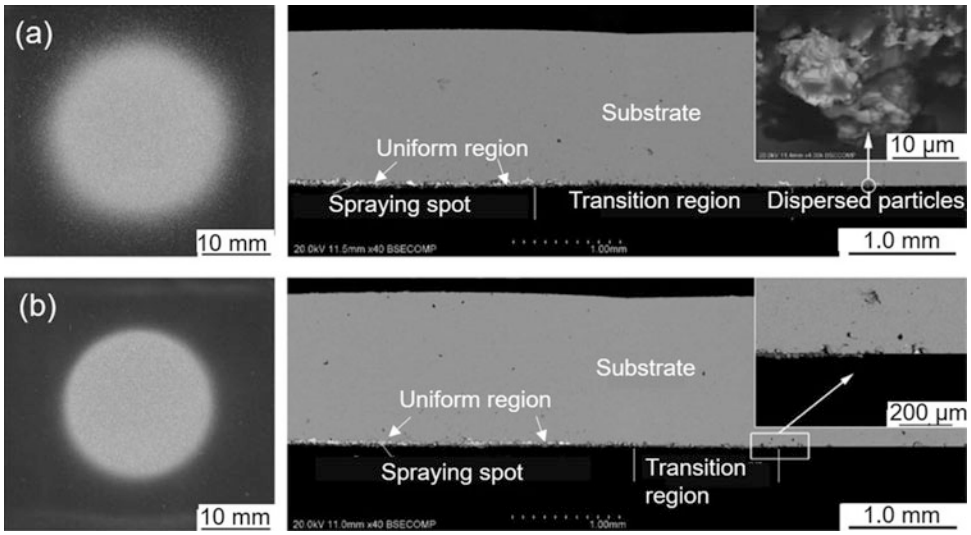

Fig. 7.60 Image of a "sweet spot" and cross-section microstructure for a single shot of WC-Co powder on polished stainless-steel substrate using modified D-gun (**a**) without separator mask (**b**) with separator mask [Wang et al. (2009)]

of the deposit "sweet spot" created by a single shot equal to the inner diameter of the gun barrel.

Wang et al. (2009) reported, however, that in certain cases, the sprayed powder from a D-gun can show an undesirable lateral dispersion as it exit the gun barrel at high speed, giving rise to a lower-quality deposit in the outer fringes of the deposited sweet spot. The study was carried out for the spraying of WC-Co (12wt.%Co) powder with a particle diameter in the 30–60 µm range on a stainless-steel substrate, which was grit blasted to a roughness, R_a, close to 7 µm. The spray gun had a 1.25 m long barrel, with a powder loading distance of 0.5 m from the discharge end of the barrel and an SoD of 110 mm (corresponding to 5.5 d_i, for a barrel i.d. of 20 mm). The combustion mixture was oxygen/acetylene with an O_2/C_2H_2 volume ratio of 1.06. The gun was operated at a detonation frequency of 4 shots/s, and a powder feed rate of 1.0–1.4 g/s (corresponding to a single powder charge of 0.25–0.35 g/shot). Typical results are given in the upper part of Fig. 7.60a, which shows on its LHS an image of the deposited "sweet spot" from a single shot, which has a central core with a diameter of about 23 mm and a halo of scattered particles with an outer diameter of 27 mm. Details of the microstructure of the deposit are given in the RHS of the same figure. This shows the central region with a uniform distribution of the deposited particles and a gradual transition to a region covered with dispersed particles in its fringes.

In an attempt to get rid of this particle-dispersed region surrounding the core of the deposit, Wang et al. (2009) designed and executed a separator mask, which they attached to the original D-gun, as shown in Fig. 7.61. The mask, which was placed at a distance of about 100 mm from the end of the gun barrel, had a circular opening of the same diameter as the barrel internal diameter (estimated 20 mm) coaxial with the gun barrel. The outer diameter of the separator mask was 5x the diameter of the opening (i.e., 100 mm). Spraying experiments carried out with the separator mask using the same powder and gun operating parameters gave rise to a significantly better-defined deposition spot, as shown on LHS of Fig. 7.60*b*. The halo around the deposited spot formed by the dispersed particles observed earlier in Fig. 7.60a was completely eliminated, giving rise to a superior-quality coating.

Comparing WC-Co coatings with the separation mask to those without mask, Wang et al. (2009) reported that the surface roughness S_a and R_a, the porosity, and the wear rate of the coating decreased respectively by 77%, 41%, 40%, and 20%, while the Vickers microhardness HV, the Knoop microhardness in both directions (parallel and orthogonal to the coating) $HKcs_{\perp}$, $HKcs_{\parallel}$, the elastic modulus $Ecs_{\perp}$, $Ecs_{\parallel}$, and the adhesive strength increased respectively by 12%, 13%, 13%, 32%, 36%, and 16%. They also pointed out that the weight of the coating received on the substrate in the presence of the separator mask was 12% less than that of the coating without the mask. Such a drop of deposition efficiency to 88% of the powder consumed in the process gave rise to a corresponding increase of the cost of the coating, which has to be evaluated against the improved properties and performance of the coating. Considering that the fringe powders would be intercepted by the separator mask, attention has to be given in such a setup to the periodic replacement of the mask for cleaning and recycling if possible.

Considering that operating parameters can be modified between successive shots of the detonation gun, the "shot control method" offers an excellent advantage for co-spraying of metal and ceramic powders with their optimum spraying parameters. Basically, only one type of

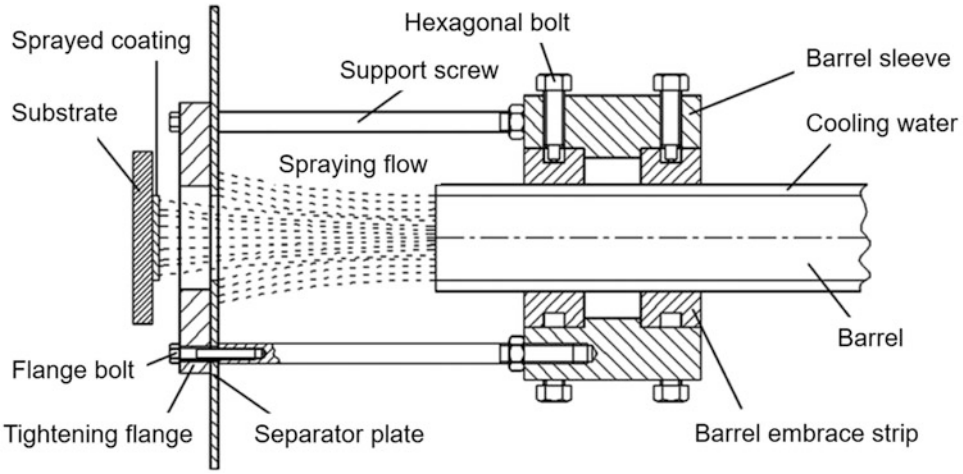

Fig. 7.61 Schematic of separation mask attachment used in D-gun spraying system [Wang et al. (2009)]

powder is deposited per individual shot to produce a coating mixture of ceramics and metals [Kim et al. (2003)]. Graded coatings with a compositional gradient through thickness could thus be produced by spraying several coating layers with increasing ratios of ceramic to metal shots in a sequence, as shown in Fig. 7.62. Other methods for the spraying of graded coatings, such as the mixed powder methods, are difficult to execute and optimize due to the important differences in the respective spraying parameters used for ceramics and metals.

According to Cannon et al. (2008), the particle size distribution of the feed powder has a significant impact on the coating properties. A decrease in powder size reduces roughness and porosity in the case of NiCr and Al_2O_3 but has a marginal effect for WC-Co due to the flow of the softer binder (Co) phases, especially when a coarser particle size is utilized. The toughness of the Al_2O_3 and WC-Co coatings are dependent on the presence respectively of W_2C in WC-Co, and α –Al_2O_3 in alumina ones. The wear resistance is only marginally affected by the powder size for WC-Co coatings, in contrast to Al_2O_3 coatings where it is very sensitive to the particle size distribution. Finally, the authors [Cannon et al. (2008)] conclude that commercial powders with size distributions of 10–44 μm can be used.

To summarize, the design of a D-gun with all its devices is not simple. Kharlamov (2004) summarized all the issues to ensure rapid development of a detonation wave within a short cycle time. With high impact velocities, and temperatures, which can be controlled in the range 0.9 T_m to T_m, T_m being the melting temperature, very dense coatings can be obtained. D-gun spraying usually produces denser coatings than any other thermal spray technique.

7.4.4 Coating Properties

The most important and well-developed applications of the D-gun are the deposition of wear-resistant, thermo-barrier, electro-insulating, and high-temperature oxidation-resistant coatings.

7.4.4.1 Plain Fatigue and Fretting Fatigue

Cu-Ni-In coatings were used to test the improvement in plain fatigue and fretting fatigue of an Al-Mg-Si alloy substrate [Rajasekaran et al. (2011)]. Coatings 40 μm thick were found to give the best result. The same Cu-Ni-In coatings deposited on Ti alloys were beneficial. The detrimental effect of life reduction due to fretting was relatively larger in the Al-alloy substrate compared to the Ti-alloy one. This result was explained in terms of differences in the values of surface hardness, surface roughness, surface residual stress, and friction stress [Ganesh Sundara Raman et al. (2007)]. Cu–Ni–In powder was deposited on Ti–6Al–4 V fatigue test samples using plasma spray and detonation gun (D-gun) spray processes [Rajasekaran et al. (2008)]. The D-gun sprayed coating was dense with lower porosity compared with the plasma-sprayed coating. The hardness value of the D-gun sprayed coating was higher than that of the plasma-sprayed coating and of the substrate because of its higher density and cohesive strength. Coating surfaces were very rough in both coatings. While the D-gun sprayed coating had higher compressive residual stresses, the plasma-sprayed coating exhibited lower values of compressive residual stress and even tensile residual stress. The higher surface hardness and higher compressive residual stress of the D-gun sprayed specimens were responsible for their superior fretting fatigue lives compared with the plasma-sprayed specimens [Rajasekaran et al. (2008)].

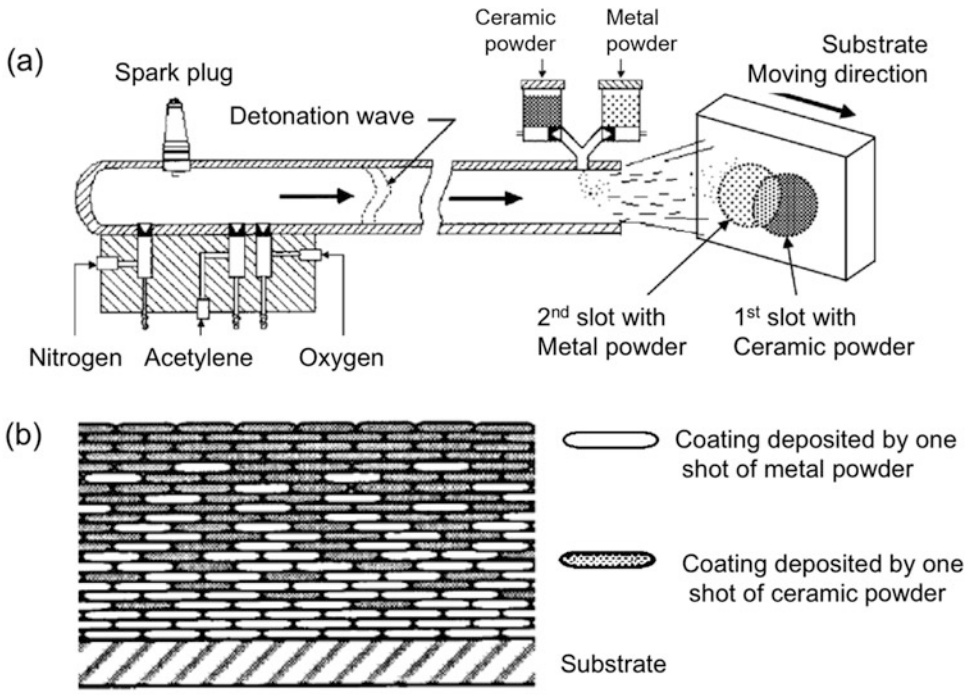

Fig. 7.62 Schematic showing the deposition scheme to produce, graded coatings using the "shot control method" (**a**) D-gun with one radial injection port and two powder feeders, (**b**) typical microstructure of a graded coating [Kim et al. (2003)]. (Reprinted with kind permission from Elsevier)

7.4.4.2 Oxidation Resistant Coatings

In the initial oxidation process of eutectic (β - NiAl + γ-Re) coatings, rhenium partially evaporates in the form of volatile oxides. Instead of rhenium oxides, a protective alumina layer forms on the coating surface. The oxidation process is reduced as Al_2O_3 is formed. It has been established that the air oxidation resistance of eutectic (β-NiAl + γ-Re) alloy coatings substantially increases at 800 to 1100 °C as compared with single-phase NiAl intermetallic coatings. The ratio of alumina and nickel formation rates is the key factor for the oxidation of these coatings. The scale formed on the single-phase NiAl intermetallic coating consists of a Al_2O_3 monolayer with spinel inclusions, while a two-layer protective scale forms on the eutectic (β-NiAl + γ-Re) alloy coating: spinel external layer and alumina internal layer, which has a better resistance to oxidation up to 1100 °C [Oliker et al. (2007)1 and 2].

7.4.4.3 Thermal Barrier Coatings (TBCs)

(i) TBC's bond coat

For thermal barrier bond coats, Ti-Al-Cr [Oliker et al. (2007)2] and MCrAlY [Yuan et al. (2008), Belzunce et al. (2002), Zhang et al. (2002), Taylor and Knapp (1995), Zhang et al. (2003)] coatings were tested. The behavior of TiAlCr depends on the substrate structure, which determines the nature of diffusion. NiCrAlY coatings displayed very favorable oxidation resistance; the aluminum layer formed was intact for over 300 h at 1050 °C. NiCrAlY coatings sprayed using a D-gun and LPPS showed a splat layer structure in the as-sprayed state [Zhang et al. (2003)2]. The difference is that an oxidation reaction took place during D-gun spraying and Al_2O_3 distributed on the splat boundaries of as-sprayed D-gun NiCrAlY coatings. Isothermally oxidized at 1050 °C for 300 h, both coatings showed favorable oxidation resistance and an Al_2O_3 scale was formed on their surface, although the oxidation resistance of D-gun NiCrAlY coatings was inferior to that of LPPS NiCrAlY coatings. D-gun NiCrAlY coatings have higher surface hardness. D-gun NiCrAlY coatings should be considered at first when the working conditions are in the high dynamic load or low oxidizing air range [Zhang et al. (2002)]. HVOF and D-gun techniques were employed to deposit the Ni–25Cr–5Al–0.5Y bond coat (BC) of a thermal barrier coating with the YSZ topcoat detonation-sprayed using hollow spherical YSZ powder [Yuan et al. (2008)]. The oxidation rate of the TBC system at 1100 °C is two times lower with the HVOF-sprayed NiCrAlY (see Fig. 7.41b) than with the D-gun sprayed one (see Fig. 7.63), with both processes using the same NiCrAlY powder. A significant number of Cr_2O_3 and $NiCr_2O_4$ oxide nodules can be formed on top of the D-gun NiCrAlY coating after 10 h oxidation at 1100 °C, while more α-Al_2O_3 is present for the HVOF sprayed coating. The coarse surface

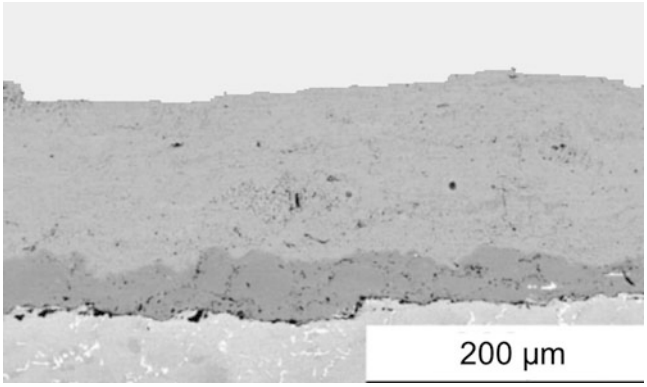

Fig. 7.63 Cross-sections of detonation-sprayed TBCs using YSZ fused and crushed powder for the topcoat and NiCrAlY for the bond-coat [Yuan et al. (2008)] (Reprinted with kind permission from Elsevier)

roughness in the case of the D-gun bond coat ($R_a = 6.61$ µm against 5.38 µm for the HVOF bond coat) and the higher porosity (7.8% for the D-gun BC against 3.2% for the HVOF BC) have a detrimental effect on the oxidation behavior of the TBC system. The fine α-Al_2O_3 dispersion formed during HVOF spraying exerts a beneficial effect on the oxidation resistance of the HVOF NiCrAlY coatings by serving as initial alumina nuclei and promoting the development of a protective TGO scale [Yuan et al. (2008)].

(ii) TBC's ceramic layer

Yttria partially stabilized zirconia was D-gun sprayed on a Ni-base superalloy, M38G [Ke et al. (2005)]. The D-gun-sprayed TBC had a very low thermal conductivity of 1.0–1.4 W/m K, close to that of the plasma-sprayed YSZ coatings and much lower than their EB-PVD counterparts. The TBCs exhibited excellent resistance to thermal shock up to 400 cycles of 1050 °C to room temperature (forced air cooling) and 200 cycles of 1100 °C to room temperature (forced water quenching). As cycles proceeded, the development of Ni/Co rich TGO and t-to-m transformation within the ceramic coat could account for eventual spallation [Zhang et al. (2002)]. Similar results were obtained through optimizing the spray parameters (especially the ratio of C_2H_2 to O_2) [Wu et al. (2003)]. The oxidation behaviors at 1000 and 1100 °C were studied. TBCs detonation sprayed were uniform and dense, with a few micro-cracks in the ceramic coats and a rough surface of bond coats. At the high temperature, the dense detonation-sprayed ceramic coats with low porosity could obviously decrease the diffusive channels for oxygen and reduce the oxygen pressure (P_{O_2}) at the ceramic-bond coat interface [Wu et al. (2004)]. NiCrAlY/YPSZ and NiCrAlY/NiAl/YPSZ thermal barrier coatings (TBCs) were also successfully deposited by detonation spraying [Ke et al. (2005)]. TBCs included a uniform ceramic coat containing a few microcracks and a bond coat with a rough surface. Results were similar to those previously discussed. *Figure* 7.64 from [Yuan et al. (2008)] presents a fractured YSZ TBC's topcoat obtained by D-gun (acetylene-oxygen [Suresh Babu et al. (2008)]) sprayed hollow sphere particles 10–75 µm in diameter. The microstructure of the topcoat is similar to APS ones with regard to the lamellar microstructure (Fig. 7.64-*A*). It means that it was built up by layering individual splats resulting from impacting melted or semi-molten particles. The large, equiaxed voids are probably due to particles that did not fully melt (Fig. 7.64-*B*). Splat are approximately 3–6 µm thick and hundreds of micrometers in diameter. The thermal conductivity is similar to that obtained with APS coatings.

(iii) Graded coatings

Functionally graded thermal barrier coatings (FGM TBC) have been deposited by the D-gun spray process according to the "shot-control method" [Ramadan and Butler (2004)]. The gradient ranged from 100% NiCrAlY metal on the substrate to 100% ZrO2–8 wt.% Y_2O_3 ceramic for the topcoat and consisted of a finely mixed microstructure of metals and ceramics with no obvious interfaces between the layers.

7.4.4.4 Wear Resistant Coatings

The hardness of coatings is conventionally used as the primary correlating parameter for evaluating wear resistance [Wu et al. (2003)]. Authors have studied large varieties of coatings (WC-Co, TiMo(CN), TiN-CoN, Al_2O_3, Al_2O_3-TiO_2 with different size distributions and obtained by different manufacturing processes deposited with the D-gun process with a range of process parameters for each coating. Coatings were characterized in terms of phase content and distribution, porosity, micro hardness, and evaluated for erosion, abrasion, and sliding wear resistance. Results [Sundararajan et al. (2005)] show that tribological properties of the coatings are more strongly influenced by the coating process parameters themselves rather than microstructural parameters like phase content and distribution, and porosity.

(i) WC-Co

Suresh et al. (2008) have shown that the microstructure, in terms of nature/extent of decomposition of WC, as well as properties of WC–12 wt.% Co coatings, is critically dependent on the variations of the oxygen–fuel ratio. Murthy et al. [5.196] have studied WC–10Co–4Cr and Cr_3C_2–20(NiCr) coatings deposited by HVOF and D-gun processes. The abrasion tests were done using a three-body solid particle rubber wheel test rig using silica grits as the abrasive medium. The D-gun coating performed slightly better than the HVOF one possibly due to the higher residual

compressive stresses of the former, and the WC-based coating had higher wear resistance compared to the Cr_3C_2-based coating. Also, the thermally sprayed carbide-based coatings have excellent wear resistance with respect to the hard chrome coatings [Murthy et al. (2006)]. Wang et al. (2010) have emphasized that the compressive stress of WC-Co coatings (peening effect of high spraying velocity and kinetic energy during the D-gun process) could significantly improve the coating properties, whereas the tensile stress impaired the coating properties. Park et al. (2007) have sprayed WC–12 wt. % Co, commercial feedstock, with carbide grain size of approximately 100–200 nm. Post-heat treatment of WC-Co coatings modified their resistance because microhardness increased, while fracture toughness and wear resistance increased by increasing the temperature to 800 °C, but decreased after heat treatment at 900 °C. The amorphous phase disappeared and other carbide phases such as W_3Co_3C and W_6Co_6C formed during heat treatment above 700 °C. The improved properties were attributed to microstructural changes. Du et al. (2005) have studied the influence of process variables on the qualities of D-gun-sprayed WC–Co coatings. Suresh Babu et al. (2007) have shown that the feedstock size influences the phase composition and porosity of WC-Co coatings, imparting variations in the coating hardness, fracture toughness, and wear properties. The fine and narrow size range WC-Co coating exhibited superior wear resistance. Oliker et al. (2004) have also shown that powder structure is important. The use of powders with highly porous particles results in the formation of porous coatings with low wear resistance. Du et al. (2006) have studied the fabrication and evaluation of D-gun-sprayed WC–Co coating with self-lubricating property.

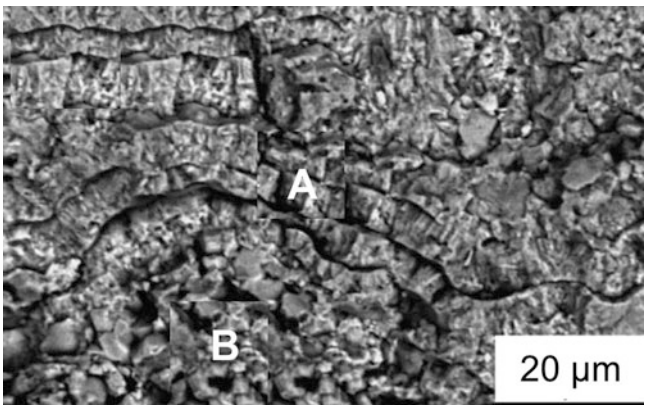

Fig. 7.64 Fractured YSZ topcoat obtained by D-gun spraying (acetylene/oxygen mixture) hollow sphere particles 10–75 μm in diameter (as-sprayed state) [Yuan et al. (2008)]. (Reprinted with kind permission from Elsevier)

Murthy et al. (2006) have studied WC-10Co-4Cr and Cr3C2–20(NiCr) coatings, deposited by HVOF and D-gun processes, and low stress abrasion wear resistance of these coatings have been compared. *Figure* 7.64 from Murthy et al. (2001) presents SEM micrographs of transverse section of WC-10Co-4Cr coatings HVOF and D-gun sprayed. The DJ-2600 HVOF gun was working with H_2 (3.6 m^3/h), O_2 (1.8 m^3/h), and air (1.2 m^3/h), while the D-gun used O_2/C_2H_2 (1/1.23 volume ratio) and the powder size was between 11 and 53 μm. Figure 7.65 shows that the D-gun coating is slightly denser than the HVOF one, as confirmed by a porosity of 1.3% against 1.6%. Correlatively, the microhardness ($HV_{0.3}$) is 792 for the HVOL coating against 849 for the D-gun one. Micrographs of traverse sections of as-sprayed WC-10Co-4Cr HVOF and D-gun coatings are given in Fig. 7.65a and b, respectively, showing in both cases damage indued by surface grinding. Coatings were ground with a diamond resin bonded wheel to achieve a final surface roughness of $R_a < 0.2$ μm. The grinding induced surface damage in both the cases, as shown in Fig. 7.65a and b. The

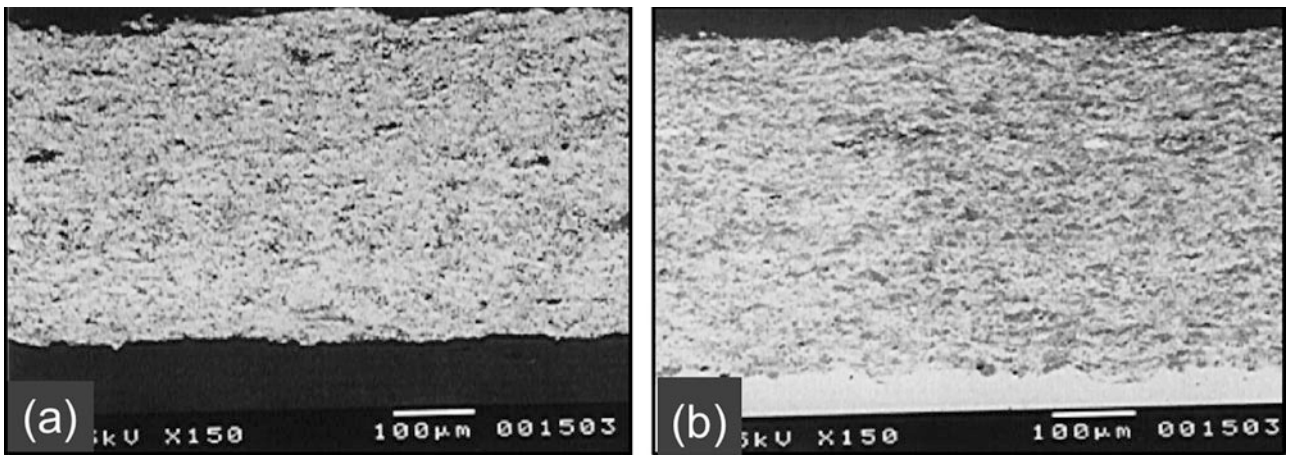

Fig. 7.65 SEM micrographs of transverse section of WC-10Co-4Cr coating in as-sprayed condition: (**a**) HVOF coating; (**b**) D-gun sprayed coating [Murthy et al. (2001)]. (Reprinted with kind permission from Elsevier)

microstructure of the HVOF coating developed numerous cracks beneath the surface up to a depth of 150–200 μm. However, such cracks were minimum in the case of D-gun-sprayed samples (Fig. 7.65b). The erosion resistance of the D-gun coating was found to be higher compared to that of the HVOF coating in the as-coated condition. This is possibly due to the slightly higher microhardness, lower porosity, and possibly higher residual compressive stresses of the DS coating [Murthy et al. (2001)].

Usually results show that the D-gun coatings perform slightly better than the HVOF coatings possibly due to the higher residual compressive stresses induced by the former process, and WC-based coatings have higher wear resistance in comparison to Cr_3C_2-based coating. Also, the thermally sprayed carbide-based coatings have excellent wear resistance with respect to the hard chrome coatings.

Du et al. (2006) deposited by the detonation gun (D-gun) process a WC–Co coating with self-lubricating property, using a commercial WC–Co powder doped with a MoS_2–Ni powder, under a proper spray condition. The results indicate that the MoS_2 content was maintained, if not slightly increased, in the coating which was attributed to the protection offered by the nickel coating of the MoS_2 doping material in the feed powder. Evaluation on sliding wear property indicates that the MoS_2 composition plays an important role in lowering both coefficient of friction and wear rate for the resulting coating, which is confirmed by observations on wear track, as well as X-ray photoelectron spectroscope (XPS) results on worn surface. It suggests that the deposition of a WC–Co coating with self-lubricating property by D-gun spray is feasible by controlling lubricant powder and spray conditions, which can exhibit higher sliding wear resistance. To analyze the improved sliding wear property of the WC–Co coating containing MoS_2 composition, worn surface after tests were observed and compared with that of the pure one, as shown in Fig. 7.66.

It is apparent that the groove is shallower for the WC–Co coating with MoS_2 composition. It is supposed that the wear particles produced in the sliding process are comprised of WC, Co, MoS_2, and Ni or some of them, which underwent crushing, compaction, and smearing at the contact area between tested material/counter body, leading to the diminution of their size, due to the developed shear stresses.

(ii) Alumina

The structure of D-gun-sprayed Al_2O_3 coatings was investigated by Li and Ohmori (1996) using a copper electroplating technique with a typical layer structure with poor bonding at interfaces between flattened particles. The mean bonding ratio of the bonded interface to total apparent bonding interface area was about 10%. However, a high particle velocity may result in a rough surface for individual flattened particles, which is effective for better interlocking of flattened particles. The good wear resistance might be mainly due to the mechanical interlocking effect between flattened particles. As for WC-Co, the feedstock size was also found to influence the phase composition of Al_2O_3. The course ($d_{50} = 18$ μm) and narrow ($d_{50} = 10$ μm) size distribution Al_2O_3 coating exhibited better performance under abrasion and sliding wear modes; however, under erosion wear mode, the as-received Al_2O_3 ($d_{50} = 14$ μm) coating exhibited better performance. Saravanan et al. (2000) have conducted a Taguchi-full factorial (L16) design parametric study to optimize the D-gun spray process parameters. For hardness, the significant factors of influence were spray distance, carrier gas flow rate, and fuel-to-O_2 ratio selected, in that order. They showed that alumina coatings of the highest hardness 1363 H and the lowest porosity 1.45% could be obtained for specific spray parameters. Other authors have also sprayed alumina coatings [Niemi et al. (1994), Saravanan et al. (2000), Pogrebnyak et al. (2000), Sobiecki et al. (2004)].

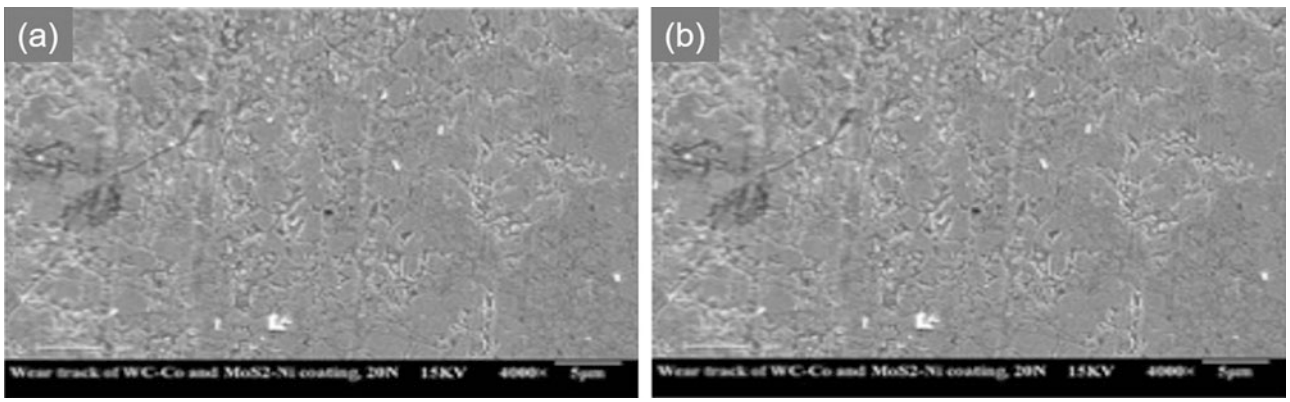

Fig. 7.66 SEM morphologies of wear surface of the WC–Co coatings against WC–Co ball under normal load of 20 N; (**a**) pure WC–Co coating, (**b**) WC–Co coating containing MoS_2 composition [Du et al. (2006)]

(iii) Alumina-titania

D-gun-sprayed coatings of Al_2O_3-TiO_2 [Venkataraman et al. (2006)] (13 wt.%), with a particle size of 22–45 μm, have low porosity, high density, hardness above 1000 $HV_{0.5}$, and, at the same time, considerably improved frictional wear resistance compared to that of the AISI-1045 steel substrate. A preliminary preparation of the substrate surface by compressed air-enhanced grit blasting is necessary for the coating to adhere well to the substrate. Venkataraman et al. (2006) have studied the phases present in D-gun-sprayed Al_2O_3-TiO_2 (13 wt%) and compared them to those obtained with plasma spraying. Semenov and Cetegen (2002) have studied D-gun spraying of nano-structured alumina–titania (12 wt.%) coatings, starting from commercial agglomerated nanostructured particles. XRD spectrum peaks of α-Al_2O_3 (113) and γ-Al_2O_3 (400) for the feedstock powder allowed for determining the fraction of melted powder. Coating obtained by D-gus spraying contained a smaller concentration of α-Al_2O_3 phase compared to that of γ-Al_2O_3 which is an indication of limited melting of the powder prior to their deposition on the substrate. It also suggests that the technology could be successfully employed for the deposition of nanostructured alumina–titania coatings. These findings combined suggest that the detonation deposition process could be successfully employed in the deposition of nanostructured alumina–titania coatings.

Coatings exhibited lower erosion wear resistance than bulk alumina but better resistance to abrasion wear, especially Al_2O_3 + 3 wt % TiO_2 and Al_2O_3 + 40 wt % ZrO_2. Compared to alumina coatings that are plasma sprayed and contain up to 98% of γ-alumina, D-gun coatings have γ-alumina phase content of less than 60%, and about 30% of α-alumina phase content, the balance being β- and δ-alumina phases [Semenov and Cetegen (2002)].

Bhandari et al. (2012) investigated the slurry erosion performance of detonation gun (D-gun) spraying ceramic coatings (Al_2O_3 and Al_2O_3-$13TiO_2$) on CF8M steel. The slurry collected from an actual hydro power plant was used as the abrasive media in a high-speed erosion test rig. An attempt has been made to study the effect of concentration (ppm), average particle size, and rotational speed on the slurry erosion behavior of these ceramic-coated steels under different experimental conditions. The analysis of eroded samples was done using SEM, XRD, and stylus profilometry. The slurry erosion performance of the D-gun spray Al_2O_3-$13TiO_2$-coated steel has been found to be superior to that of Al_2O_3-coated steel. Both the coatings showed brittle fracture mechanism y of material removal during the slurry erosion exposure. During the slurry erosion of Al_2O_3-coated steels, slurry concentration and average particle size were found to be relatively more dominant factors in comparison with rotational speed. On the other hand, in the case of Al_2O_3-$13TiO_2$-coated steel y, rotational speed was found to be more dominant in comparison with slurry concentration and average particle size. Thus, D-gun-sprayed Al_2O_3-$13TiO_2$ coatings can be used in low-speed hydro turbines with high concentration slurries of large particles. Fatigue and brittle failure were found to be dominating material removal mechanism in the Al_2O_3-$13TiO_2$ coating whereas the Al_2O_3 coating showed brittle behavior mechanism of material removal. Under stated experimental conditions, there was no chemical effect of the used slurry on the coatings.

(iv) Tribological coatings

Sundararajan et al. (2010) have studied the tribological performance of 200 μm thick TiMo(CN)-28Co and TiMo (CN)–36NiCo coatings obtained using a D-gun. Powders were prepared by SHS and had the following characteristics: TiMo(CN)-36NiCo, d_{50} = 36.4 μm irregular and blocky shaped, phases being $TiC_{0.7}N_{0.3}$, Co, Ni, and TiMo(CN)-28Co, d_{50} = 23.3 μm, irregular shaped, phases being $TiC_{0.7}N_{0.3}$, Co. In both coatings, the best tribological performance and the lowest porosity were obtained at intermediate oxygen/acetylene ratios. When comparing the tribological performance of the optimized TiMo(CN) type coatings with that of optimized WC-Co ones, the abrasion resistance is comparable. However, the erosion and sliding wear resistance of TiMo(CN) type coatings were considerably lower than those of the WC-Co coatings. Du et al. (2007) have deposited WC-Co/MoS_2–Ni coatings by D-gun, using a commercial WC-Co powder and a MoS_2-Ni powder, with the spray condition being adapted to both powders. The MoS_2 composition was kept and distributed homogeneously. Coatings had self-lubricating properties. MoS_2 lowered the wear rate under dry sliding conditions when its content was lower than 4.9 wt.%.

(v) Corrosion and wear-resistant coatings

Cr_3C_2 (75 wt %)-NiCr D-gun-sprayed coatings on high-temperature structure steel DIN 12CrMo44 [Wang et al. (2000)] were dense with good bonding to substrate as well as high resistance to high-temperature oxidation and wear. Reports from the in-service test at Bao Shan Steel Company indicate that such coatings have at least doubled the roll life. Cr_3C_2–NiCr cermet coatings were deposited on two Ni-based superalloys, namely Superni 75 and Superni 718, and one Fe-based superalloy Superfer 800H by the D-gun thermal spray process [Sundararajan et al. (2010)]. The cyclical hot-corrosion studies were conducted on uncoated as well as D-gun-coated superalloys in the presence of a mixture of 75 wt.% Na_2SO_4 + 25 wt.% K_2SO_4 film at 900 °C for 100 cycles. It was observed that the Cr_3C_2–NiCr-coated superalloy showed better hot-corrosion resistance than the

uncoated superalloys, as a result of the formation of continuous and protective oxides of chromium, nickel, and their spinel. Cr_3C_2–NiCr coatings were D-gun sprayed on Superni 75, Superni 718, and Superfer 800H superalloys [Kamal et al. (2008)]. Coatings exhibited nearly uniform, adherent, and dense microstructures with porosity less than 0.8%. These coatings were found to be very effective in decreasing the corrosion rate in a molten salt environment (Na_2SO_4–60% V_2O_5) at a high temperature of 900 °C for 100 cycles. Particularly, the coating deposited on Superfer 800H showed better hot corrosion protection as compared to Superni 75 and Superni 718. The cyclical oxidation behavior of the same coatings on the same superalloy at 900 °C for 100 cycles in air under cyclic heating and cooling conditions has been investigated [Kamal et al. (2009)]. Among all the coated superalloys, chromium, iron, silicon, and titanium were oxidized in the inter-splat region, whereas splats that consisted mainly of Ni remained un-oxidized. The parabolic rate constants of Cr_3C_2-NiCr-coated alloys were lower than those of the bare superalloy. The cyclical oxidation behavior of the same coatings on the same superalloy at 900 °C for 100 cycles in air under cyclic heating and cooling conditions has been investigated [Kamal et al. (2009)]. Among all the coated superalloys, chromium, iron, silicon, and titanium were oxidized in the inter-splat region, whereas splats, which consisted mainly of Ni remained un-oxidized. The parabolic oxidation rate of Cr_3C_2-NiCr-coated alloys were lower than those of the bare superalloys. To prolong the life of steel slab continuous casting rolls, Cr_3C_2-NiCr D-gun spray coatings were processed on the roll surface (DIN 12CrMo44) in a steelmaking plant in China [Wang et al. (2002)]. The wear resistance of the coated samples reduced the risk of seizure compared to uncoated samples, at room and elevated temperatures with any load and sliding velocity. It must also be emphasized that Cr_3C_2–20(NiCr) coatings have excellent wear resistance [Murthy et al. (2006), Wang et al. (2002)], however lower than those of the WC-Co ones. When they are exposed to high temperatures (over 600 °C), their corrosion resistance is improved [Wang et al. (2002b), Murthy et al. (2007)].

Kamal et al. (2011) investigated rare earth oxide (CeO_2) incorporated in the NiCrAlY alloy and the hot corrosion resistance of detonation-gun-sprayed NiCrAlY +0.4 wt.% CeO_2 coatings on superalloys, namely, superni 75, superni 718, and superfer 800H in molten 40% Na_2SO_4–60% V_2O_5 salt environment at 900 °C for 100 cycles. The coatings exhibited a characteristic splat globular dendritic structure with diameters similar to those of the original powder particles. The weight change technique was used to establish corrosion kinetics. X-ray diffraction (XRD), field emission scanning electron microscopy/energy-dispersive analysis (FE-SEM/EDAX), and X-ray mapping techniques were used to analyze the corrosion products. The coated superfer 800H alloy showed the highest corrosion resistance among the examined superalloys. CeO_2 was found to be distributed in the coating along the splat boundaries, whereas Al streaks distributed non-uniformly. The main phases observed for the coated superalloys are the oxides of Ni, Cr, Al, and spinels, which are suggested to be responsible for developing corrosion resistance. The surface morphology of the as-sprayed coating depicts the formation of un-melted particles in the form of a globular dendritic structure. The diameter of the dendritic structure is equal to that of original powder particles. Cerium oxide is uniformly distributed along the Ni-rich splat boundaries. Traces of Al are distributed along the Ni-rich splat boundaries. The bare and coated Fe-based superfer 800H superalloy showed least and highest resistance to hot corrosion, respectively. D-gun-sprayed NiCrAlY +0.4 wt.% CeO2 coating was found to be effective in imparting hot corrosion resistance to superfer 800H in the molten salt environment. The formation of oxides along the splat boundaries and within the open pores of the coatings might have acted as a diffusion barrier to the inward diffusion of molten salt. A dense oxide scale formed on the coated superalloys and the hot corrosion resistance of the coating might be due to the formation of protective phases like NiO, Cr_2O_3, Al_2O_3, $NiCr_2O_4$, and Ni Al_2O_4.

Ma et al. (2015) prepared a pure Al coating by a detonation gun (D-gun) spraying process to protect sintered NdFeB magnets. The detonation gun sprayed coating was very uniform and had a low porosity of 0.77%. The thickness of the Al coating was approximately 16 μm. The corrosion current density for the coated sample was 1.30 $x10^{-5}$ A/cm^2 immediately after immersion in 3.5% NaCl solution, compared to 6.54 x 10^{-5} A/cm^2 for the uncoated sample. X-ray photoelectron spectrometry results indicated that the formation of Al_2O_3 film contributed to the increased corrosion resistance of Al coating. Meanwhile, electrochemical impedance spectroscopy with an equivalent electrical circuit was used to ascertain the corrosion process of the Al coatings. The micrographs of the surface and the cross-section of the Al coating on sintered NdFeB permanent magnets are revealed in Fig. 7.67. Results showed that the corrosion procedure consisted of two stages, which agreed with the potential-dynamic polarization test. It was concluded that the Al coating deposited by the D-gun spray process can improve the corrosion resistance of the sintered NdFeB.

Corrosion-resistant Cr_2O_3- Al_2O_3 (50 wt.% Al_2O_3) coatings were sprayed using D-gun process by Rani et al (2017)a on ASTM-SA213-T-22 boiler steel, and Fe-based superalloy Superfer 800 H. The high-temperature corrosion performance of the coated as well as the bare alloys was evaluated in Na_2SO_4–60%V_2O_5 molten salt with an aggressive environment at 900 °C under cyclic conditions. The kinetics of the corrosion were analyzed by the change in

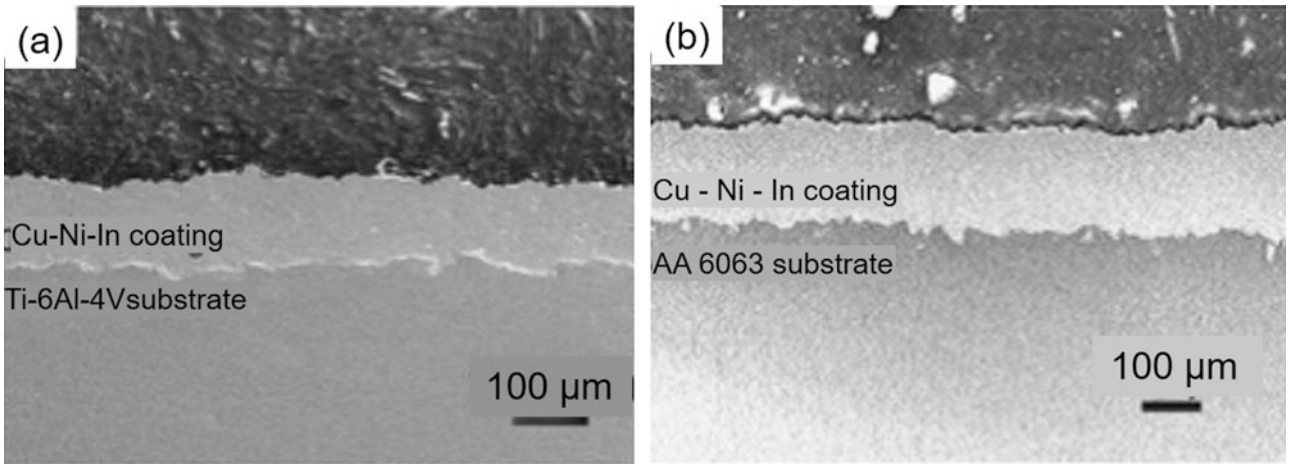

Fig. 7.67 SEM morphologies of the Al coating: (**a**) surface, (**b**) cross-section [Ma et al. (2015)]

weight measurements, which were taken after each cycle (i.e., 1-h heating in a tube furnace followed by 20-min cooling in ambient air) for a total period of 50 cycles. The X-ray diffraction and scanning electron microscopy/energy-dispersive X-ray analysis techniques were used for the analysis of the corrosion products. During investigations, it was found that both the selected bare alloys have suffered intensive spallation in the form of removal of their oxide scales, which may be attributed to the formation of non-protective Fe_2O_3-dominated oxide scales, whereas the coated alloys have shown lesser weight gains along with better adhesiveness of the oxide scales with the substrate till the end of the experiment. The oxides of chromium and aluminum were the main phases revealed in the oxide scales of the coated specimens, which are reported to be protective against the hot corrosion. The Cr_2O_3–50% Al_2O_3 coating was successful in reducing the corrosion rate of the T-22 steel by 97%, in terms of overall weight gains, whereas the reduction was 19% for the Superfer 800H alloy. In case of the Cr_2O_3–50% Al_2O_3-coated T-22 alloy, the weight change was almost negligible throughout the study, whereas in case of the Cr_2O_3–50% Al_2O_3-coated Superfer 800H superalloy, the weight gain abruptly increased after the 25th cycle, but remained lesser than the bare counterpart.

Rani et al. (2017)2 comparatively discussed in the present study the high-temperature hot corrosion behavior of bare and detonation-gun-sprayed Ni-5Al coatings on Ni-based superalloy Inconel-718. Hot corrosion studies were carried out at 900 °C for 100 cycles in the Na_2SO_4–60% V_2O_5 molten salt environment under cyclic heating and cooling conditions. The thermo-gravimetric technique was used to establish the kinetics of hot corrosion. X-ray diffraction, SEM/EDAX, and X-ray mapping techniques were used to analyze the hot corrosion products of bare and coated superalloys. The results indicated that the Ni-5Al-coated superalloy showed very good hot corrosion resistance. The overall weight gain and parabolic rate constant of the Ni-5Al-coated superalloy were less in comparison with the bare superalloy. The D-gun-sprayed Ni-5Al coating was found to be uniform, adherent, and dense in a hot corrosion environment. The formation of nickel- and aluminum-rich oxide scales might have contributed to the better hot corrosion resistance of the coated superalloy. The Ni-5Al coating exhibited dense and uniform lamellar structure with cross-sectional porosity values of around 0.9%, micro-hardness values in the range of 253–306 HV, and surface roughness values in the range of 4.5–5.6 µm.

Mudgal et al. (2015) pointed out that Cr_3C_2–25(NiCr) coatings were widely used in wear, erosion, and corrosion applications. In the present study, D-gun-sprayed Cr_3C_2–25 (NiCr) coatings with and without 0.4 wt.% ceria incorporated were deposited on Superni 718, Superni 600, and Superco 605 substrates. Hot-corrosion runs were conducted in 40%Na_2SO_4–40%K_2SO_4–10%NaCl-10%KCl environment at 900 °C for 100 cycles. Corrosion kinetics were monitored using weight-gain measurements. Characterization of corrosion products was carried out by field-emission scanning electron microscopy (FESEM)/energy-dispersive spectroscopy (EDS) and X-ray diffraction (XRD) techniques. It was observed that Cr_3C_2–25(NiCr) coating with and without added ceria deposited on both of the Ni-based alloys showed resistance to corrosion under the given environment. Addition of ceria enhanced the adherence of the oxide to the coating during the corrosion run and reduced the overall weight gain. However, Cr_3C_2–25 (NiCr)-coated Superco 605 did not perform satisfactorily under this environment. In the case of Superco 605, Cr_3C_2-NiCr with and without ceria did not perform very well in the hot-corrosion run, with a lot of delamination and spallation being observed from a very early stage of exposure. SEM

analysis of all the coatings clearly showed the variation in surface morphology of the coatings with and without ceria doping. In the case of coating without ceria doping, massive oxide along with needle-like morphology could be seen, while in ceria-doped coating some dense patches were observed throughout the surface, with clusters containing ceria in substantial amounts. In the case of corroded coated Superni 718 and Superni 600, Cr_2O_3 and $NiCr_2O_3$ were the major oxides providing protection.

[Kaushal et al. (2014)] recalled that to protect materials from surface degradations such as wear, corrosion, and thermal flux, a wide variety of materials can be deposited on the materials by several spraying processes. Their paper examined and compared the microstructure and high-temperature corrosion of Ni-20Cr coatings deposited on T22 boiler steel by high-velocity oxy-fuel (HVOF), detonation gun spray, and cold spraying techniques. The coatings' microstructural features were characterized by means of XRD and FE-SEM/EDS analyses. Based on the results of mass gain, XRD, and FE-SEM/EDS analyses, it may be concluded that the Ni-20Cr coating sprayed by all the three techniques was effective in reducing the corrosion rate of the steel. Among the three coatings, D-gun spray coating proved to be better than HVOF-spray and cold-spray coatings.

(vi) Erosion resistance

It is known that the addition of Cr to WC–Co improves the binding of the metallic matrix with the WC grains and provides better wear-resistant coatings. Thus, WC–Co–Cr is considered to be a potentially better wear-resistant coating material as compared to WC–Co. The thermally sprayed carbide coatings are in general surface finished by machining or grinding after the coating process. A WC-10Co-4Cr powder has been sprayed [Murthy et al. (2001)] on medium-carbon steel using D-gun and HVOF processes. Some of the coated specimens were further ground by a diamond wheel with controlled parameters, and both "as-coated" and "as-ground" conditions have been tested for solid particle erosion behavior. It has been found that surface grinding improved the erosion resistance. A detailed analysis indicates that the increase in residual stress in the ground specimen is a possible cause for the improvement in erosion resistance. Sand erosion studies of D-gun sprayed WC-Co-Cr have been undertaken [Wood et al. (1997)] using a sand/water jet impingement rig. The erosion rate of coatings compared well with sintered tungsten carbide-cobalt-chrome for low-energy impacts, but the sintered material outperforms the sprayed material for high-energy impacts by a factor of four. This fact is the result from the anisotropic microstructure of coatings with preferred crack propagation parallel to the coating surface, followed by crack interlinking and spalling. The influence of the angle of impingement of the sand/water slurry jet with respect to the surface of the coated part was found to be most pronounced for low energy slurries compared to that under high energy conditions. Maximum erosion rates in this case were obtained with the slurry jet impinging the surface of the part at 90^o, while minimal erosion rates were observed at angles below 30^o. In contrast, the erosion rate using high energy slurries were essentially independent of the jet angel.

WC-12%Co and WC-17%Co coatings were deposited [Manish (2002)] by detonation spraying on three different substrate materials—mild steel, commercially pure (CP) aluminum, and CP titanium—to test their dynamic hardness by a drop weight system. WC-Co coatings exhibit higher hardness under impact at a high strain rate. The dynamic hardness of a WC-Co coating is maximum on aluminum substrate and minimum on mild steel substrate. The identical coating exhibits intermediate hardness on titanium substrate.

Harpreet Singh Grewal et al. (2012) deposited WC-Co-Cr coatings on some hydro-turbine 13Cr4Ni and 16Cr5Ni steels by the detonation-gun spray process. An in-depth characterization of the as-sprayed coating was done using X-ray diffraction (XRD) and scanning electron microscopy (SEM)/energy-dispersive X-ray spectroscopy (EDS) techniques. Microhardness and porosity measurements were also made. The coating was found to have a typical splat-like morphology with some indications of un-melted carbide particles. The XRD results showed the presence of WC as the primary phase along with W_2C and Co_6W_6C as secondary phases. Furthermore, the slurry erosion behavior of the coatings was investigated to ascertain the usefulness of the coatings to reduce the slurry erosion of the steels. The effect of four operating factors viz. the velocity, impact angle, concentration, and particle size on the slurry erosion of coated and bare steels have been studied using a high-speed jet-type test rig. The sand used as an erodent was collected from a power plant to replicate the actual turbine conditions. It has been observed that the given cermet coating can enhance the erosion resistance of the steel. Velocity was found to be the most significant factor affecting the erosion behavior of the coating, whereas it was the erodent particle size in the case of uncoated steel. As evidenced from the SEM images, the platelet mechanism of erosion seemed to be the prominent one, causing the removal of material from the surface of the steel, whereas for the coating, the formation and interlinking of cracks resulted in the removal of material.

(vii) Fatigue

Ganesh Sundara Raman et al. (2007) sprayed, using the detonation gun (D-gun) spray process, Cu-Ni-In coating on two substrate materials: Ti-alloy (Ti-6Al-4 V) and Al-alloy (AA 6063) fatigue test specimens. Coatings on both substrates were dense with low porosity, high hardness, and high surface roughness, see Fig. 7.68. Relatively higher surface compressive residual stress was present at the coating on

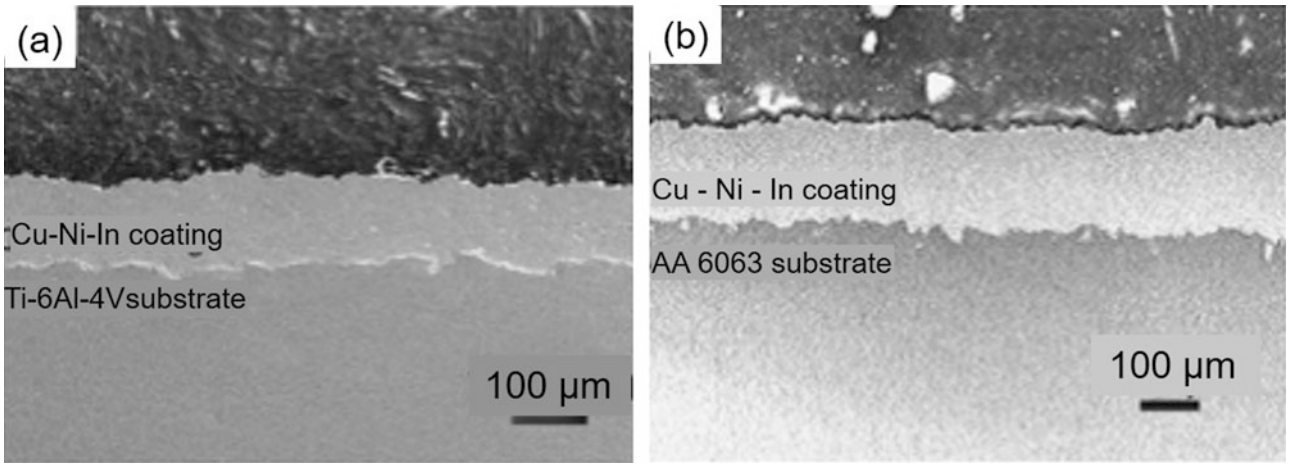

Fig. 7.68 SEM micrographs showing the cross section of Cu-Ni-In coating on two different substrates: (**a**) Ti-6Al-4 V; (**b**) AA 6063 [Ganesh Sundara Raman et al. (2007)]

Ti-alloy specimens. In case of the coating on Al-alloy samples, tensile residual stress was also present in some places. Uniaxial plain fatigue and fretting fatigue experiments were conducted on uncoated and coated specimens. The detrimental effect of life reduction due to fretting was relatively larger in the Al-alloy compared to the Ti-alloy. While Cu-Ni-In coating was found to be beneficial on the Ti-alloy, it was deleterious on the Al-alloy substrate under both plain fatigue and fretting fatigue loading. The results were explained in terms of differences in the values of surface hardness, surface roughness, surface residual stress, and friction stress.

The mismatch in the properties of coating and substrate was less in case of the Cu-Ni-In coating on Ti- 6Al-4 V alloy than the Cu-Ni-In coating on AA 6063. The detrimental effect of life reduction due to fretting was relatively larger in the Al-alloy compared with that in the Ti-alloy. While the Cu-Ni-In coating was found to be beneficial on the Ti-alloy, it was deleterious on the Al-alloy substrate under both plain fatigue and fretting fatigue loading. The results were explained in terms of differences in the values of surface hardness, surface roughness, surface residual stress, and friction stress.

(viii) Boiler environment

Kaushal et al. (2011) used two spray techniques—high-velocity-oxy-fuel (HVOF) spray and detonation-gun (D-gun) spray—to deposit Ni-20Cr coatings on a commonly used boiler steel ASTM-SAE 213-T22. The specimens, with and without coating, were subjected to molten salt (Na_2SO_4–60% V_2O_5) deposition in a laboratory furnace at 900 °C to determine hot-corrosion resistance. Specimens were also exposed to the superheater zone of a thermal power plant boiler at an average temperature of 700 °C under cyclic conditions to ascertain their erosion-corrosion (E-C) behavior. Mass-change measurements were taken to approximate the kinetics of corrosion and erosion-corrosion. In the case of E-C, the thickness lost data were also taken at the end of the exposure. The exposed specimens were characterized by X-ray diffraction (XRD) and field-emission scanning electron microscopy/energy dispersive spectroscopy (FE-SEM/EDS). The HVOF-sprayed coating was found to be intact during exposure to both given environments, whereas the D-gun coating showed spallation of its oxide scale during exposure to the molten salt environments. An overall analysis of the results indicated that the HVOF-sprayed Ni-20Cr coating should be a better choice for the given.

7.4.4.5 Other Cermets

Metal-matrix composites (MMCs), containing large ceramic particles as super-abrasives, are typically used for grinding stone, minerals, and concrete. Sintering and brazing are the key manufacturing technologies for grinding tool production. However, restricted geometry flexibility and the absence of repair possibilities for damaged tool surfaces, as well as difficulties of controlling material interfaces, are the main weaknesses of these production processes. Thermal spraying offers the possibility to avoid these restrictions [Oliker et al. (2006)]. Cu-based coatings containing large ceramic particles (Al_2O_3 and SiC particles larger than 150 μm) gave high abrasiveness for grinding stones and concrete [Tillmann et al. (2007)].

FeTi-SiC coatings gave very high hardness (7900 MPa) when spraying agglomerated powders with fine SiC. The coatings contained $TiSi_2$, TiSi, Ti_5Si_3, and FeTiSi, and the porosity was below 2% [Oliker et al. (2005)]. Detonation coatings of mechanically Ti-Al alloyed powders [5.231] contained titanium aluminide with the inclusion of nitrides, depending on the working gas environment. With the mechanically alloyed powder Ti-50Al, coatings can be consolidated by the formation of the compound Al_2TiO_5 obtained when the working gas is oxidizing [Oliker et al.

(2005)]. Filimonov et al. (2008) have considered the mechanisms of structure formation during gas detonation spraying of coatings of $TiAl_3$ and Ni_3Al intermetallic compounds produced under equilibrium and non-equilibrium synthesis conditions.

Podchernyaeva et al. (2003) have investigated the composition, structure, and wear rate of detonation coatings on steel 30KhGSNA deposited from composite powders based on $TiC_{0.5}N_{0.5}$ with refractory additions of SiC, AlN, and a Ni-Cr metallic binder. It was shown that at a load of 10 MPa, these coatings exhibited substantially less wear and a larger range of sliding velocities with a stable value of wear than coatings of the hard alloy WC-15% Co.

A kind of Ti-Fe-Ni-C compound powder was prepared by a novel precursor pyrolysis process using ferro-titanium, carbonyl nickel powder, and sucrose as raw materials [Zhu et al. (2008)]. The powder had a very compact structure and was uniform in particle size. The TiC-Fe36Ni composite coatings were simultaneously in-situ synthesized by reactive D-gun spraying using this powder. The coatings presented the typical morphology of thermally sprayed coatings with two different areas: one was the area of TiC distribution where the round fine TiC particles (from 300 nm to 1 μm) were dispersed in the Fe36Ni alloy matrix; the other was the area of TiC accumulation (from 2 to 4 μm). The surface hardness of the composite coating reached about 94 ± 2 (HV_{15N}).

The effects of the powder particle size and the acetylene/oxygen gas flow ratio during the D-gun spray process on the amount of molybdenum phase, porosity, and hardness of the coatings using MoB powder were investigated by Yang et al. (2001). The results show that the presence of metallic molybdenum in the coating results from decomposition of MoB powder during thermal spray. The compositions of the coatings are metallic Mo, MoB, and Mo_2B, which are different from the phases of the original powder. Similar results were obtained by Gao et al. (2001).

7.4.4.6 Alloys

[Senderowski and Bojar (2008), Senderowski and Bojar (2009)] have studied D-gun sprayed NiAl and NiCr intermediate layers underneath the intermetallic Fe–Al type coatings on a plain carbon steel substrate. The interface layers are responsible for the hardness, bond strength, thermal stability, and adhesive strength of the whole coating structure. The physical–chemical properties of the intermediate layers, combined with a unique, very dense, and pore-free intermetallic Fe–Al coating obtained from self-decomposing powders resulted in a more complex structure. It enabled independent control of its functional properties and considerably reduced negative gradients of stress and temperature influencing the substrate and increasing adhesion strength.

7.5 Summary and Conclusions

This chapter was devoted to spray processes where thermal and kinetic energies are generated chemically through the combustion (or detonation) of fuels (gaseous or liquid) with oxygen or air. The oldest process is flame spraying, which appeared in 1910 and is still in common use. Oxyacetylene torches are the most common, and undoubtedly this process is the cheapest one. The use of rods or cords has allowed spraying ceramics, which otherwise as powders would not have been melted. The main limitation of the flame process is the relatively low velocity of sprayed particles (< 60–80 m/s) resulting in porous coatings. Oxide inclusions are also present due to the high degree of interaction between fully molten droplets and the surrounding atmosphere.

The detonation gun (D-gun) appeared in Western countries in the 1950s. In this process, very high thermal and kinetic energies were achieved by producing a detonation in an explosive mixture (mostly acetylene-oxygen) confined in a tube closed at one end into which the powder is introduced. Of course, the process is cyclic (6–100 Hz) with the introduction of the explosive gases and powder dose, the detonation, ignited by a spark plug followed by the purging of burned gases. The process generates high particle velocities (500–900 m/s) and fully molten particles (even ceramic ones, provided their size is small <30 μm). Thus, coatings are dense (less than 2% porosity), well bonded, with compressive stress, and their oxidation is limited.

In the 1960s, to compete with the D-gun deposition, the HVOF process was introduced where the combustion flame is produced in a pressurized chamber followed by a convergent-divergent nozzle and a barrel to limit the surrounding atmosphere entrainment. First developed with gaseous combustible gases and oxygen, it was extended by replacing oxygen by air (HVAF process) to reduce the gas temperature and increase its velocity. The next step was the high-power HVOF torches working with kerosene followed by HVOF processes where non-combustible gas (nitrogen) was introduced in the combustion chamber or water injected downstream of the nozzle throat. These new torches were aimed at reducing the gas temperature and increasing the velocity. Coatings obtained with HVOF torches are rather dense and their oxidation level is rather low. Of course, the density increases with particle impact velocity that varies with the combustible gas or liquid used with either oxygen or air or nitrogen addition in the combustion chamber. Velocities between 400 and 900 m/s can be achieved for the same particles depending on the spray conditions and gun used. With high velocities (> 700 m/s), it becomes possible to spray particles below their melting point and thus with a low oxidation level. However, it must be emphasized that these processes are not suited to spraying ceramics.

Nomenclature

Units are indicated in parentheses; when no units are indicated, the parameter is dimensionless.

Latin Alphabet

a_i	local sound velocity, $a_i = \sqrt{\gamma\rho/\rho_g}$ (m/s)
A	oxidizer volume or mass (m^3 or kg)
A_i	cross-sectional area perpendicular to the direction of the flow (m^2)
A_t	throat area (m^2)
D	detonation wave velocity (m/s)
F	fuel volume or mass (m^3 or kg)
F/A	fuel to oxidizer molar ratio
h_i	enthalpy (J/kg)
$\dot{m}_{O_2}$	oxygen gas feed rate (kg/s)
M_a	Mach number, $Ma = vg/ai$
p	pressure (Pa)
p_t	gas pressure at the throat (Pa)
P_F	power dissipated in the flame (kW)
q	chemical energy release at constant pressure (J/kg)
Q	Gas flow rate (slm)
E_D	specific energy of detonation (J)
R	perfect gas constant (J/K.kg)
S_t	stoichiometric factor $S_t = Q_{O_2}/\left(Q_{O_2}\right)_{St.}$
R_u	universal gas constant (8.32 J/K.mole)
R'	flame richness ratio $R' = (F/A)/(F/A)_{St.}$
t_c	detonation cycle duration time (s)
T_g	gas temperature (K)
T_m	melting temperature (K)
T_p	particle temperature (K)
T_t	temperature at the throat (K)
u_b	burned gas velocity (m/s)
u_u	unburned gas velocity (m/s)
v_f	flame velocity (m/s)
v_g	g velocity (m/s)

Greek Alphabet

b	burned gases (in the immediate vicinity behind the front)
g	gas
p	particle
t	throat
u	unburned gas (before the detonation wave front)

Subscripts

Δt_i	characteristic time intervals of a detonation (s)
ϕ	dummy variable
ϕ'	time- (or Reynolds) averaged dumb variable
ϕ"	density-averaged dumb variable
γ	specific heats ratio $\gamma = c_p/c_v$
ρ_g	gas mass density (kg/m^3)
ρ_p	particle mass density (kg/m^3)
ρ_t	gas mass density at the throat (kg/m^3)

References

Aalamialeagha, M.E., S.J. Harris, and M. Emamighomi. 2003. Influence of the HVOF spraying process on the microstructure and corrosion behavior of Ni-20%Cr coatings. *Journal of Materials Science* 38: 4587–4596.

Ahmed, R., and M. Hadfield. 2002. Mechanisms of fatigue failure in thermal spray coatings. *Journal of Thermal Spray Technology* 11 (4): 551–558.

Altomare, L., D. Bellucci, G. Bolelli, B. Bonferroni, V. Cannillo, L. De Nardo, R. Gadow, A. Killinger, L. Lusvarghi, A. Sola, and N. Stiegler. 2011. Microstructure and in vitro behaviour of 45S5 bioglass coatings deposited by high velocity suspension flame spraying (HVSFS). *Journal of Materials Science: Materials in Medicine* 22: 1303–1319.

American Welding Society. 1985. *Thermal spraying, practice*. Miami: Theory and Application.

Ang, A.S.M., H. Howse, S.A. Wade, and C.C. Berndt. 2016. Development of processing windows for HVOF carbide-based coatings. *Journal of Thermal Spray Technology* 25 (1–2): 28–35.

Anon. 1913. Metal plating with the air brush. *Scientific American* 1: 346–352.

Arcondéguy, A., A. Grimaud, A. Denoirjean, G. Gasnier, C. Huguet, B. Pateyron, and G. Montavon. 2007. Flame-sprayed glaze coatings: Effect of operating parameters and feedstock characteristics onto coating structures. *Journal of Thermal Spray Technology* 16 (5–6): 978–990.

Ashrafizadeh, H., A. McDonald, and P. Mertiny. 2016. Deposition of electrically conductive coatings on Castable polyurethane elastomers by the flame spraying process. *Journal of Thermal Spray Technology* 25 (3): 419–430.

Astakhov, E.A. 2008. Controlling the properties of detonation-sprayed coatings: Major aspects. *Powder Metallurgy and Metal Ceramics* 47 (1–2): 70–79.

Bandyopadhyay, R., and Per Nylén. 2003. A computational fluid dynamic analysis of gas and particle flow in flame spraying. 12 (4): 494–503.

Barisov, Yui S., E.A. Asstachov, and V.S. Klimenko. 1990. *Detonation Spraying equipment, materials and Applications*, 26–32. Essen, Germany: Thermische Spritzkonferenz.

Barthel, K., S. Rambert, and St. Siegmann. 2000. Microstructure and polarization resistance of thermally sprayed composite cathodes for solid oxide fuel cell use. *Journal of Thermal Spray Technology* 9 (3): 343–347.

Bartuli, C., T. Valente, F. Cipri, E. Bemporad, and M. Tului. 2005. Parametric study of an HVOF process for the deposition of nanostructured WC-co coatings. *Journal of Thermal Spray Technology* 14 (2): 187–195.

Belzunce, F.J., V. Higuera, S. Poveda, and A. Carriles. 2002. High temperature of HFPD thermal-sprayed MCrAlY coatings in simulated gas turbine environments. *Journal of Thermal Spray Technology* 11 (4): 461–467.

Bergant, Z., and J. Grum. 2009. Quality improvement of flame sprayed, heat treated, and Remelted NiCrBSi coatings. *Journal of Thermal Spray Technology* 18 (3): 380–391.

Berghaus, Oberste J., J.-G. Legoux, C. Moreau, R. Hui, C. Decès-Petit, W. Qu, S. Yick, Z. Wang, R. Maric, and D. Ghosh. 2008. Suspension HVOF spraying of reduced temperature solid oxide fuel cell electrolytes. *Journal of Thermal Spray Technology* 17 (5–6): 700–707.

Bhandari, S., H. Singh, H.K. Kansal, and V. Rastogi. 2012. Slurry Erosion behaviour of detonation gun spray Al_2O_3 and Al_2O_3–$13TiO_2$-coated CF8M steel under hydro accelerated conditions. *Tribology Letters* 45: 319–331.

Bobzin, K., M. Ote, T.F. Linke, and K.M. Malik. 2016. Wear and corrosion resistance of Fe-based coatings reinforced by TiC particles for application in hydraulic systems. *Journal of Thermal Spray Technology* 25 (1–2): 365–374.

Bolelli, G., and L. Lusvarghi. 2006. Heat treatment effects on the Tribological performance of HVOF sprayed co-Mo-Cr-Si coatings. *Journal of Thermal Spray Technology* 15 (4): 802–810.

Bolelli, G., V. Cannillo, L. Lusvarghi, and S. Ricco. 2006. Mechanical and tribological properties of electrolytic hard chrome and HVOF-sprayed coatings. *Surface & Coatings Technology* 200: 2995–3009.

Bolelli, G., J. Rauch, V. Cannillo, A. Killinger, L. Lusvarghi, and R. Gadow. 2009. Microstructural and Tribological Investigation of High-Velocity Suspension Flame Sprayed (HVSFS) Al_2O_3 Coatings. *Journal of Thermal Spray Technology* 18 (1): 35–49.

Brandl, W., D. Toma, J. Kruger, H.J. Grabke, and G. Matthäus. 1997. The oxidation behavior of HVOF thermal-sprayed MCrAlY coatings. *Surface and Coatings Technology* 93-95: 21–26.

Brantner, H.P., R. Pippan, and W. Prantl. 2003. Local and global fracture toughness of a flame sprayed molybdenum coating. *Journal of Thermal Spray Technology* 12 (4): 560–571.

Browning, J.A. 1983. *Highly concentrated supersonic liquefied material flame spray method and apparatus*. US patent # 4,416,421, November.

———. 1992. Hypervelocity impact fusion-a technical note. *Journal of Thermal Spray Technology* 1 (4): 289–229.

———. 1999. Viewing the future of HVOF and HVAF thermal spraying. *Journal of Thermal Spray Technology* 8 (3): 351–356.

Cannon, J.E., M. Alkam, and P.B. Butler. 2008. Efficiency of pulsed detonation thermal spraying. *Journal of Thermal Spray Technology* 17 (4): 456–464.

Cetegen, B.M., and S. Basu. 2009. Review of modeling of liquid precursor droplets and particles injected into plasmas and high-velocity oxy-fuel (HVOF) flame jets for thermal spray deposition applications. *Journal of Thermal Spray Technology* 18 (5–6): 769–793.

Chang-Jiu, Li, and Yu-Yue Wang. 2002. Effect of particle state on the adhesive strength of HVOF sprayed metallic coating. *Journal of Thermal Spray Technology* 11 (4): 523–552.

Chebbi, A., and J. Stokes. 2012. Thermal spraying of bioactive polymer coatings for orthopedic applications. *Journal of Thermal Spray Technology* 21 (3–4): 719–730.

Chen, W.R., X. Wua, B.R. Marple, D.R. Nagy, and P.C. Patnaik. 2008. TGO growth behavior in TBCs with APS and HVOF bond coats. *Surface & Coatings Technology* 202 (12): 2677–2683.

Cheng, D., Q. Xu, G. Trapaga, and E.J. Lavernia. 2001. The effect of particle size and morphology on the in-flight behavior of particles during high-velocity oxyfuel thermal spraying. *Metallurgical and Materials Transactions B* 32 (3): 525–535.

———. 2001b. A numerical study of high-velocity oxygen fuel thermal spraying process. Part I: gas phase dynamics. *Metallurgical and Materials Transactions A* 32A: 1609–1620.

Chow, R., T.A. Decker, R.V. Gansert, D. Gansert, and D. Lee. 2003. Properties of aluminium deposited by a HVOF process. *Journal of Thermal Spray Technology* 12 (2): 208–213.

Deng, C., M. Liu, C. Wu, K. Zhou, and J. Song. 2007. Impingement resistance of HVAF WC-based coatings. *Journal of Thermal Spray Technology* 16 (5–6): 604–609.

Dent, A.H., S. DePalo, and S. Sampath. 2002. Examination of the wear properties of HVOF sprayed nanostructured and conventional WC-co Cermets with different binder phase contents. *Journal of Thermal Spray Technology* 11 (4): 551–558.

Dobbins, T.A., R. Knight, and M.J. Mayo. 2003. HVOF thermal spray deposited Y_2O_3- ZrO_2 coatings for thermal barrier applications. *Journal of Thermal Spray Technology* 12 (2): 214–225.

Dobler, K., H. Kreye, and R. Schwetzke. 2000. Oxidation of stainless steel in the high velocity oxy-fuel process. *Journal of Thermal Spray Technology* 9 (3): 407–413.

Dolatabadi, A., V. Pershin, and J. Mostaghimi. 2005. New attachment for controlling gas flow in the HVOF process. *Journal of Thermal Spray Technology* 14 (1): 91–99.

Dongmo, E., R. Gadow, A. Killinger, and M. Wenzelburger. 2009a. Modeling of combustion as well as heat, mass, and momentum transfer during thermal spraying by HVOF and HVSFS. *Journal of Thermal Spray Technology* 18 (5–6): 896–908.

Dongmo, E., A. Killinger, M. Wenzelburger, and R. Gadow. 2009b. Numerical approach and optimization of the combustion and gas dynamics in High Velocity Suspension Flame Spraying (HVSFS). *Surface & Coatings Technology* 203: 2139–2145.

Du, H., W. Hua, J. Liu, J. Gong, C. Sun, and L. Wen. 2005. Influence of process variables on the qualities of detonation gun sprayed WC–Co coatings. *Materials Science and Engineering A* 408: 202–210.

Du, H., C. Sun, W.G. Hua, Y.S. Zhang, Z. Han, T.G. Wang, J. Gong, and S.W. Lee. 2006. Fabrication and evaluation of D-gun sprayed WC–Co coating with self-lubricating property. *Tribology Letters* 23 (3): 261–266.

Du, H., C. Sun, W. Hua, T. Wang, J. Gong, X. Jiang, and S. Wohn Lee. 2007. Structure, mechanical and sliding wear properties of WC-Co/MoS2-Ni coatings by detonation gun spray. *Materials Science and Engineering A* 445-446: 122–134.

Edrisy, A., T. Perry, and A.T. Alpas. 2005. Wear mechanism maps for thermal-spray steel coatings. *Metallurgical and Materials Transactions* 36A: 2737–2750.

Endo, T., R. Obayashi, T. Tajiri, K. Kimura, Y. Morohashi, T. Johzaki, K. Matsuoka, T. Hanafusa, and S. Mizunari. 2016. Thermal spray using a high-frequency pulse detonation combustor operated in the liquid-purge mode. *Journal of Thermal Spray Technology* 25 (3): 494–508.

Evdokimenko, Y.I., V.M. Kisel, V. Kh, A. Kadyrov, A. Korol, and O.I. Get'man. 2001. High-velocity flame spraying of powder Aluminium protective coatings. *Powder Metallurgy and Metal Ceramics* 40 (3–4): 121–126.

Filimonov, V. Yu, V.I. Yakovlev, M.A. Korchagin, M.V. Loginova, A.S. Semenchina, and A.V. Afanas'ev. 2008. Structure formation during gas-detonation spraying of coatings from composite powders $TiAl_3$ and Ni_3Al. *Combustion, Explosion, and Shock Waves* 44 (5): 591–596.

Fossati, A., M. Di Ferdinando, A. Lavacchi, U. Bardi, C. Giolli, and A. Scrivani. 2010. Improvement of the isothermal oxidation resistance of CoNiCrAlY coating sprayed by high velocity oxygen fuel. *Surface & Coatings Technology* 204: 3723–3728.

Furuhata, T., S. Tanno, T. Miura, Y. Ikeda, and T. Nakajima. 1997. Performance of numerical spray combustion simulation, energy convers. *Manage* 38 (10–13): 1111–1122.

Ganesh Sundara Raman, S., B. Rajasekaran, S.V. Joshi, and G. Sundararajan. 2007. Influence of substrate material on plain fatigue and fretting fatigue behavior of detonation gun sprayed cu-Ni-in coating. *Journal of Thermal Spray Technology* 16 (4): 571–579.

Gao, Y., H. Zu-kun, X. Xiaolei, and X. Gang. 2001. Formation of molybdenum boride cermet coating by the detonation spray process. *Journal of Thermal Spray Technology* 10 (3): 456–460.

Gärtner, F., T. Stoltenhoff, T. Schmidt, and H. Kreye. 2006. The Cold Spray Process and Its Potential for Industrial Applications. *Journal of Thermal Spray Technology* 15 (2): 223–232.

Gavrilenko, T.P., and Yu.A. Nikolaev. 2006. Limits of gaseous detonation spraying. *Combustion, Explosion, and Shock Waves* 42 (5): 594–597.

———. 2007. Calculation of detonation gas spraying. *Combustion, Explosion, and Shock Waves* 43 (6): 724–731.

Gawne, D.T., T. Zhang, and Y. Bao. 2001. Heating effect of flame impingement on polymer coatings, thermal spray 2001. In *New surfaces for a new millennium*, ed. C. Berndt, K. Khor, and E. Lugscheider. Materials: ASM International.

Glassman, I. 1977. *Combustion*. New York: Academic.

Gonzalez, R., H. Ashrafizadeh, A. Lopera, P. Mertiny, and A. McDonald. 2016. A review of thermal spray metallization of polymer-based structures. *Journal of Thermal Spray Technology* 25 (5): 897–919.

Gordon, S., and B.J. McBride. 1994. *Computer program for calculation of complex chemical equilibrium compositions and applications*, NASA reference publication 1311. Cleveland: Lewis Research Center.

Grewal, Harpreet Singh, Sanjeev Bhandari, and Harpreet Singh. 2012. Parametric study of slurry-Erosion of hydro-turbine steels with and without detonation gun spray coatings using Taguchi technique. *Metallurgical and Materials Transactions A* 43A: 3387–3401.

Gross, K.A., J. Tikkanen, J. Keskinen, V. Pitkänen, M. Eerola, R. Siikamaki, and M. Rajala. 1999. Liquid flame spraying for glass coloring. *Journal of Thermal Spray Technology* 8 (4): 583–589.

Gu, S., C.N. Eastwick, K.A. Simmons, and D.G. McCartney. 2001. Computational fluid dynamic modelling of gas flow characteristics in a high-velocity oxy-fuel thermal spray system. *Journal of Thermal Spray Technology* 10 (3): 461–469.

Gu, S., D.G. McCartney, C.N. Eastwick, and K. Simmons. 2004. Numerical modeling of in-flight characteristics of Inconel 625 particles during high-velocity oxy-fuel thermal spraying. *Journal of Thermal Spray Technology* 13 (2): 200–213.

Guilemany, J.M., N. Espallargas, P.H. Suegama, A.V. Benedetti, and J. Fernández. 2005. High-velocity oxyfuel Cr_3C_2-NiCr replacing hard chromium coatings. *Journal of Thermal Spray Technology* 14 (3): 335–341.

Gupta, M., N. Markocsan, X.-H. Li, and L. Östergren. 2018. Influence of bond-coat spray process on lifetime of suspension plasma-sprayed thermal barrier coatings. *Journal of Thermal Spray Technology* 27: 84–97.

Hackett, C.M., and G.S. Settles. 1995. Research on HVOF gas shrouding for coating oxidation control. In *Thermal spray: Science and technology*, ed. C.C. Berndt and S. Sampath, 21–29. Geauga County: ASM International, Materials Park.

Hall, A., D. Urrea, J. Mccloskey, D. Beatty, T. Roemer, and D. Hirschfeld. 2010. The effect of torch hardware on particle temperature and particle velocity distributions in the powder flame spray process. *Journal of Thermal Spray Technology* 19 (4): 824–827.

Han, Y., H. Chen, D. Gao, G. Yang, B. Liu, Y. Chu, J. Fan, and Y. Gao. 2017. Microstructural evolution of NiCoCrAlHfYSi and NiCoCrAlTaY coatings deposited by AC-HVAF and APS. *Journal of Thermal Spray Technology* 26: 1758–1775.

Hanshin, C., S. Lee, B. Kim, H. Jo, and C. Lee. 2005. Effect of in-flight particle oxidation on the phase evolution of HVOF NiTiZrSiSn bulk amorphous coating. *Journal of Materials Science* 40: 6121–6126.

Hanson, T.C., C.M. Hackett, and G.S. Settles. 2002. Independent control of HVOF particle velocity and temperature. *Journal of Thermal Spray Technology* 11: 75–85.

Harsha, S., D.K. Dwivedi, and A. Agarwal. 2007. Influence of CrC addition in Ni-Cr-Si-B flame sprayed coatings on microstructure, microhardness and wear behaviour. *Surface & Coatings Technology* 201: 5766–5775.

Hassan, B., A.R. Lopez, and W.L. Oberkampf. 1998. Computational analysis of a three-dimensional High-Velocity Oxygen Fuel (HVOF) thermal spray torch. *Journal of Thermal Spray Technology* 7 (1): 71–77.

He, J., M. Ice, and E. Lavernia. 2001. Particle melting behavior during high-velocity oxygen fuel thermal spraying. *Journal of Thermal Spray Technology* 10 (1): 83–93.

Henkes and H. Olivier, J (2014) Particle Acceleration in a High Enthalpy Nozzle Flow with a Modified Detonation Gun. *J Thermal Spray Technology* 23(4) 626-640

Hideki, I., U. Shibakumaran, and G. Kazumasa. 1991. *Method for thermally spraying and grazing cement martial*. Japanese patent JP3033084, 13-02-1991.

Higuera, V., F.J. Belzunce, A. Carriles, and S. Poveda. 2002. Influence of the thermal-spray procedure on the properties of a nickel-chromium coating. *Journal of Materials Science* 37: 649–654.

Horlock, A.J., Z. Sadeghian, D.G. McCartney, and P.H. Shipway. 2005. High-velocity Oxyfuel reactive spraying of mechanically alloyed Ni-Ti-C powders. *Journal of Thermal Spray Technology* 14 (1): 77–84.

Huang, J., Y. Liu, J. Yuan, and H. Li. 2014. Al/Al_2O_3 composite coating deposited by flame spraying for marine applications: Alumina skeleton enhances anti-corrosion and Wear performances. *Journal of Thermal Spray Technology* 23 (4): 676–683.

Hussary, N.A., and J.V.R. Heberlein. 2007. Effect of system parameters on metal breakup and particle formation in the wire arc spray process. *Journal of Thermal Spray Technology* 16 (1): 140–152.

Ishikawa, K., T. Suzuki, Y. Kitamura, and S. Tobe. 1999. Corrosion resistance of thermal sprayed titanium coatings in chloride solution. *Journal of Thermal Spray Technology* 8 (2): 273–278.

Ishikawa, K., T. Suzuki, S. Tobe, Y. Kitamura, and K. Ishikawa. 2001. Alloy against aqueous corrosion. *Journal of Thermal Spray Technology* 10 (3): 520–525.

Ishikawa, Y., J. Kawakita, S. Osawa, T. Itsukaichi, Y. Sakamoto, M. Takaya, and S. Kuroda. 2005. Evaluation of corrosion and Wear resistance of hard cermet coatings sprayed by using an improved HVOF process. *Journal of Thermal Spray Technology* 14 (3): 384–390.

Ishikawa, Y., S. Kuroda, J. Kawakita, Y. Sakamoto, and T. Matsufumi. 2007. Sliding wear properties of HVOF sprayed WC–20%Cr_3C_2–7%Ni cermet coatings. *Surface & Coatings Technology* 201: 4718–4727.

Ivosevic, M., R. Knight, S.R. Kalidindi, G.R. Palmese, and J.K. Sutter. 2005. Adhesive/cohesive properties of thermally sprayed functionally graded coatings for polymer matrix composites. *Journal of Thermal Spray Technology* 14 (1): 45–51.

Ivosevic, M., R.A. Cairncross, and R. Knight. 2007. Melting and degradation of Nylon-11 particles during HVOF combustion spraying. *Journal of App. Pol. Science* 105 (2): 827–837.

Ivosevic, M., S.L. Coguill, and S.L. Galbraith. 2009. Polymer thermal spraying: A novel coating process. In *Thermal spray 2009: Proceedings of the international thermal spray conference*, ed. B.R. Marple, M.M. Hyland, Y.-C. Lau, C.-J. Li, R.S. Lima, and G. Montavon, 1078–1083. Materials Park, OH, USA: ASM International.

Jackson, L., M. Ivosevic, R. Knight, and R.A. Cairncross. 2007. Sliding Wear properties of HVOF thermally sprayed Nylon-11 and Nylon-11/ceramic composites on steel. *Journal of Thermal Spray Technology* 16 (5–6): 927–932.

Jacobs, L., M.M. Hyland, and M. De Bonte. 1998. Comparative study of WC-cermet coatings sprayed via the HVOF and the HVAF process. *Journal of Thermal Spray Technology* 7 (2): 213–218.

———. 1999. Study of the influence of microstructural properties on the sliding-Wear behavior of HVOF and HVAF sprayed WC-cermet coatings. *Journal of Thermal Spray Technology* 8 (1): 125–132.

Jang, H.-J., D.-H. Park, Y.-G. Junga, J.-C. Jang, S.-C. Choi, and U. Paik. 2006. Mechanical characterization and thermal behavior of HVOF-sprayed bond coat in thermal barrier coatings (TBCs). *Surface & Coatings Technology* 200: 4355–4362.

Jayaganthan, R., S. Prakash, and Sanjay Kumar. 2008. Hot corrosion behavior of detonation gun sprayed Cr_3C_2–NiCr coatings on Ni and Fe-based superalloys in Na_2SO_4–60% V_2O_5 environment at 900 °C. *Journal of Alloys and Compounds* 463: 358–372.

Ji, G.-C., C.-J. Li, Y.-Y. Wang, and W.-Y. Li. 2007. Erosion performance of HVOF-sprayed Cr_3C_2-NiCr coatings. *Journal of Thermal Spray Technology* 16 (4): 557–565.

Jin, Kawakita, Seiji Kuroda, Takeshi Fukushima, and Toshiaki Kodama. 2005. Improvement of corrosion resistance of high-velocity oxyfuel-sprayed stainless-steel coatings by addition of molybdenum. *Journal of Thermal Spray Technology* 14 (2): 224–230.

Jorge, Lino F., Teresa P. Duarte, and Ricardo Maia. 2003. Development of coated ceramic components for the aluminum industry. *Journal of Thermal Spray Technology* 12 (2): 250–257.

Kadyrov, E. 1996. Gas-particle interaction in detonation spraying systems. *Journal of Thermal Spray Technology* 5 (2): 185–195.

Kadyrov, E., and V. Kadyrov. 1995. Gas dynamical parameters of detonation powder spraying. *Journal of Thermal Spray Technology* 4 (3): 280–286.

Kamal, S., R. Jayaganthan, S. Prakash, and Sanjay Kumar. 2008. Hot corrosion behavior of detonation gun sprayed Cr_3C_2–NiCr coatings on Ni and Fe-based superalloys in Na_2SO_4–60% V_2O_5 environment at 900 °C. *Journal of Alloys and Compounds* 463: 358–372.

Kamal, S., R. Jayaganthan, and S. Prakash. 2009. High temperature oxidation studies of detonation-gun-sprayed Cr_3C_2–NiCr coating on Fe- and Ni-based superalloys in air under cyclic condition at 900 °C. *Journal of Alloys and Compounds* 472: 378–389.

———. 2011. Hot corrosion studies of detonation-gun-sprayed NiCrAlY + 0.4 wt.% CeO_2 coated Superalloys in molten salt environment, Journal of. *Materials Engineering and Performance* 20 (6): 1068–1077.

Kamnis, S., and S. Gu. 2006. Numerical modelling of propane combustion in a high velocity oxygen–fuel thermal spray gun. *Chemical Engineering and Processing* 45: 246–253.

Katanoda, H., H. Yamamoto, and K. Matsuo. 2006. Numerical simulation on supersonic flow in high velocity oxy fuel thermal spray gun. *Journal of Thermal Science* 15 (1): 65–70.

Katanoda, H., T. Matsuoka, S. Kuroda, J. Kawakita, H. Fukanuma, and K. Matsuo. 2005. Aerodynamic study on supersonic flows in high-velocity oxy-fuel thermal spray process. *Journal of Thermal Science* 14: 126–129.

Katanoda, H., H. Yamamoto, and K. Matsuo. 2006. Numerical simulation on supersonic flow in high velocity oxy fuel thermal spray gun. *Journal of Thermal Science* 15 (1): 65–70.

Kaushal, G., H. Singh, and S. Prakash. 2011. Comparative high temperature analysis of HVOF- sprayed and detonation gun sprayed Ni–20Cr coating in laboratory and actual boiler environments. *Oxidation of Metals* 76: 169–191.

Kaushal, G., N. Bala, H. Singh, N. Kaur, and S. Prakash. 2014. Comparative high-temperature corrosion behavior of Ni-20Cr coatings on T22 boiler steel produced by HVOF, D-Gun, and Cold spraying. *Metallurgical and Materials Transactions A* 45A: 395–410.

Kawahara, Y. 2007. Application of high temperature corrosion-resistant materials and coatings under severe corrosive environment in waste-to-energy boilers. *Journal of Thermal Spray Technology* 16 (2): 202–213.

Jin, Kawakita, Seiji Kuroda, Takeshi Fukushima, and Toshiaki Kodama. 2005. Improvement of corrosion resistance of high-velocity oxyfuel-sprayed stainless steel coatings by addition of molybdenum. *Journal of Thermal Spray Technology* 14 (2): 224–230.

Kawakita, J., S. Kuroda, T. Fukushima, H. Katanoda, K. Matsuo, and H. Fukanuma. 2006. Dense titanium coatings by modified HVOF spraying. *Surface & Coatings Technology* 201: 1250–1255.

Ke, P.L., Y.N. Wu, Q.M. Wang, J. Gong, C. Sun, and L.S. Wen. 2005. Study on thermal barrier coatings deposited by detonation gun. *Surface & Coatings Technology* 200: 2271–2276.

Kharlamov, Y.A. 2004. Gaseous pulse detonation spraying: Current status, challenges, and future perspective. In *ITSC-2004: Thermal spray crossing borders*, ed. E. Lugsheider. Düsseldorf, Germany: DVS. E-proceedings.

Killinger, A., M. Kuhn, and R. Gadow. 2006. High-velocity suspension flame spraying (HVSFS), a new approach for spraying nanoparticles with hypersonic speed. *Surface & Coatings Technology* 201 (2006): 1922–1929.

Killinger, A., P. Müller, and R. Gadow. 2015. What do we know, what are the current limitations of suspension HVOF spraying? *Journal of Thermal Spray Technology* 24 (7): 1130–1142.

Kim, J.H., K.M. Lim, B.G. Seong, and C.G. Park. 2001. Amorphous phase formation of Zr-based alloy coating by HVOF spraying process. *Journal of Materials Science* 36: 49–54.

Kim, J.H., M.C. Kim, and C.G. Park. 2003. Evaluation of functionally graded thermal barrier coatings fabricated by detonation gun spray technique. *Surface and Coatings Technology* 168: 275–280.

Kim, K.H., S. Kuroda, and M. Watanabe. 2010. Microstructural development and deposition behavior of titanium powder particles in warm spraying process: From single splat to coating. *Journal of Thermal Spray Technology* 19 (6): 1244–1254.

Kleinstein, G. 1964. Mixing in turbulent axially symmetric free jets. *Journal of Spacecraft* 1 (4): 403–408.

Koji, N., H. Kunio, and Y. Eiichi. 1990. *Glass-coated metallic work piece*. Japanese patent JP2011749, 16-01-1990.

Korpiola, K., J.P. Hirvonen, L. Laas, and F. Rossi. 1997. The influence of the nozzle design on HVOF exit gas velocity and coating microstructure. *Journal of Thermal Spray Technology* 6 (4): 469–474.

Kumar, Ashok, J. Boy, Ray Zatorski, and L.D. Stephenson. 2005. Thermal spray and weld repair alloys for the repair of cavitation damage in turbines and pumps: A technical note. *Journal of Thermal Spray Technology* 14 (2): 177–182.

Kuroda, S., Y. Tashiro, H. Yumoto, S. Taira, H. Fukanuma, and S. Tobe. 2001. Peening action and residual stresses in high-velocity oxygen fuel thermal spraying of 316L stainless steel. *Journal of Thermal Spray Technology* 10 (2): 367–374.

Kuroda, S., M. Watanabe, K.H. Kim, and H. Katanoda. 2011. Current status and future prospects of warm spray technology. *Journal of Thermal Spray Technology* 20 (4): 653–676.

Kwon, J.-Y., J.-H. Lee, Y.-G. Jung, and U. Paik. 2006. Effect of bond coat nature and thickness on mechanical characteristic and contact damage of zirconia-based thermal barrier coatings. *Surface & Coatings Technology* 201: 3483–3490.

Laribi, M., A.B. Vannes, and D. Treheux. 2006. On a determination of wear resistance and adhesion of molybdenum, Cr–Ni and Cr–Mn steel coatings thermally sprayed on a 35CrMo4 steel. *Surface & Coatings Technology* 200: 2704–2710.

Li, M., and P.D. Christofides. 2005. Multi-scale modelling and analysis of an industrial HVOF thermal spray process. *Chemical Engineering Science* 60: 3649–3669.

Li, S., and Panagiotis D. Christofides. 2006. Computational study of particle in-flight behavior in the HVOF thermal spray process. *Chemical Engineering Science* 61: 6540–6552.

Li, C.-J., and A. Ohmori. 1996. The lamellar structure of a detonation gun sprayed $A1_2O_3$ coating. *Surface and Coatings Technology* 82: 254–258.

Chang-Jiu, Li, and Yu-Yue Wang. 2002. Effect of particle state on the adhesive strength of HVOF sprayed metallic coating. *Journal of Thermal Spray Technology* 11 (4): 523–552.

Li, M., P. Shi, and P.D. Christofides. 2004a. Diamond jet hybrid HVOF thermal spray: Gas-phase and particle behavior modelling and feedback control design. *Industrial and Engineering Chemistry Research* 43: 3632–3652.

Li, J.F., L. Li, and F.H. Stott. 2004b. Multi-layered surface coatings of refractory ceramics prepared by combined laser and flame spraying. *Surface and Coatings Technology* 180–181: 500–505.

Lima, C.R.C., and J.M. Guilemany. 1997. The oxidation behavior of HVOF thermal-sprayed MCrAlY coatings. *Surface and Coatings Technology* 93-95: 21–26.

Lima, C.R.C., and J.M. Guilemany. 2007. Adhesion improvements of thermal barrier coatings with HVOF thermally sprayed bond coats. *Surface & Coatings Technology* 201: 4694–4701.

Lima, R.S., and B.R. Marple. 2003a. High Weibull modulus HVOF titania coatings. *Journal of Thermal Spray Technology* 12 (2): 240–249.

———. 2003b. Optimized HVOF titania coatings. *Journal of Thermal Spray Technology* 12 (3): 360–369.

Lima, C.R.C., J. Nin, and J.M. Guilemany. 2006. Evaluation of residual stresses of thermal barrier coatings with HVOF thermally sprayed bond coats using the modified layer removal method (MLRM). *Surface & Coatings Technology* 200: 5963–5972.

Lin, L., and K. Han. 1998. Optimization of surface properties by flame spray coating and boriding. *Surface and Coatings Technology* 106: 100–105.

Lin, Q.S., K.S. Zhou, C.M. Deng, M. Liu, L.P. Xu, and C.G. Deng. 2014. Deposition mechanisms and oxidation behaviors of Ti-Ni coatings deposited in low-temperature HVOF spraying process. *Journal of Thermal Spray Technology* 23 (6): 892–902.

Liu, Hui, and Jihua Huang. 2005. Reactive thermal spraying of TiC-Fe composite coating by using asphalt as carbonaceous precursor. *Journal of Materials Science* 40: 4149–4151.

Liu, Hui Yuan, and Ji Hua Huang. 2006. Reactive flame spraying of TiC-Fe cermet coating using asphalt as a carbonaceous precursor. *Surface & Coatings Technology* 200: 5328–5333.

Liu, C.S., J.H. Huang, and S. Yin. 2002. The influence of composition and process parameters on the microstructure of TiC-Fe coatings obtained by reactive flame spray process. *Journal of Materials Science* 37 (2002): 5241–5245.

Liu, M., K. Yang, C.-M. Deng, C.-G. Deng, and K.-S. Zhou. 2016. Microstructure and properties of Cu coating fabricated onto diamond-Cu substrate by low-temperature HVOF process. *Journal of Thermal Spray Technology* 25 (8): 1516–1525.

Lopez, A.R., B. Hassan, W.L. Oberkampf, R.A. Neiser, and T.J. Roemer. 1998. Computational fluid dynamics analysis of a wire-feed, high-velocity oxygen fuel (HVOF) thermal spray torch. *Journal of Thermal Spray Technology* 7 (3): 374–382.

Lugsheider, E., P. Remer, A. Nyland, and R. Siking. 1995. Thermal spraying of Bio-active glass ceramics. In *Thermal Spray: Science and Technology*, ed. C.C. Berndt and S. Sampath, 583–587. Materials Park, OH, USA: ASM International.

Lyphout, C., and S. Björklund. 2015. Internal diameter HVAF spraying for Wear and corrosion applications. *Journal of Thermal Spray Technology* 24 (1–2): 235–243.

Lyphout, C., K. Sato, S. Houdkova, E. Smazalova, L. Lusvarghi, G. Bolelli, and P. Sassatelli. 2016. Tribological properties of hard metal coatings sprayed by high-velocity air fuel process. *Journal of Thermal Spray Technology* 25 (1–2): 331–345.

Ma, J., X. Liu, W.O. Qu, and C. Zhou. 2015. Corrosion behavior of detonation gun sprayed Al coating on sintered NFeB. *Journal of Thermal Spray Technology* 24 (3): 394–400.

Maiti, A.K., N. Mukhopadhyay, and R. Raman. 2007. Effect of adding WC powder to the feedstock of WC-Co-Cr based HVOF coating and its impact on erosion and abrasion resistance. *Surface & Coatings Technology* 201: 7781–7788.

Manish, R. 2002. Dynamic hardness detonation sprayed WC-co coatings. *Journal of Thermal Spray Technology* 11 (3): 393–399.

Marple, B.R., and R.S. Lima. 2005. Process temperature/velocity-hardness-Wear relationships for high-velocity Oxyfuel sprayed nanostructured and conventional cermet coatings. *Journal of Thermal Spray Technology* 14 (1): 67–76.

Marple, B.R., and J. Voyer. 2001. Improved Wear performance by the incorporation of solid lubricants during thermal spraying. *Journal of Thermal Spray Technology* 10 (4): 626–636.

Masataka, M., and K. Kazumi. 1989. *Substrate for flame-sprayed tile*. Japanese patent JP1192777, 02-08-1989.

Matikainen, V., H. Koivuluoto, P. Vuoristo, J. Schubert, and S. Houdkova. 2018. Effect of nozzle geometry on the microstructure and properties of HVAF-sprayed WC-10Co4Cr and Cr3C2-25NiCr Coatings. *Journal of Thermal Spray Technology* 27: 680–694.

Matthews, S., M. Hyland, and B. James. 2004. Long-term carbide development in high-velocity oxygen fuel/high-velocity air fuel Cr_3C_2-NiCr coatings heat treated at 900 °C. *Journal of Thermal Spray Technology* 13 (4): 526–536.

Mesrati, N., H. Ajhrourh, Du Nguyen, and D. Treheux. 2000. Thermal spraying and adhesion of oxides onto graphite. *Journal of Thermal Spray Technology* 9 (1): 95–99.

Milanti, A., H. Koivuluoto, and P. Vuoristo. 2015. Influence of the spray gun type on microstructure and properties of HVAF sprayed Fe-based corrosion resistant coatings. *Journal of Thermal Spray Technology* 24 (7): 1312–1322.

Min'kov, D.V., V.Yu. Lakunin, S.T. Kartashov, O.M. Bashkirov, A.S. Ivanov, A.V. Kasatkin, and M.D. Min'kov. 2008. Restoration of drying cylinders on spinning machines by gas detonation spraying. *Fibre Chemistry* 40 (6): 545–547.

Mingheng, Li, and Panagiotis D. Christofides. 2006. Computational study of particle in-flight behavior in the HVOF thermal spray process. *Chemical Engineering Science* 61: 6540–6552.

Mizuno, H., and J. Kitamura. 2007. MoB/CoCr cermet coatings by HVOF spraying against Erosion by molten Al-Zn alloy. *Journal of Thermal Spray Technology* 16 (3): 404–413.

Modi, S.C., and E. Calla. 2001. A study of high-velocity combustion wire molybdenum coatings. *Journal of Thermal Spray Technology* 10 (3): 480–486.

Moskowitz, L., and K. Trelewicz. 1997. HVOF coatings for heavy-Wear, high-impact applications. *Journal of Thermal Spray Technology* 6 (3): 294–299.

Mudgal, D., S. Singh, and S. Prakash. 2015. Evaluation of ceria-added Cr_3C_2-25(NiCr) coating on three Superalloys under simulated incinerator environment. *Journal of Thermal Spray Technology* 24 (3): 496–514.

Müller, P., A. Killinger, and R. Gadow. 2012. Comparison between high-velocity suspension flame spraying and suspension plasma spraying of alumina. *Journal of Thermal Spray Technology* 21 (6): 1120–1127.

Murthy, J.K.N., and B. Venkataraman. 2006. Abrasive wear behaviour of WC–CoCr and Cr_3C_2–20(NiCr) deposited by HVOF and detonation spray processes. *Surface & Coatings Technology* 200: 2642–2652.

Murthy, J.K.N., D.S. Rao, and B. Venkataraman. 2001. Effect of grinding on the erosion behaviour of a WC–Co–Cr coating deposited by HVOF and detonation gun spray processes. *Wear* 249: 592–600.

Murthy, J.K.N., S. Bysakh, K. Gopinath, and B. Venkataraman. 2007. Microstructure dependent erosion in Cr_3C_2–20(NiCr) coating deposited by a detonation gun. *Surface & Coatings Technology* 202: 1–12.

Navas, C., R. Colaço, J. de Damborenea, and R. Vilar. 2006. Abrasive wear behaviour of laser clad and flame sprayed-melted NiCrBSi coatings. *Surface & Coatings Technology* 200: 6854–6862.

Navidpour, A.H., M. Salehi, H.R. Salimijazi Y. Kalantari, and M. Azarpour Siahkali. 2017. Photocatalytic activity of flame-sprayed coating of zinc ferrite powder. *Journal of Thermal Spray Technology* 26: 2030–2039.

Neiser, R.A., J.E. Brockmann, T.J. O'Hern, R.C. Dyhkuizen, M.F. Smith, T.J. Roemer, and R.E. Teets. 1995. Wire melting and droplet atomization in a HVOF jet. In *Thermal Spray Science and Technology*, ed. C.C. Berndt and S. Sampath, 99–104. Materials Park OH, USA: ASM International.

Neiser, R.A., M.F. Smith, and R.C. Dykhuizen. 1998. Oxidation in wire HVOF-sprayed steel. *Journal of Thermal Spray Technology* 7 (4): 537–545.

Nevgod, V.A., V.H. Kadyrov, and A. Khairutdinov. 1987a. *Gas detonation apparatus*. U.S. Patent 4 669 658.

———. 1987b. *Gas detonation apparatus*. U.S. Patent 4 687 135.

Ni, L.Y., C. Liu, H. Huang, and C.G. Zhou. 2011. Thermal Cycling behavior of thermal barrier coatings with HVOF NiCrAlY bond coat. *Journal of Thermal Spray Technology* 20 (5): 1133–1138.

Niemi, K., P. Vuoristo, and T. Mantyla. 1994. Properties of alumina-based coatings deposited by plasma spray and detonation gun spray processes. *Journal of Thermal Spray Technology* 3 (2): 199–203.

Nikolaev, Y.A., A.A. Vasil'ev, and B.Yu. Ul'yanitskii. 2003. Gas detonation and its application in engineering and technologies (review). *Combustion, Explosion, and Shock Waves* 39 (4): 382–410.

Nylén, P., and R. Bandyopadhyay. 2000. A computational fluid dynamic analysis of gas and particle flow in flame spraying. In *Thermal Spray: Surface Engineering via Applied Research*, ed. C.C. Berndt, 237–244. Materials Park, Ohio, USA: ASM International®.

Oberkampf, W.L., and M. Talpallikar. 1994. Analysis of a high velocity oxygen-fuel (HVOF). In *Proceedings of 7th. National Thermal Spray Conf., Boston, MA*, 381–392.

———. 1996a. Analysis of a high velocity oxygen-fuel (HVOF) thermal spray torch part1: Numerical simulation. *Journal of Thermal Spray Technology* 5 (1): 53–61.

———. 1996b. Analysis of a high velocity oxygen-fuel (HVOF) thermal spray torch part 2: Computational results. *Journal of Thermal Spray Technology* 5 (1): 62–68.

Oliker, V.E., E.F. Grechishkin, V.V. Polotai, M.G. Loskutov, and I.I. Timofeeva. 2004. Influence of the structure and properties of WC-Co alloy powders on the structure and wear resistance of detonation coatings. *Powder Metallurgy and Metal Ceramics* 43 (5–6): 258–264.

Oliker, V.E., V.L. Sirovatka, I.I. Timofeeva, E.F. Grechishkin, and T. Ya Gridasova. 2005. Effects of properties of titanium aluminide powders and detonation spraying conditions on phase and structure formation in coatings. *Powder Metallurgy and Metal Ceramics* 44 (9–10): 472–480.

Oliker, V.E., V.L. Sirovatka, I.I. Timofeeva, T. Ya Gridasova, and Ye F. Hrechyshkin. 2006. Formation of detonation coatings based on titanium aluminide alloys and aluminium titanate ceramic sprayed from mechanically alloyed powders Ti—Al. *Surface & Coatings Technology* 200: 3573–3581.

Oliker, V.E., M.Yu. Barabash, E.F. Grechishkin, I.I. Timofeeva, and T. Ya Gridasova. 2007a. High-temperature air oxidation based on eutectic (β-NiAl + γ- and NiAl) Intermetallide. *Powder Metallurgy and Metal Ceramics* 46 (3–4): 175–181.

Oliker, V.E., A.A. Pritulyak, V.L. Syrovatka, E.F. Grechishkin, and T. Ya Gridasova. 2007b. Formation and high-temperature oxidation of thermal-barrier coatings with Ti–Al–Cr binding layer. *Powder Metallurgy and Metal Ceramics* 46 (9–10): 483–491.

Otsubo, F., H. Era, T. Uchida, and K. Kishitake. 2000. Properties of Cr_3C_2-NiCr cermet coating sprayed by high power plasma and high velocity oxy-fuel processes. *Journal of Thermal Spray Technology* 9 (4): 499–504.

Ozdemir, I., I. Hamanaka, Y. Tsunekawa, and M. Okumiya. 2005. In-process exothermic reaction in high-velocity oxyfuel and plasma spraying with SiO_2/Ni/Al-Si-mg composite powder. *Journal of Thermal Spray Technology* 14 (3): 321–329.

Panossian, Z., L. Mariaca, M. Morcillo, S. Flores, J. Rocha, J.J. Pen, F. Herrera, F. Corvo, M. Sanchez, O.T. Rincon, G. Pridybailo, and J. Simancas. 2005. Steel cathodic protection afforded by zinc, aluminium and zinc/aluminium alloy coatings in the atmosphere. *Surface & Coatings Technology* 190: 244–248.

Pant, Bharat K., Vivek Arya, and B.S. Mann. 2007. Development of low-oxide MCrAlY coatings for gas turbine applications. *Journal of Thermal Spray Technology* 16 (2): 275–280.

Parco, M., L. Zhao, J. Zwick, K. Bobzin, and E. Lugscheider. 2006. Investigation of HVOF spraying on magnesium alloys. *Surface & Coatings Technology* 201: 3269–3274.

Paredes, R.S.C., S.C. Amico, and A.S.C.M. d'Oliveira. 2006. The effect of roughness and pre-heating of the substrate on the morphology of aluminium coatings deposited by thermal spraying. *Surface & Coatings Technology* 200: 3049–3055.

Park, S.Y., M.C. Kim, and C.G. Park. 2007. Mechanical properties and microstructure evolution of the nano WC–Co coatings fabricated by detonation gun spraying with post heat treatment. *Materials Science and Engineering A* 449–451: 894–897.

Perry, J.M., A. Neville, and T. Hodgkiess. 2002. A comparison of the corrosion behaviour of WC-Co-Cr and WC-Co HVOF thermally sprayed coatings by in situ atomic force microscopy (AFM). *Journal of Thermal Spray Technology* 11 (4): 536–541.

Petrovicova, E., R. Knight, L.S. Schadler, and T.E. Twardowski. 2000. Nylon 11/Silica nanocomposite coatings applied by the HVOF process. II. mechanical and barrier properties. *Journal of Applied Polymer Science* 78: 2272–2289.

Planche, M.P., H. Liao, B. Normand, and C. Coddet. 2005. Relationships between NiCrBSi particle characteristics and corresponding coating properties using different thermal spraying processes. *Surface & Coatings Technology* 200: 2465–2473.

Podchernyaeva, I.A., V.V. Shchepetov, A.D. Panasyuk, V.Yu. Gromenko, D.V. Yurechko, and V.P. Katashinskii. 2003. Refractory and ceramic materials structure and properties of wear-resistant detonation coatings based on titanium carbonitride. *Powder Metallurgy and Metal Ceramics* 42 (9–10): 497–502.

Pogrebnyak, A.D., Yu.N. Tyurin, Yu.F. Ivanov, A.P. Kobzev, O.P. Kul'ment'eva, and M.I. Il'yashenko. 2000. Preparation and investigation of the structure and properties of Al_2O_3 plasma-detonation coatings. *Technical Physics Letters* 26 (11): 960–963.

Poirier, T., A. Vardelle, M.F. Elchinger, M. Vardelle, A. Grimaud, and H. Vesteghem. 2003. Deposition of nanoparticle suspensions by aerosol flame spraying: Model of the spray and impact processes. *Journal of Thermal Spray Technology* 12 (3): 393–402.

Poorman, R.M., H.B. Sargent, and R. Lamprey. 1955. *Method and apparatus utilizing detonation waves for spraying and other purposes*'. US patent 2 714 563.

Rajasekaran, B.S., S. Ganesh Sundara Raman, V. Joshi, and G. Sundararajan. 2006. Effect of detonation gun sprayed Cu–Ni–In coating on plain fatigue and fretting fatigue behavior of Al–Mg–Si alloy. *Surface & Coatings Technology* 201: 1548–1558.

Rajasekaran, B.S., S. Ganesh Sundara Ramana, V. Joshi, and G. Sundararajan. 2008. Performance of plasma sprayed and detonation gun sprayed Cu–Ni–In coatings on Ti–6Al–4V under plain fatigue and fretting fatigue loading. *Materials Science and Engineering A* 479: 83–92.

Rajasekaran, B., G. Mauer, and R. Vaßen. 2011. Enhanced characteristics of HVOF-sprayed MCrAlY bond coats for TBC applications. *Journal of Thermal Spray Technology* 20 (6): 1209–1216.

Ramadan, K., and P. Barry Butler. 2004. Analysis of particle dynamics and heat transfer in detonation thermal spraying systems. *Journal of Thermal Spray Technology* 13 (2): 248–264.

Rani, A., N. Bala, and C.M. Gupta. 2017. Accelerated hot corrosion studies of D-gun-sprayed Cr_2O_3–50% Al_2O_3 coating on boiler steel and Fe- based Superalloy. *Oxidation of Metals* 88: 621–648.

Richer, P., M. Yandouzi, L. Beauvais, and B. Jodoin. 2010. Oxidation behaviour of CoNiCrAlY bond coats produced by plasma. *HVOF and cold gas dynamic spraying, Surface & Coatings Technology* 204: 3962–3974.

Roberson, J.A., and C.T. Crowe. 1997. *Engineering fluid dynamics*. 6th ed. New York: Wiley.

Rodriguez, R.M.H.P., R.S.C. Paredes, S.H. Wido, and A. Calixto. 2007. Comparison of aluminium coatings deposited by flame spray and by electric arc spray. *Surface & Coatings Technology* 202: 172–179.

Roy, G.D., S.M. Frolov, A.A. Borisov, and D.W. Netzer. 2004. Pulse detonation propulsion: Challenges, current status, and future perspective. *Progress in Energy and Combustion Science* 30: 545–672.

Sadeghimeresht, E., N. Markocsan, and P. Nylen. 2016. A comparative study on Ni-based coatings prepared by HVAF, HVOF, and APS methods for corrosion protection applications. *Journal of Thermal Spray Technology* 25 (8): 1604–1616.

Saeidi, S., K.T. Voisey, and D.G. McCartney. 2011. Mechanical properties and microstructure of VPS and HVOF CoNiCrAlY coatings. *Journal of Thermal Spray Technology* 20 (6): 1231–1243.

Sainz, M.A., M.I. Osendi, and P. Miranzo. 2008. Protective Si-Al-O-Y glass coatings on stainless steel in situ prepared by combustion flame spraying. *Surface & Coatings Technology* 202: 1712–1717.

Sakaki, K., and Y. Shimizu. 2001. Effect of the increase in the entrance convergent section length of the gun nozzle on the high-velocity oxygen fuel and cold spray process. *Journal of Thermal Spray Technology* 10 (3): 487.

Sakata, K., K. Nakano, H. Miyahara, Y. Matsubara, and K. Ogi. 2007. Microstructure control of thermally sprayed co-based self-fluxing alloy coatings by diffusion treatment. *Journal of Thermal Spray Technology* 16 (5–6): 991–997.

Saladi, S., J.V. Menghani, and S. Prakash. 2015. Characterization and evaluation of cyclic hot corrosion resistance of detonation-gun sprayed Ni-5Al coatings on Inconel-718. *Journal of Thermal Spray Technology* 24 (5): 778–788.

Saravanan, P., V. Selvarajan, D.S. Rao, S.V. Joshi, and G. Sundararajan. 2000. Influence of process variables on the quality of detonation gun sprayed alumina coatings. *Surface and Coatings Technology* 123: 44–54.

Schwetzke, R., and H. Kreye. 1999. Microstructure and properties of tungsten carbide coatings sprayed with various high-velocity oxygen fuel spray systems. *Journal of Thermal Spray Technology* 8 (3): 433–439.

Scrivani, A., U. Bardi, L. Carrafiello, A. Lavacchi, F. Niccolai, et al. 2003. A comparative study of high velocity oxygen fuel, vacuum plasma spray, and axial plasma spray for the deposition of CoNiCrAlY bond coat alloy. *Journal of Thermal Spray Technology* 12 (4): 504–507.

Semenov, S.Y., and B.M. Cetegen. 2002. Experiments and modeling of the deposition of nano-structured alumina–titania coatings by detonation waves. *Materials Science and Engineering* A335: 67–81.

Senderowski, C., and Z. Bojar. 2008. Gas detonation spray forming of Fe–Al coatings in the presence of interlayer. *Surface & Coatings Technology* 202: 3538–3548.

———. 2009. Influence of detonation gun spraying conditions on the quality of Fe-Al intermetallic protective coatings in the presence of NiAl and NiCr interlayers. *Journal of Thermal Spray Technology* 18 (3): 435–447.

Sidhu, T.S., S. Prakash, and R.D. Agrawal. 2005. Studies on the properties of high-velocity oxy-fuel thermal spray coatings for higher temperature applications. *Materials Science* 41 (6): 805–823.

Sidhu, H.S., B.S. Sidhu, and S. Prakash. 2006. Comparative characteristic and erosion behavior of NiCr coatings deposited by various high-velocity Oxyfuel spray processes Journal of. *Materials Engineering and Performance* 15 (6): 699–704.

Sidhu, T.S., S. Prakash, and R.D. Agrawal. 2006a. Characterisation of NiCr wire coatings on Ni- and Fe-based superalloys by the HVOF process. *Surface & Coatings Technology* 200: 5542–5549.

———. 2006b. Characterizations and hot corrosion resistance of Cr_3C_2-NiCr coating on Ni-base superalloys in an aggressive environment. *Journal of Thermal Spray Technology* 15 (4): 811–816.

———. 2006c. Hot corrosion resistance of high-velocity oxyfuel sprayed coatings on a nickel-base superalloy in molten salt environment. *Journal of Thermal Spray Technology* 15 (3): 387–399.

Sidhu, H.S., B.S. Sidhu, and S. Prakash. 2007a. Hot corrosion behavior of HVOF sprayed coatings on ASTM SA213-T11 steel. *Journal of Thermal Spray Technology* 16 (3): 349–354.

Sidhu, T.S., A. Malik, S. Prakash, and R.D. Agrawal. 2007b. Oxidation and hot corrosion resistance of HVOF WC-NiCrFeSiB coating on Ni- and Fe-based superalloys. *Journal of Thermal Spray Technology* 16 (5-6): 844–849.

Smith, R.W. 1991. Plasma spray processing... The state of the art and future. From a surface to a materials processing technology. In *Proceedings of the 2nd Plasma Technik symposium*, vol. 1, 13–38. Wohlen, Switzerland: Plasma Technik.

Sobiecki, J.R., J. Ewertowshi, T. Babul, and T. Wierzchon. 2004. Properties of alumina coatings produced by gas-detonation method. *Surface and Coatings Technology* 180–181: 556–555.

Srivatsan, V.R., and A. Dolatabadi. 2006. Simulation of particle-shock interaction in a high velocity oxygen fuel process. *Journal of Thermal Spray Technology* 15 (4): 481–487.

Stahr, C.C., S. Saaro, L.-M. Berger, J. Dubsky, K. Neufuss, and M. Hermann. 2006. Dependence of the stabilization of α-alumina on the spray process. *Journal of Thermal Spray Technology* 16 (5–6): 822–830.

Stanisic, J., D. Kosikowski, and P.S. Mohanty. 2006. High-speed visualization and plume characterization of the hybrid spray process. *Journal of Thermal Spray Technology* 15 (4): 750–758.

Stiegler, N., D. Bellucci, G. Bolelli, V. Cannillo, R. Gadow, A. Killinger, L. Lusvarghi, and A. Sola. 2012. High-velocity suspension flame sprayed (HVSFS) hydroxyapatite coatings for biomedical applications. *Journal of Thermal Spray Technology* 21 (2): 275–287.

Sundararajan, T., S. Kuroda, and F. Abe. 2004a. Steam oxidation of 80Ni-20Cr high-velocity oxyfuel coatings on 9Cr-1Mo steel: Diffusion-induced phase transformations in the substrate adjacent to the coating. *Metallurgical and Materials Transactions A* 36A: 2165–2174.

———. 2004b. Effect of thermal spray on the microstructure and adhesive strength of high-velocity oxy-fuel–sprayed Ni-Cr coatings on 9Cr-1Mo steel. *Metallurgical and Materials Transactions A* 35A: 3187–3199.

Sundararajan, G., D. Sen, and G. Sivakumar. 2005. The tribological behavior of detonation sprayed coatings: The importance of coating process parameters. *Wear* 258: 377–391.

Sundararajan, G., G. Sivakumar, D. Sen, D. Srinivasa Rao, and G. Ravichandra. 2010. The tribological behaviour of detonation sprayed TiMo(CN) based cermet coatings. *International Journal of Refractory Metals & Hard Materials* 28: 71–81.

Suresh, Babu P., D.S. Rao, G.V.N. Rao, and G. Sundararajan. 2007. Effect of feedstock size and its distribution on the properties of detonation sprayed coatings. *Journal of Thermal Spray Technology* 16 (2): 281–290.

Suresh, Babu P., B. Basu, and G. Sundararajan. 2008. Processing–structure–property correlation and decarburization phenomenon in detonation sprayed WC–12Co coatings. *Acta Materialia* 56: 5012–5026.

Tatsuya, N., K. Izozou, M. Haruyuki, and S. Yasuhi. 1988. *Improved glaze application for coating and flame spraying and glaze*. Japanese patent JP63277583, 15-11-1988.

Tawfik, H.H., and F. Zimmerman. 1997. Mathematical modelling of the gas and powder flow in HVOF systems. *Journal of Thermal Spray Technology* 6 (3): 345–352.

Taylor, T.A., and J.K. Knapp. 1995. Dispersion-strengthened modified MCrAlY coatings produced by reactive deposition. *Surface and Coatings Technology* 76-77: 34–40.

Thermal Spraying, Practice, Theory and Application. 1985. *American welding society*. Miami.

Thiele, S., R.B. Heimann, L.-M. Berger, M. Herrmann, M. Nebelung, T. Schnick, B. Wielage, and P. Vuoristo. 2002. Microstructure and

properties of thermally sprayed silicon nitride-based coatings. *Journal of Thermal Spray Technology* 11 (2): 218–225.

Thorpe, M.L., and H.J. Richter. 1992. A pragmatic analysis and comparison of HVOF processes. *Journal of Thermal Spray Technology* 1 (2): 161–170.

Tikkanen, J., K.A. Gross, C.C. Berndt, V. Pitkatnen, J. Keskinen, S. Raghu, M. Rajala, and J. Karthikeyan. 1997. Characteristics of the liquid flame spray process. *Surface and Coatings Technology* 90: 210–216.

Tillmann, W., E. Vogli, and J. Nebel. 2007. Development of detonation flame sprayed Cu-Base coatings containing large ceramic particles. *Journal of Thermal Spray Technology* 16 (5–6): 751–758.

Tillmann, W., C. Schaak, L. Hagen, G. Mauer, and G. Matthäus. 2018. Internal diameter coating processes for bond coat (HVOF) and thermal barrier coating (APS) systems. *Journal of Thermal Spray Technology*. Published online: 30-10-2018.

Torres, B., P. Rodrigo, M. Campo, A. Urena, and J. Rams. 2009. Oxy-acetylene flame thermal spray of Al/SiCp composites with high fraction of re-enforcements. *Journal of Thermal Spray Technology* 18 (4): 642–651.

Totemeier, T.C. 2005. Effect of high-velocity oxygen-fuel thermal spraying on the physical and mechanical properties of type 316 stainless steel. *Journal of Thermal Spray Technology* 14 (3): 369–372.

Totemeier, T.C., R.N. Wright, and W.D. Swank. 2002. Microstructure and stresses in HVOF sprayed Iron aluminide coatings. *Journal of Thermal Spray Technology* 11 (3): 400–408.

———. 2003. Mechanical and physical properties of high-velocity oxy-fuel–sprayed Iron aluminide coatings. *Metallurgical and Materials Transactions A* 34A: 2223–2231.

———. 2004. Residual stresses in high-velocity oxy-fuel metallic coatings. *Metallurgical and Materials Transactions A* 35A: 1807–1814.

Trompetter, W.J., M. Hyland, P. Munroe, and A. Markwitz. 2005. Evidence of mechanical interlocking of NiCr particles thermally sprayed onto Al substrates. *Journal of Thermal Spray Technology* 14 (4): 524–529.

Trompetter, W., M. Hyland, D. McGrouther, P. Munroe, and A. Markwitz. 2006. Effect of substrate hardness on splat morphology in high-velocity thermal spray coatings. *Journal of Thermal Spray Technology* 15 (4): 663–669.

———. 2010. The effect of substrate surface oxides on the bonding of NiCr alloy particles HVAF thermally sprayed onto aluminum substrates. *Journal of Thermal Spray Technology* 19 (5): 1024–1031.

Venkataraman, R., B. Ravikumar, R. Krishnamurthy, and D.K. Das. 2006. A study on phase stability observed in as sprayed Alumina-13 wt.% Titania coatings grown by detonation gun and plasma spraying on low alloy steel substrates. *Surface & Coatings Technology* 201: 3087–3095.

Vijaya, Babu M., R. Krishna Kumar, O. Prabhakar, and N. Gowri Shank. 1996a. Simultaneous optimization of flame spraying process parameters for high quality molybdenum coatings using Taguchi methods. *Surface & Coatings Technology* 79: 276–288.

Vijaya, Babu M., R. Krishna Kumar, O. Prabhakar, and N. Gowri Shankar. 1996b. Simultaneous optimization of flame spraying process parameters for high quality molybdenum coatings using Taguchi methods. *Surface and Coatings Technology* 79: 276–288.

Villiers Lovelock, H.L., P.W. Richter, J.M. Benson, and P.M. Young. 1998. Parameter study of HP/HVOF deposited WC-Co coatings. *Journal of Thermal Spray Technology* 7 (1): 97–107.

Voyer, Joel. 2013. Flexible and conducting metal-fabric composites using the flame spray process for the production of Li-ion batteries. *Journal of Thermal Spray Technology* 22 (5): 699–709.

Wang, Y. 2004. Nano- and submicron-structured sulfide self-lubricating coatings produced by thermal spraying. *Tribology Letters* 17 (2): 165–168.

Wang, J., Zhang Li, B. Sun, and Y. Zhou. 2000. Study of the Cr_3C_2-NiCr detonation spray coating. *Surface and Coatings Technology* 130: 69–73.

Wang, Jun, Baode Sun, Qixin Guo, Mitsuhiro Nishio, and Hiroshi Ogawa. 2002. Wear resistance of a Cr_3C_2-NiCr detonation spray coating. *Journal of Thermal Spray Technology* 11 (2): 261–265.

Wang, J., Baode Sun, Qixin Guo, Mitsuhiro Nishio, and Hiroshi Ogawa. 2002b. Wear resistance of a Cr_3C_2-NiCr detonation spray coating. *Journal of Thermal Spray Technology* 11 (2): 261–265.

Wang, T.-G., S.-S. Zhao, W.-G. Hua, J. Gong, and C. Sun. 2009. Design of a separation device used in detonation gun spraying system and its effects on the performance of WC–Co coatings. *Surface & Coatings Technology* 203: 1637–1644.

Wang, T.-G., S.-S. Zhao, W.-G. Hua, J.-B. Li, J. Gong, and C. Sun. 2010. Estimation of residual stress and its effects on the mechanical properties of detonation gun sprayed WC–Co coatings. *Materials Science and Engineering A* 527 (3): 454–461.

Wang, X., Q. Song, and Z. Yu. 2016. Numerical investigation of combustion and flow dynamics in a high velocity oxygen-fuel thermal spray gun. *Journal of Thermal Spray Technology* 25 (3): 441–450.

Wielage, B., A. Wank, H. Pokhmurska, T. Grund, Ch. Rupprecht, G. Reisel, and E. Friesen. 2006. Development and trends in HVOF spraying technology. *Surface & Coatings Technology* 201: 2032–2037.

Wigren, J., et al. 1996. On-line diagnostics of traditional flame spraying as a tool to increase reproducibility. In *Proceedings of National Thermal Spray Conference*, ed. C.C. Berndt, 675–681. Materials Park, OH, USA: ASM International.

Withy, B.P., M.M. Hyland, and B.J. James. 2008. The effect of surface chemistry and morphology on the properties of HVAF PEEK single splats. *Journal of Thermal Spray Technology* 17 (5–6): 631–636.

Wood, R.J.K., B.G. Mellor, and M.L. Binfield. 1997. Sand erosion performance of detonation gun applied tungsten carbide/cobalt-chromium coatings. *Wear* 211: 70–83.

Wu, Y.N., F.H. Wang, W.G. Hua, J. Gong, C. Sun, and L.S. Wen. 2003. Oxidation behavior of thermal barrier coatings obtained by detonation spraying. *Surface and Coatings Technology* 166: 189–194.

Wu, Y.N., P.L. Ke, Q.M. Wang, C. Sun, and F.H. Wang. 2004. High temperature properties of thermal barrier coatings obtained by detonation spraying. *Corrosion Science* 46: 2925–2935.

Wu, T., S. Kuroda, J. Kawakita, K. Katanoga, and R. Reed. 2006. Processing and properties of titanium coatings produced by warm spraying. In *Thermal spray: Building on 100 years of success*, ed. B. Marple et al. ASM International, Materials Park, OH, USA. e-proceedings.

Yang, G., H. Zu-kun, X. Xiaolei, and X. Gang. 2001. Formation of molybdenum boride cermet coating by the detonation spray process. *Journal of Thermal Spray Technology* 10 (3): 456–460.

Yang, Y.-M., H. Liao, and C. Coddet. 2002. Simulation and application of a HVOF process for MCrAlY thermal spraying. *Journal of Thermal Spray Technology* 11 (1): 36–43.

Yang, G.-J., C.-J. Li, and Y.-Y. Wang. 2005. Phase formation of Nano-TiO_2 particles during flame spraying with liquid feedstock. *Journal of Thermal Spray Technology* 14 (4): 480–486.

Yasunari, Ishikawa, Seiji Kuroda, and Jin Kawakita. 2007. Yukihiro Sakamoto, Matsufumi Takaya, sliding wear properties of HVOF sprayed WC-20%Cr_3C_2-7%Ni cermet coatings. *Surface & Coatings Technology* 201: 4718–4727.

Yilbas, B.S., and A.F.M. Arif. 2007. Residual stress analysis for HVOF diamalloy 1005 coating on Ti–6Al–4V alloy. *Surface & Coatings Technology* 202: 559–568.

Yilbas, B.S., M. Khalid, and B.J. Abdul-Aleem. 2003. Corrosion behavior of HVOF coated sheets. *Journal of Thermal Spray Technology* 12 (4): 572–575.

Yuan, X., H. Wang, G. Hou, and B. Zha. 2006. Numerical modelling of a low temperature high velocity air fuel spraying process with injection of liquid and metal particles. *Journal of Thermal Spray Technology* 15 (3): 413–421.

Yuan, F.H., Z.X. Chen, Z.W. Huang, Z.G. Wang, and S.J. Zhu. 2008. Oxidation behavior of thermal barrier coatings with HVOF and detonation-sprayed NiCrAlY bondcoats. *Corrosion Science* 50: 1608–1617.

Yuuzou, Kawahara. 2007. Application of high temperature corrosion-resistant materials and coatings under severe corrosive environment in waste-to-energy boilers. *Journal of Thermal Spray Technology* 16 (2): 202–213.

Zhang, T., Z. Qiu, Y. Bao, G.T. Gawne, and K. Zhang. 2000. Temperature profile and thermal stress analysis of plasma sprayed glass-composite coatings. In *Thermal spray: Surface engineering via applied research*, ed. C.C. Berndt, 355–361. ASM International, Materials Park, OH, USA.

Zhang, Yu-Juan, Xiao-Feng Sun, Heng-Rong Guana, and Zhuang-Qi Hua. 2002. 1050°C isothermal oxidation behavior of detonation gun sprayed NiCrAlY coating. *Surface and Coatings Technology* 161: 302–305.

Zhang, Y.J., X.F. Sun, Y.C. Zhang, T. Jin, C.G. Deng, H.R. Guan, and Z.Q. Hu. 2003. A comparative study of DS NiCrAlY coating and LPPS NiCrAlY coating. *Materials Science and Engineering A* 360: 65–69.

Zhang, G., H. Liao, H. Yu, S. Costil, S.G. Mhaisalkar, J.-M. Bordes, and C. Coddet. 2006. Deposition of PEEK coatings using a combined flame spraying–laser remelting process. *Surface & Coatings Technology* 201: 243–249.

Zhang, Z., B. Liang, and H. Guo. 2014. Interface microstructure and Tribological properties of flame spraying NiCr/La_2O_3 coatings. *Journal of Thermal Spray Technology* 23 (8): 1404–1412.

Zhu, J.L., J.H. Huang, H.T. Wang, J.L. Xu, X.K. Zhao, and H. Zhang. 2008. In-situ synthesis and microstructure of TiC–Fe36Ni composite coatings by reactive detonation-gun spraying. *Materials Letters* 62: 2009–2012.